

**FULL-WAVE ANALYSIS OF IMPERFECT PLANAR RADIATORS
ON LOSSY SUBSTRATES OF FINITE EXTENT**

by

Martin Gimersky

Engineer, 1988 (Czech Technical University of Prague, Czechoslovakia)

A Dissertation Submitted in Partial Fulfillment
of the Requirements for the Degree of

DOCTOR OF PHILOSOPHY

in the Department of Electrical and Computer Engineering

We accept this dissertation as conforming
to the required standard

Dr. J. Bornermann, Supervisor (Dept. of Elec. & Comp. Engineering)

Dr. R. Vahldieck, Departmental Member (Dept. of Elec. & Comp. Engineering)

Dr. R.L. Kirlin, Departmental Member (Dept. of Elec. & Comp. Engineering)

Dr. S. Dost, Outside Member (Dept. of Mechanical Engineering)

Dr. L. Shafai, External Examiner (Dept. of Elec. & Comp. Engg., University of Manitoba)

© Martin GIMERSKY, 1996
UNIVERSITY OF VICTORIA

All rights reserved. This dissertation may not be reproduced in whole or in part, by photocopy or other means, without the permission of the author.

Supervisor: Prof. Jens Bornemann

ABSTRACT

Planar radiators have several interesting practical features — including low profile, light weight, conformability, potentially low development/production costs and the ease with which they can be integrated with printed feed networks and active circuits — expected from modern antennas. As a result, planar antennas are a serious candidate for future radar, navigation and mobile communications systems. To live up to their potentials, planar radiators are in need of accurate computer modeling methods, since experimental design approaches are too time-consuming and expensive. Computer programs should allow for accurate analysis, performance optimization of parameters and simple determination of manufacturing tolerances.

This dissertation presents a full-wave analysis tool for planar radiators and transmission lines. The technique is based on a rigorous spectral-domain method-of-moments solving procedure. It is capable of accounting for real-material parameters — finite conductivity of metals and non-zero conductivity of dielectrics — as well as metallic surfaces of non-zero thickness and substrates of finite extent.

A technique for the exact numerical evaluation of the two-dimensional generalized exponential integral is introduced. It makes the utilized method systematic and suitable for the analysis of even highly complex structures in an unambiguous way.

Performance of the method is tested in comparisons with measured data, in terms of input impedance and input reflection coefficient, of a number of planar radiators and transmission lines. On all accounts, good agreement is found. In addition, three types of microstrip-antenna feeding mechanisms are modeled, and radiation patterns of the corresponding antenna systems are presented. Again, good agreement with measurement — including radiation in the backward direction — results. Effects of finite-extent substrate are studied on a planar two-port. It is shown that they should not be neglected.

Examiners:

Dr. J. Bornemann, Supervisor (Dept. of Elec. & Comp. Engineering)

Dr. R. Vahldieck, Departmental Member (Dept. of Elec. & Comp. Engineering)

Dr. R.L. Kirlin, Departmental Member (Dept. of Elec. & Comp. Engineering)

Dr. S. Dost, Outside Member (Dept. of Mechanical Engineering)

Dr. L. Shafai, External Examiner (Dept. of Elec. & Comp. Engg., University of Manitoba)

TABLE OF CONTENTS

Abstract	ii
Table of Contents	iv
List of Figures	vi
Acknowledgment	xiii
1 Introduction	1
2 Planar Radiators	6
2.1 Single Patch Modeling	7
2.2 Mutual Coupling in Planar Antenna Arrays	15
3 Modeling Planar Radiators	20
3.1 Structures Involving Finite-Size Dielectric Regions	21
3.2 Modeling the Dielectric	23
3.3 Defining the Surface Impedance	24
3.4 Rooftop Representation	26
3.5 Scattering and Radiation Formulations	31
3.6 Calculations of F_A and F_S	38
3.7 Time Reduction Strategy	49

4	Polarization Charge in a Dielectric Cube	57
5	Input Reflection Coefficient of a Patch Antenna	62
	5.1 Approximate Solution	62
	5.2 Full-Wave Solution	65
6	Input Impedance of an Inset-Fed Patch Antenna	68
7	Further Remarks on Input Impedance/Admittance of Passive Components	73
	7.1 Bode's Integrals	74
	7.2 Input Impedance of a Short-Circuited Microstrip Transmission Line	86
8	Effects of Finite-Extent Substrate	91
9	Radiation Characteristics of Planar Antennas	96
	9.1 Coaxial Feeding	97
	9.2 Coupling to a Coplanar Transmission Line	100
	9.3 Aperture Coupling to a Microstrip-Line	104
10	Conclusions	110
	Bibliography	114
	Appendix — The Method of Moments	128

LIST OF FIGURES

1	Dielectric subdivision, with one cell removed for illustrative purposes.	23
2	Representation of junction currents. (a) At an external edge. (b) At a three-junction. (c) At a four-junction.	26
3	Diagram showing the use of thin-wall sections to model the dielectric and the use of rooftop functions to model the surface currents.	27
4	Surface currents in the $(i,j,1)$ layer, $i = 1, \dots, N_1, j = 1, \dots, N_2$, of a structure divided into $N_1=3, N_2=4$ and N_3 cells, respectively, in the x, y and z directions.	28
5	Falling half-rooftop and junction half-current associated with the current coefficient I_α .	36
6	Two adjacent cells, with currents at the common sidewall, the interface, standing out prominently.	37
7	Rectangular integration region in the Cartesian coordinate system, with some additional notation.	44
8a	Calculated real part of integral I_3 versus a . (Parameters: $x_1=0, x_2=5\text{cm}, y_1=-3\text{cm}, y_2=3\text{cm}, \text{frequency} = 2\text{GHz}$.) Solid line: 6-outer/3-inner-point Gaussian integration in polar coordinates according to (3-37); dashed	

- line: 3-outer/6-inner-point Gaussian integration in Cartesian coordinates according to (3-31); dash-dotted line: technique suggested in [62]. Inset: solid line: 6-outer/3-inner-point Gaussian integration in polar coordinates according to (3-37); dashed line: 96-outer/96-inner-point Gaussian integration in Cartesian coordinates according to (3-31). 47
- 8b Calculated imaginary part of integral I_3 versus a . (Parameters: $x_1=0$, $x_2=5\text{cm}$, $y_1=-3\text{cm}$, $y_2=3\text{cm}$, frequency = 2GHz.) Solid line: 6-outer/3-inner-point Gaussian integration in polar coordinates according to (3-37); dashed line: 3-outer/6-inner-point Gaussian integration in Cartesian coordinates according to (3-31); dash-dotted line: technique suggested in [62]. (Note that the values of the dash-dotted line labeled [62] are independent of a , because only one imaginary term, $-jk$, of the Maclaurin series of the integrand is respected in [62].) 48
- 9 Subdivided source region of the source current I_α and test interval of the target element upon which the voltage V_β is calculated. 50
- 10 Dielectric cube of sidelength $A=0.2 \times 10^{-4} \lambda_0$ and relative permittivity $\epsilon_r=9$ illuminated by a 1V/cm plane-wave incident electric field. Layers 1—4 correspond to the locations of computed current distributions in Figures 11 and 12. For symmetry reasons, only one half cube volume is of interest. 57
- 11 Polarization current distribution on layer 1 (c.f. Figure 10) of the cube according to [62]. 58

- 12 Polarization current distributions on layers 1—4 (c.f. Figure 10) calculated after implementing the integration procedure of this paper in the model of [62]. 60
- 13 Frequency dependence of the input reflection coefficient — amplitude (a) and phase (b) — for a rectangular patch of length 3.85 cm, width 3.18 cm, substrate thickness 1.568 mm and substrate relative dielectric constant 2.34, according to the simplified model of [111]. Solid line: calculation based on our exact numerical integration, c.f. (3-34); dotted line: calculation based on numerical tuning [111]; dashed line: measurement [29]. 64
- 14 Dimensions of asymmetrically edge-fed rectangular patch antenna. 65
- 15 Frequency dependence of the amplitude of the input reflection coefficient for the asymmetrically edge-fed patch of Figure 14. Solid lines of (a) and (b): full-wave calculation based on our exact numerical integration; dotted line of (a): measurement [69]; square markers of (a): significant calculated values according to [69]; dotted line of (b): our calculation under insufficient discretization (c.f. remarks at the end of Section 3), for demonstration purposes only. 67
- 16 Inset-fed rectangular patch antenna. 68
- 17 Two feeding mechanisms for the rectangular patch antenna of Figure 16. 69
- 18 Frequency dependence of input impedance — real (a) and imaginary (b) parts — for the inset-fed rectangular patch of Figure 16, with the substrate relative dielectric constant 2.33 and thickness 1.575 mm. Dashed line: calculation for the feeding mechanism according to Figure 17a; solid line: calculation for the

- feeding mechanism according to Figure 17b; dotted line: calculation as the solid line, with an increased-conductivity dielectric substrate ($\tan \delta = 0.01$); square markers: measurement [69]. 70
- 19 Input conductance of a wire antenna as a function of L/λ_0 . $q = 11.11$ (solid line) and $q = 33.33$ (dashed line). 79
- 20 Input susceptance of a wire antenna as a function of L/λ_0 . $q = 11.11$. The solid line is the direct method-of-moments solution and the dashed line is obtained through Bode's integrals. 80
- 21 Input susceptance of a wire antenna as a function of L/λ_0 . $q = 33.33$. The solid line is the direct method-of-moments solution and the dashed line is obtained through Bode's integrals, where the conductance was calculated at 400 frequency points. 82
- 22 Input susceptance of a wire antenna as a function of L/λ_0 . $q = 33.33$. The solid line is the direct method-of-moments solution and the dashed line is obtained through Bode's integrals, where the conductance was calculated at 50 frequency points. 83
- 23 Input conductance G of a wire antenna with $\pm 10\%$ (± 1.3 mS) of noise superimposed. (Note that negative conductances are eliminated by setting the respective values to zero.) 84
- 24 Calculated input susceptance B corresponding to conductance of Figure 23 (solid line) and conductance without noise (dashed line). The inset is the input susceptance calculated from only the first peak, $0 \leq L/\lambda_0 \leq 1$, of the conductance in Figure 23. 85

25	Geometry of the analyzed short-circuited section of a microstrip transmission line.	87
26	Feeding region and excitation currents of the structure depicted in Figure 25.	88
27	Frequency dependence of input impedance for the structure of Figure 25. Dotted line: calculated real part; solid line: calculated imaginary part.	88
28	Frequency dependence of input susceptance for the structure of Figure 25. Dashed line: obtained from input impedance; solid line: reconstructed through Bode's integrals.	89
29	Frequency dependence of input susceptance for the structure of Figure 25 as published in [62].	90
30	Topologies examined in study of effects of finite-extent substrates. Dimensions: $a=1.036$ mm, $b=2a$; dielectric thickness 1.423 mm, material properties are those of gallium arsenide at 25 degrees C. Port 2 matched.	91
31	Frequency dependence of input reflection coefficient — amplitude (a) and phase (b) — for the two-ports of Figures 30a (dashed line) and 30b (solid line).	93
32	Frequency dependence of transmission coefficient — amplitude (a) and phase (b) — for the two-ports of Figures 30a (dashed line) and 30b (solid line).	94
33	Frequency dependence of the total power radiated by the two-port of Figure 30b.	95

- 34 Coaxially fed rectangular patch antenna. 97
- 35a E-plane radiation patterns of the coaxially fed rectangular patch antenna of Figure 34 at 6.8 GHz. Solid line: calculated co-polarized; dashed line: measured co-polarized [135]; calculated cross-polarized below -60 dB. 98
- 35b H-plane radiation patterns of the coaxially fed rectangular patch antenna of Figure 34 at 6.8 GHz. Solid line: calculated co-polarized; dashed line: measured co-polarized [135]; dotted line: calculated cross-polarized. 99
- 36 Back-side view of rectangular patch antenna fed by coupling from a coplanar transmission line. Dimensions in millimeters. 101
- 37a E-plane radiation patterns of the microstrip patch antenna with coplanar feed line of Figure 36 at 4.3 GHz. Solid line: calculated co-polarized; calculated cross-polarized below -60 dB. 102
- 37b H-plane radiation patterns of the microstrip patch antenna with coplanar feed line of Figure 36 at 4.3 GHz. Solid line: calculated co-polarized; dashed line: measured co-polarized [136]; dotted line: calculated cross-polarized. 103
- 38 Expanded view of multilayer microstrip antenna comprised of parallel dipoles aperture-coupled to a microstrip line. Dimensions: $\epsilon_{r2} = 2.33$, $H_2 = 0.762$, $\tan \delta_2 = 0.0012$, $\epsilon_{r1} = 1.07$, $H_1 = 5.2$ mm, $\tan \delta_1 = 0.0004$, $A_l = 13.0$ mm, $A_w = 0.8$ mm, $\epsilon_{rf} = 2.2$, $H_f = 0.762$ mm, $\tan \delta_f = 0.0009$, $W_f = 2.32$ mm, $L_s = 3.0$ mm. 105

- 39 Detailed view of parallel resonators of Figure 39. Dimensions: $W_{x1} = 20.50$ mm, $W_{y1} = 0.25$ mm, $d_1 = 0.25$ mm, $W_{x2} = 17.80$ mm, $W_{y2} = 0.50$ mm, $d_2 = 2.00$ mm, $W_{x3} = 15.50$ mm, $W_{y3} = 0.50$ mm, $d_3 = 4.00$ mm. 106
- 40a E-plane radiation patterns of the microstrip antenna of Figure 38 at 5.24 GHz. Solid line: calculated co-polarized; dashed line: measured co-polarized [137]; calculated cross-polarized below -60 dB. 107
- 40b H-plane radiation patterns of the microstrip antenna of Figure 38 at 5.24 GHz. Solid line: calculated co-polarized; dashed line: measured co-polarized [137]; dotted line: calculated cross-polarized. 108

Acknowledgment

I enjoyed company — and valued friendship — of several open-minded, no-nonsense people who never failed to be there for me, accepted me for who I am and helped me feel at home in this country.

First and upmost, I express deep and abiding gratitude to my supervisor, Professor Jens Bornemann, who believed in me when no-one else would. Throughout the long haul called the graduate school, Jens was a patient — and tolerant — instructor (even when I was pushing my luck), a mentor and a touchstone for not pretending anything. I will never forget our lengthy discussions when, attempting to resolve a problem, in the heat of the debate, one of us would start a sentence and the other one would finish it — for, I have learned, in this is the true joy of engineering work. Also, I am grateful to Jens for financial support; my studies in Canada would not have been possible without it.

I thank Professor Ruediger Vahldieck for enduring my “twisted” sense of humor. His cool, integrity and deeply rooted capacity for fairness are qualities that I admire and strive to match. Although at times the two of us might have seemed like oil and water, it is my conviction that we stand for the same values, which is the only thing that really matters.

Thanks go to Dr. Benoit de la Filolie, a very French fellow who drives a Ford, for understanding that there is nothing that would beat the power and the rumble of a big V-8.

Last but not least, Dr. Smain Amari — one of a kind, a researcher with the soul of a poet. Your decency and civility, especially in life's adverse situations, are not easy to come by. Thank you for numerous insightful discussions and suggestions as well as for showing me not to be intimidated to say “the emperors have no clothes” when they, indeed, do not have any.

To my parents

1 INTRODUCTION

Next to the traditional microwave and millimeter-wave systems utilizations like radar, deep space communications and electronic warfare, numerous types of wireless communications systems are emerging from the prototype stage to mass applications. Personal communications services (PCS), direct broadcast satellite television, auto navigation aids, highway traffic controls, along with medical and agricultural applications, offer new market opportunities for microwave component and system suppliers. The systems, which are currently under development, will provide integrated communications and navigation services to consumers, including nationwide digital audio broadcasts; data broadcasts, such as traffic advisories, weather reports, travel databases, and stock and sports updates; precision navigation; and two-way voice and data communications.

Significant changes have also taken place in microwave equipment for space applications. One of the most clearly visible has been the reduction in mass and size, that is, miniaturization. For example, a satellite receiver at Ku-band, which had a mass of more than 5 kg in 1988, can now be made with improved performance and still weight less than 1.5 kg [1]. Circuits, whose sizes were once measured in centimeters, now have dimensions of the order of hundreds of microns. Impressive miniaturization has been achieved by the use of monolithic microwave integrated circuits (MMICs) fabricated on gallium arsenide (GaAs) semiconductor material. The favorable properties of GaAs permit passive and active microwave components, with good microwave performance, to be implemented on the same semiconductor chip. There has been a continuous improvement in the performance of MMICs over recent years due to the achievement of stable, well

controlled and reproducible manufacturing processes, yielding devices whose characteristics can now be modelled with high accuracy by computer aided design techniques. The technology of MMICs is now regarded as mature for space applications.

In addition to the wireless communications and space systems, there are other microwave and millimeter-wave applications, for example, imaging radars and radiometers, adverse weather landing systems [2], traffic management and highway automation systems, intelligent vehicle systems (collision warning and avoidance, near obstacle detection, blind spot detection, airbag arming, speed sensing, adaptive cruise control, vehicle identification, navigation, position tracking) [3]. However, microwave systems are not the sole contender for many of the applications listed. Ultrasonics, infrared, laser, optical and mechanical approaches compete for the high volume production business offered by the respective industries. Nevertheless, microwave technology offers advantages such as good penetration despite rain and fog, dimensional tolerances that are proportional to wavelength, and thus, parts are less difficult to fabricate than infrared or optical components. Its drawbacks include relatively large physical size as compared to infrared or optical systems, limited spectrum availability for automotive use and higher cost.

What all the aforementioned microwave applications have in common is that antennas are crucial parts of their systems; not uncommonly a system's antenna is the decisive component for selecting or rejecting the system for a particular application. For example, in imaging applications, microwave systems may be the desired technology, because antennas with beamwidths that provide good interference rejection along with adequate angular resolution are available. Similarly, in the automobile industry, microwave technology may be the technology of choice, for microwave subsystems based on MMICs (offering clear reductions in size and mass of on-board equipment, lower manufacture costs, high reliability and accurate repeatability) have sped up the development of phased-array and adaptive beamforming antennas that can be integrated into the surface of a car's body [3].

Also, a particular antenna can be the decisive factor in dictating performance, thus applicability, of a system. A textbook example of this are Global Positioning System (Navstar) receivers: The antenna of omnidirectional hemispherical coverage can take a variety of forms. Depending on receiver packaging, application and cost considerations, a monopole, dipole, quadrifilar helix (volute), spiral helix or microstrip patch radiator can be used. Microstrip patch radiators are most easily integrated into portable receiver packages and offer the highest zenith gain. However, their flat geometry leads to rapid falloff of coverage at elevations near 10 degrees above the horizon, a satellite elevation within the normal usable range of the system. While this characteristic will not degrade performance of fixed receivers, it can lead to loss of receiver lock on low elevation satellites when receivers are on mobile platforms subject to pitch or roll. The physical height of the other antenna types permits them to maintain their patterns to elevations as low as 10 to 20 degrees below the horizon [4].

To build an antenna for future applications, three major microwave technologies — complex beamforming networks, solid-state power amplifiers and *lightweight radiating elements* — need to be further developed. The understandable trend of wireless systems towards antennas that are compact, low in mass and volume and cheap to manufacture has naturally led to radiators that use the planar-transmission-line technology, the most common technology of contemporary microwave and millimeter-wave systems. At first, the radiators were positioned on the same surface as their feeding and beamforming networks. However, it was soon found out the transmission lines, especially when closely placed, interact with the radiators, usually adversely affecting the antennas' radiation properties in the process [5]. Thereafter, several alternative feeding mechanisms appeared. The most straightforward replaces the microstrip feeding with the coaxial one. Unfortunately, this necessitates via holes penetrating the substrate in order to connect the coaxial launcher with the radiating elements [6]; furthermore, all practical implementations of the launcher-radiator connection introduce undesirable parasitic effects, which are not easy to

either predict or determine and result in deteriorated performance as the operating frequency increases. Another option abandons via holes; instead, it uses a separate layer of metallization to couple energy to the radiators above [7]. A modification of that alternative is an arrangement that employs yet another structure, a metallic plane with one or more openings, placed above the feedlines and below the radiating patches, to ensure that the patches get excited exclusively at desired locations, by screening out all other electromagnetic coupling that exists between the feedlines and the radiators [8]—[10]. While advantageous and intuitively very elegant and orderly, both options have also a downside: they introduce one or two extra layers of metallization plus one or two extra layers of dielectric, respectively. Such a multilayer structure requires a significantly more complex manufacturing process, which translates into higher cost.

The need for a multilayer feeding network is evident in large arrays with a large number of power dividers or phase shifters. Due to space considerations, the spurious coupling between the network and the radiating elements, or between different parts of the network itself, can be significant enough to degrade performance. In addition, corporate feed network radiation can affect the sidelobe and cross-polarization characteristics of the array. Using a multilayer feed network located in a different plane than the radiating elements can alleviate these problems.

Planar transmission-line and radiating structures are an important factor in modern microwave and millimeter-wave communications systems. As the importance of the abovementioned applications and the brief introduction to the antenna problematics suggest, antenna development by trial and error methods is not economical. Contemporary antenna technologies are very powerful but also very complex. In order to reduce cost, computer codes of progressively increasing accuracy are needed. In antenna arrays, the most reasonable tradeoff appears to lie in developing computer-aided techniques for such antenna array analyses that would respect significant mutual coupling effects and neglect

minor contributions, thus enabling modeling on modern workstations with very little sacrifice in precision.

This dissertation attempts to fill up some of the gaps, by presenting an improved numerical model for full-wave analysis of imperfect planar radiators on lossy substrates of finite extent. The dissertation is organized as follows:

Section 2 reviews most significant publications on single planar antennas as well as antenna arrays; general concepts of antenna arrays and then specifics and mechanisms of planar antenna arrays are discussed.

The numerical model utilized in this study for analysis of planar radiating structures is described in Section 3. Implementation details and two time reduction techniques are presented and discussed.

Sections 4—6 present computed results, in terms of input impedance and input reflection coefficients, for a number of planar systems, in comparison with measurement.

The Kramers-Kronig relations are applied to antenna input impedances/admittances — and are proved to hold — in Section 7.

Results of a study of finite-extent-substrate effects in planar microwave circuits are presented in Section 8.

Section 9 shows radiation characteristics of three types of planar-antenna feeding mechanisms, in comparison with experimental results.

Finally, conclusions are drawn in Section 10.

2 PLANAR RADIATORS

The concept of patch antennas to create compact, lightweight, low cost, low volume, electrically thin radiating structures represents an intriguing development in antenna engineering. The fact that printed circuits do emit significant levels of radiation was found more than four decades ago, at the inception of stripline, but such radiation was generally regarded as an unwanted effect to be suppressed. It was found that the radiation could be reduced by employing thinner high permittivity substrates and narrower printed conducting strips, hence the name "microstrip".

The microstrip antenna concept dates back about 40 years to work in the U.S.A. by Deschamps [11] and in France by Gutton and Baissinot [12]. Shortly thereafter, Lewin [13] investigated radiation from stripline discontinuities. Additional studies were undertaken in the late 1960's by Kaloi, who studied basic rectangular and square configurations. However, other than the original Deschamps report, work was not reported in the literature until the early 1970's, when a conducting strip radiator separated from a ground plane by a dielectric substrate was described by Byron [14]. This half-wavelength-wide and several-wavelength-long strip was fed by coaxial connections at periodic intervals along both radiating edges; the concept of the aperture as a series of metal film elements mounted over and in close proximity to a conducting ground plane was established. Later, a microstrip element was patented by Munson [15], and data on basic rectangular and circular microstrip patches were published by Howell [16]. Weinschel [17] developed several microstrip geometries for use with cylindrical S-band arrays on rockets. Sanford [18] showed that the microstrip element could be used in conformal array designs

for L-band aircraft-satellite communications. Additional work on basic microstrip patch elements was reported in 1975 by Garvia *et al.* [19], Howell [20], Weinschel [21] and James and Wilson [22]. The early work by Munson on the development of microstrip antennas for use as low-profile flush-mounted antennas on rockets and missiles showed that this was a practical concept for use in many antenna system problems and thereby gave birth to a new antenna industry.

2.1 Single Patch Modeling

Of the various methods of analyzing microstrip antennas, the *transmission line model* (TLMod) is the simplest approach. This method uses the analogy between a rectangular microstrip patch and a section of a transmission line. Papers by Munson [23] and Derneryd [24] are two of the earliest reports outlining the method and its applications. The equivalent transmission line of the rectangular patch is terminated with edge admittances at the two ends, and transmission line network analysis is used to solve for the input impedance and voltages at the edges.

Bhattacharyya and Garg [25] have generalized the approach for applications to non-rectangular patch shapes, by replacing the uniform transmission line section with a non-uniform section of appropriate characteristics. The method is thus applicable to any shape for which separation of variables is possible within the wave equation expressed in the particular coordinate system.

Among other major papers on TLMod, Dubost [26] has extended the model to include the conductor and dielectric losses by using a lossy equivalent transmission line in the model. Dubost [27] has also described a non-uniform TLMod for an arbitrarily shaped patch; later Dubost and Beauquet [28] have applied this modified TLMod to a

circular patch antenna. A TLMod method has been developed, by Dearnley and Barel [29], to predict the input characteristics of rectangular microstrip antennas over a wide band of frequencies. The model has been later modified to include the mutual radiative coupling between the two ends and the influence of the side edges on the radiation conductance. Despite these modifications, the model is approximate, since it does not incorporate the effect of the transverse current on the patch, and it is not convenient to incorporate feedline junction reactances.

More recently, Bhattacharyya [30] investigated radiation characteristics of a wide rectangular patch antenna excited by a single feed. It was found theoretically that a single-feed wide rectangular patch supports a leaky traveling wave along the width of the patch. Though the paper presents interesting findings, it is more of academic importance, as single-feed wide rectangular patches (unlike multiple-feed ones, which have been used as wraparound antennas on missiles) do not have outstanding radiation characteristics.

Microstrip antenna analysis has been improved by replacing the one-dimensional transmission line model with the two-dimensional *cavity model*, where the substrate sandwiched by the upper and lower metallizations is treated as a cavity resonator with appropriate boundary conditions. In [31], two equivalent representations of fields below the patch are analyzed: the expansion into resonant modes and mode matching. It has been concluded that while the mode matching solution, in general, converges faster than the expansion into resonant modes, the expansion gives more physical insight for the antennas excited near a resonance mode. An improvement in the cavity model theory is reported in [32], which illustrates how the copper and the radiative losses associated with the radiating patch are lumped together with the dielectric loss to postulate an effective loss tangent. This leads to input impedance characteristics in good agreement with measurement for all modes and feed locations. The method is applicable to patch shapes for which the two-dimensional wave equation is separable.

An extension of the cavity method to more general shapes is discussed in [33] and [34], where the segmentation/desegmentation method of two-dimensional planar circuit analysis is used to decompose the configuration into a series of canonical shapes for which Green's function can be determined and the cavity method is applicable. Panisamy and Garg [35] avoid dividing the aperture into a number of ports. This makes the method more efficient, and the error previously introduced by assuming certain radiation losses for given segments is not present.

The need for more accurate design of microstrip patches and arrays stimulated the development of the *multiport network model* [36], which could be considered as an extension to the cavity model. Electromagnetic fields underneath the patch and outside the patch are modeled separately. Fields outside the patch — the fringing fields, the surface-wave fields and the radiation fields associated with the radiating edges — are modeled by equivalent lumped edge admittance networks (EANs). EAN is a multiport network consisting of parallel combinations of capacitances (representing the energy stored in fringing fields) and conductances (representing the power carried away by radiation and surface waves). Effects of mutual coupling between the radiating edges are incorporated by inserting a mutual coupling network.

Both the transmission line and the multiport network models require the knowledge of edge admittances for network modeling of fringing and external fields, hence the evaluation of input impedance and the frequency of resonance. A large number of papers was devoted to the evaluation of the edge admittance; usually they are referred to as *edge admittance models*.

The radiation conductance associated with the edge of a microstrip antenna is calculated by considering the slot between the edge of the patch and the ground plane as a radiating aperture. Many publications ([37]—[42] and references in [42]) provide simple design equations for the resonant frequencies and unloaded radiation Q-factors for

rectangular microstrip patches, using the thin-substrate approximation. An accurate characterization of an infinitely long microstrip edge has been carried out using Wiener-Hopf analysis [43] of a parallel plate dielectric loaded waveguide with a semi-infinite top plate. This analysis yields both the edge conductance and the edge susceptance; however, the results are accurate only for very wide patches. Moreover, it should be pointed out that, while all the analysis techniques mentioned in this paragraph lead to input impedance and resonant frequency results that are in fairly good agreement with measurement, they fail to predict reasonable radiation patterns; it is so because the fundamental idea of the techniques is not consistent with physical reality: radiation from a patch antenna is caused by the current distribution on the upper metallization rather than electromagnetic fields in the slot between the edge of the upper metallization and the ground plane. In that context, monograph [42], for example, is obsolete.

Many of the analyses mentioned so far are based on the quasi-static model of printed circuits. Independent of the efforts on antennas, microstrip and other printed circuit structures have been used in microwave and millimeter-wave integrated circuits. As the frequency of operation is increased, it has been known that the quasi-static analyses of microstrip circuit elements are not accurate enough (due to the approximations built into these models), and a more rigorous *full-wave analysis* is required. For instance, as for the analysis of microstrip disk resonators, a number of improved theoretical analyses appeared in the past [44], [45].

Paper [46] presents a full-wave analysis of an unloaded rectangular patch (without any feed arrangements) as an eigenvalue problem with complex eigenvalue (resonant frequency). All the wave phenomena are incorporated in the analysis. The method is based on the spectral domain immittance matrix approach. In the formulation process, the directions parallel to the substrate surface are completely separated from the normal direction by the use of the equivalent network for spectral waves. Galerkin's method

is used in the solution process, and numerical results are obtained for the complex resonant frequency and radiation pattern.

When sources of electromagnetic radiation are in the proximity, or on the interface, of electrically dissimilar materials, the resulting electromagnetic fields involve Sommerfeld-type integrals. If the source is near the interface, these integrals include exponentially decaying terms in the integrand which facilitate convergence [47]—[49]. A patch antenna can be seen as an extended source typically printed on a grounded dielectric substrate. In order to evaluate electrical properties of such an antenna, the current distribution must be obtained by solving Pocklington's integral equation, a Fredholm integral equation of the first kind [50].

Mosig and Gardiol [51] have outlined a general mixed potential integral equation formulation; the Green's functions belonging to the kernel of the integral equation are expressed as Sommerfeld integrals, in which surface wave effects are automatically included. Another paper [52] by these authors elaborates on the analytical and numerical techniques involved in full-wave analysis. Mosig [53] has applied these techniques to the analysis of arbitrarily shaped microstrip structures. Damiano [54] depicts the computational aspects of difficult numerical integrals (with complex poles and strong oscillations) involved in the analysis of patch antennas.

A variety of models — such as TLM, the cavity model and various moment method solutions [55]—[57] — exists for computing the input impedance of a microstripline fed patch antennas. These models generally simplify the feed by treating it as an equivalent current sheet and have been shown to give reasonable results for antennas on thin substrates of low dielectric constant material. However, in millimeter-wave applications, the above models often fail to give reasonable impedance results [58]. The reason for a simple feed model working well for electrically thin substrates is probably due to the fact that the antenna Q is very high for this case. Thus, the surface current on the patch is predominantly owing to the high Q resonance of the patch and is not greatly perturbed

by the details of the feed current. (This effect is shown graphically in [51].) When the substrate becomes thicker, the Q of the resonance becomes smaller, and the details of the actual feed current become more significant in relation to the total patch current. Pozar and Voda [59] have developed a rigorous solution to the problem of input impedance of a rectangular patch antenna fed by a microstripline. The currents on the feed line and the patch are expanded in a suitable set of modes, and a moment method solution is formulated in the spectral domain. Input impedance calculations are compared with measurements for high and low dielectric constant substrates. No radiation patterns have been presented in the paper.

Most of the research on patch antennas has been performed in the frequency domain, by the resolution of integral equations. Radiation characteristics of antennas, computed frequency-by-frequency, require much computer storage and time. In addition, the coaxial probe feeding is not easy to model. Herault *et al.* [60] reported a mixed method that associates transient analysis using an integral equation with harmonic analysis based on the solution of Pocklington's equation in terms of Hertz's potentials. The computation is done entirely in the time domain, followed by the Fourier transform. Then, the frequency-domain solution is used, with additional frequency-domain formulas, to calculate frequency characteristics. Relative importance of spherical space waves and cylindrical surface waves and their behavior in terms of substrate parameters and frequency are discussed for several particular configurations; the model, in general, does not accurately respect the presence of surface waves in the calculation of transient currents on the antenna surface.

More recently, Jackson and Alexopoulos [61] published closed-form expressions for the calculation of the radiation resistance, bandwidth and radiation efficiency of a resonant rectangular patch antenna, using asymptotic formulas derived from a rigorous Sommerfeld solution. The formulas become less accurate as the substrate thickness increases.

Rubin and Daijavad [62] have developed what is very likely the most sophisticated, albeit numerically very demanding, full-wave model in the field so far. It is a moment-method approach for calculating the scattered fields produced by structures that involve finite-size dielectric regions. The dielectric is first approximated by an array of interlocking thin-wall sections; the electric field boundary conditions are later applied through the use of appropriate surface impedances. Rooftop basis functions, chosen to represent the surface current, are placed on the thin-wall sections in such a way as to accurately represent the polarization current while preventing fictitious charge within the dielectric. The technique is applied to scattering from dielectric cubes and composite dielectric-conductor structures and to radiation from microstrip structures. More numerical results in comparison with measurement can be found in [63].

In recent years, the rectangular slot has been proposed as a means of power transfer between layers in multilayer printed antennas. Compared to probes, slots reduce fabrication complexity and allow more flexibility in the design of multilayer configurations. In the past, the aperture-coupled microstrip patch has been analyzed using the reciprocity theorem for the feeding line and the method of moments for the patch [64]. The same method is used in [65] for the analysis of an aperture-coupled patch fed by perpendicular coplanar strips. The perpendicularly fed aperture-coupled patch is a useful architecture by allowing more space for active circuits than single-layer or multilayer planar configurations.

The multilayer feeding network provides increased substrate area for feed networks, the possibility of an inherently symmetric feed network and a modular approach for design. In [66], the models for each transition (to another transmission line or a patch) were derived, using an extension of the analysis developed in [64]. A full-wave moment method is applied for the analysis of aperture coupled microstrip antennas [67].

The excitation of the parallel plate mode in stripline configurations is a serious concern in the design of multilayer feeding networks. Using either probes or slots

as means of power transfer between adjacent layers, this parasitic mode is always excited, and a considerable effort has to be made to assure its suppression. Paper [68] presented a new method that does not require via holes; instead, it uses striplines with two different dielectric substrates on the two sides of its center strip to solve the parallel-plate-mode problem.

Feeding is not a trivial matter even when a patch antenna is fed by means of a single-layer architecture. A combination of piecewise sinusoidal-pulse functions and semi-infinite microstrip current expansion functions is used in the full-wave spectral-domain method to analyze rectangular microstrip antennas [69]. Results show that the current on the feed line can substantially disturb the antenna radiation pattern.

Microstrip patch antennas typically have radiation patterns containing unwanted sidelobes or local minima caused by surface waves, especially when fabricated on high-dielectric-constant substrates. Communication [70] shows that removal of the substrate beneath the patch can greatly improve the pattern. A variation of the technique, compatible with monolithic fabrication, is applied to fabrication of a patch on GaAs and shows similar pattern improvement.

Another class of patch-antenna problems is related to the antenna bandwidth and gain. The bandwidth of a conventional antenna with a thin substrate (i.e., thickness smaller than 2 percent of free-space wavelength) and one patch layer is limited to often no more than 1 to 2 percent. The most straightforward means of improving the impedance bandwidth of a microstrip antenna is to use an electrically thick dielectric substrate. Unfortunately, the thick substrate causes an inductive shift in the input impedance [71], requiring the use of a compensating input network, which increases the design complexity and production costs. One solution to increased bandwidth may be the use of an electromagnetically-coupled microstrip structure. In this case, the patch is not connected to the probe, i.e., there is a small gap between the top of the probe and the patch of about 0.25 mm. Such a design offers an impedance bandwidth of approximately 50 percent. Another

popular structure with an improved impedance bandwidth is a stacked microstrip antenna capable of bandwidths ranging from 5 to 20 percent [72], [73]. A stacked microstrip array antenna usually has two closely spaced resonance frequencies, which result in a larger bandwidth. To overcome the shortcoming of low gain, several gain enhancement methods relying on substrate-superstrate resonance have been proposed and discussed [74]—[77].

A few other methods that are well established in the electromagnetic theory, for example, the finite-difference time-domain method [78] or the method of lines [79], have been utilized to develop new full-wave analysis techniques. They do not appear to have the potential to surpass the merits of the previously described procedures, which renders them of practical importance for only a very specific, almost custom-made type of problems.

In general, full-wave analyses of patch antennas are computationally complicated, and it is difficult to envision that they will become a day-to-day working tool for antenna designers. Nevertheless, the results obtained by full-wave analyses have been incorporated into design procedures based on the equivalent transmission line, cavity or multiple network approaches discussed earlier.

2.2 Mutual Coupling in Planar Antenna Arrays

The ever-increasing demands of the space and missile age upon modern radar and communication systems have propelled phased array antennas into the limelight. The need for specialized multifunction operation (i.e., simultaneous surveillance, discrimination, tracking, etc.), coupled with high power, high data rates and the ability to withstand adverse environmental conditions, has stimulated considerable activity in the research, design and deployment of phased array radars and antennas. Phased array antenna systems have been

deployed on the ground, aboard ships and due to the miniaturization of components also aboard aircraft and spacecraft as well.

In what may be termed "classical" array theory [50], [80], the mutual coupling between the array elements is neglected. However, experimental and theoretical investigations have clearly indicated that mutual coupling cannot be ignored, especially in the case of closely spaced array elements (i.e., spacing of the order of half a wavelength). The mutual coupling strongly affects the radiation and reflection characteristics (as a function of the beam pointing direction) of phased array antennas. Furthermore, in a finite sized array, the radiation patterns and the reflection characteristics of the various elements may depend on their relative positions in the array. They are strongly influenced by the proximity of an element to the edge of the array. In the case of "large" planar arrays, however, the bulk of the inner core elements behave almost uniformly, and the important aspects of this behavior may be approximated well by the uniform behavior of elements in an infinite array. Thus the infinite array can serve as a useful model for the analysis of large planar arrays. In this case, the array radiation pattern can still be expressed as a product of the array factor and the element radiation pattern, the latter being determined in an infinite array environment. The effects of mutual coupling are taken care of by the element radiation pattern (excited in the array environment with the rest of the elements being properly terminated). Certain general expressions that relate the mutual coupling coefficients, the reflection coefficients and the radiation power pattern of an element can be derived.

The number of papers on antenna arrays published in just the last decade, or so, is overwhelming. Yet one may find it surprising how few significant publications on the mutual coupling in antenna arrays are available in the literature. Much of that can be attributed to inadequate computer technology (insufficient memory capacity, slow execution, etc.) in the past; however, it is also a fact that the modeling of mutual coupling effects still is — employing a metaphor — only in its infancy.

In 1966, Galindo and Wu [81] have pointed out that the radiation impedance of an antenna element in a phased array varies with the angle of scan because of mutual coupling between the radiating elements. Shortly thereafter, the authors derived a variational expression directly for the coupling coefficients, in terms of the array aperture field that exists when only a single element is excited [82]. In [83], the conventional problem of two arbitrarily located antennas is solved by using an integral equation technique. The approximate solution can be extended to a general array of N parallel elements. Agrawal and Lo [84] have studied mutual coupling effects in phased arrays with randomly located elements. Two main effects of coupling are separately considered: the increase in the sidelobe level (it is found that the increase is noticeable only for small average spacing — i.e., less than 2.5 wavelengths) and the fluctuation of mainlobe amplitude as a function of the scan angle (the fluctuations are found small if the average spacing is above 5.0 wavelengths). An important contribution of this theory is a method for the removal of blind angles.

In 1972, Amitay, Galindo and Wu published a book [85] that hitherto is the most comprehensive monograph on mutual coupling in phased arrays. Emphasis is placed upon the analysis of open ended waveguide type array elements in terms of scattering parameters.

A general formulation for aperture problems in terms of the method of moments is given in [86]. It applies to any two regions isolated except for coupling through the aperture. In [87], explicit formulas for a rectangular aperture in a conducting plane excited by an incident plane wave have been derived.

Jedlicka's paper [88] is perhaps the most quoted reference on the mutual coupling between two rectangular and circular patches. Coupling between L-band rectangular, nearly square and circular microstrip antennas has been investigated experimentally by a series of measurements of scattering parameters. The experiments demonstrated that for 1/16-inch and 1/8-inch substrates the surface wave coupling is

negligible and the predominant coupling mechanism is via the space wave. Measured results indicate that the coupling levels encountered for thin microstrip elements at L-band should not cause insurmountable problems in a patch antenna design.

Paper [55] is a moment method solution to the problem of input impedance and mutual coupling of rectangular microstrip antenna elements. The formulation uses the grounded dielectric slab Green's function to account rigorously for the presence of the substrate and surface waves. Another paper by Pozar, [89], analyzes phased arrays of rectangular patches in terms of reflection coefficient magnitudes. A full-wave analysis of mutual coupling between electromagnetically coupled printed dipoles has been reported in [90]. Surface wave coupling between circular microstrip patches is discussed in [91]. It is shown that the surface wave coupling decreases much more slowly than the space wave coupling and it increases rapidly with the substrate thickness.

Two companion papers [92], [93] describe a general solution to a class of printed antenna geometries composed of multiple dielectric layers or ground planes, radiating patches, dipoles or slots and an arbitrary configuration of multiple transmission lines proximity coupled or aperture coupled to the radiating elements. The solution uses a full-wave spectral-domain moment method approach and a generalized multiport scattering formulation to model the excitation from the multiple feed lines. The method, however, is unable to handle direct coupling between transmission lines or losses of any kind.

The method of papers [94] and [95] for the analysis of finite arrays is based on an infinite array approach, where the edge effects are taken into account by convoluting the infinite array results with the Fourier transform of the current distribution window on the array. The procedure is based on the use of Poisson's sum formula in the case of finite arrays, as was initially proposed by Ishimaru *et al.* [96]. One advantage of the method is that the size of the finite array to be analyzed has no influence on the computer time or memory required.

Finally, in [97] mutual coupling between two printed antennas is studied, and coupling versus element separation is presented for substrate parameters of practical interest. For certain substrate parameters, it was found that the magnitude of mutual coupling does not decay monotonically with increasing element separation. Instead, the magnitude exhibits a quasi-periodic oscillation which can be attributed to the interference of surface and space waves.

An assortment of papers on various patch antenna feeding mechanisms, patch antennas with layered substrates, dielectric-covered microstrip antennas, stacked patch antennas, etc. — either in single- or array-antenna configurations — can be found in the literature. Their review is beyond the scope of this document.

Vast majority of these reports, however, is confined to the analysis of lossless structures, assuming metallizations made of perfect conductors and substrates and superstrates made of perfect dielectrics. Very little of performance under lossy conditions has been revealed. Similarly, effects of finite sized substrates and the proximity of radiating elements to the substrate edges have not been studied either.

Utilizing a numerical model that is able to account for finite-conductivity conductors and nonzero-conductivity dielectrics, this dissertation will address these issues. The numerical model is not intended to become a day-to-day tool for antenna analysis or design (contemporary computer technology does not yet allow it) — rather it is envisioned as a means to shed more light on the extent to which the addressed phenomena affect antenna performance and, once aware of the effects, serve as a basis for specifying limitations of current analysis techniques and making proper adjustments in antenna design procedures if needed.

3 MODELING PLANAR RADIATORS

The problems of electromagnetic theory usually lead to partial differential equations, more rarely to ordinary differential equations, which have to be integrated under the initial or boundary conditions corresponding to the given problem. From the practical viewpoint, the evaluation of numerical, albeit approximate, values of the required quantities is of considerable interest. Perhaps the best devices for this purpose are the so called *direct methods*. Direct methods are those methods for the approximate solution of the problems of the theory of differential and integral equations that reduce these problems to finite systems of algebraic equations [98]. In theory and the practical applications of direct methods, we often come across a fact of prime importance. In many cases it is possible to replace the problem of integrating a differential equation by the equivalent problem of seeking a function which gives a minimum value to some integral. Problems of such a type are called *variational problems*; thus, the fact referred to above implies that in many cases the problem of integrating a differential equation can be replaced by some equivalent variational problem. The methods which allow us to reduce the problem of integrating a differential equation to the equivalent variational problem are usually called *variational methods*. There are many names associated with variational methods; included among them are Rayleigh, Ritz, Galerkin, Hilbert, Courant, Tonelli and Trefftz.

One of the direct methods is closely associated with the name of B.G. Galerkin. In his paper [99] published in 1915, Galerkin solved a number of problems on the equilibrium and stability of rods and plates. The method that he applied is identical in form to the method obtained by Bubnov [100]; however, Galerkin's essentially new contribution

was the fact that he did not connect his method with any variational problem, so that it could be applied to any differential (and not only differential) equation and it did not require the orthogonality of the coordinate functions, which was the requirement set up by Bubnov.

In the 1960s, Harrington applied the *method of moments* to the problems of the electromagnetic theory. The concept of the method is very general, and almost any solution, analytical or numerical, can be interpreted by it. For example, the classical eigenfunction approach corresponds to the particular choice of eigenfunctions for expansion and testing. The Rayleigh-Ritz variational method and Galerkin's method are closely related to it (the Galerkin method can be viewed as a special case of the method of moments), and so on. Harrington's monograph [101] presented a unified approach to the solution of field problems using computers and has long ago become a classical book. Detailed expositions to the method can be found in the monograph; to keep the dissertation selfcontained, a brief description of the method is given in Appendix.

3.1 Structures Involving Finite-Size Dielectric Regions

Numerous papers have appeared that consider the propagation, radiation or scattering in structures composed of conductors and dielectrics. However, when one considers the solution techniques that apply to arbitrary geometries, the number of approaches is reduced to a few. Most popular are moment methods that employ either volume elements to represent both conduction and polarization currents [102], [103] or surface equivalence principles [104], and finite methods that employ either finite-element or finite-difference techniques [78]. The approaches rely on the use of subsectional basis functions in the formulation and solution of the problem. The term "subsectional" refers to the use of a set of functions to represent the unknown quantity, which is often the current, with the property

that each function is non-zero only over a certain region, or subsection, of space. An appropriate linear combination of such functions represents the solution, with the coefficients of the basis function being the unknowns.

The first two approaches are often referred to as integral methods. Each unknown in an integral method is directly related to all other unknowns, with the result being a matrix equation where most of the matrix elements are non-zero. On the other hand, each unknown in a finite method is directly related to only those unknowns associated with neighboring basis functions, but indirectly related to all others, through chains of such nearby interactions. Finite methods give rise to sparse matrices.

Each of the above approaches is best suited for a particular subset of the general case. For example, the first approach, which is also referred to as a volume approach (since the basis functions appear wherever conductors or dielectrics exist), is not suited for large dielectric regions but can easily handle anisotropies. Finite approaches are efficient for structures that are dense, involving little empty space, but are not well-suited for radiation problems. Fortunately, generally there is an overlap for a given problem, permitting various checks on accuracy and opening the door for competing claims by proponents of different methods.

In this dissertation, only the first approach will be addressed. The numerical model utilized here is based on the method-of-moments algorithm presented in [62]. However, our theoretical approach is "selfconsistent" in the way the theory is presented and, therefore, differs to some degree from that of [62]. The conduction as well as polarization effects are represented by two-dimensional surface currents and surface impedances. The advantage is that the entire structure under analysis can be viewed as existing in a homogeneous dielectric, so that free-space Green's functions are used, and the same set of basis functions represents both conduction and polarization currents. The method is applicable to highly diverse set of structures, which makes it suitable for general purpose analysis.

3.2 Modeling the Dielectric

To represent the volume polarization with surface currents, the dielectric region is first replaced with a thin-wall mechanism employed by Harrington and Mautz [105]. As shown in Figure 1, the dielectric is subdivided into sections along the Cartesian coordinates, so that the region is composed of three-dimensional cells that have dimensions τ_x , τ_y and τ_z . If the dielectric material is pushed out from the center of each cell until it is compressed to zero thickness on the cell walls, a new structure that is composed only of these zero-thickness cell walls is formed. During compression, as the wall thickness κ goes to zero, the dielectric constant of the wall material goes to infinity as $1/\kappa$. Provided the grid is sufficiently fine with respect to wavelength and to feature size, and provided the walls are properly modeled, this thin-wall structure is essentially equivalent to the solid dielectric. After all, if a material was so constructed with very fine cells, it would be virtually impossible to ascertain the microscopic dielectric nature through bulk electrical measurements.

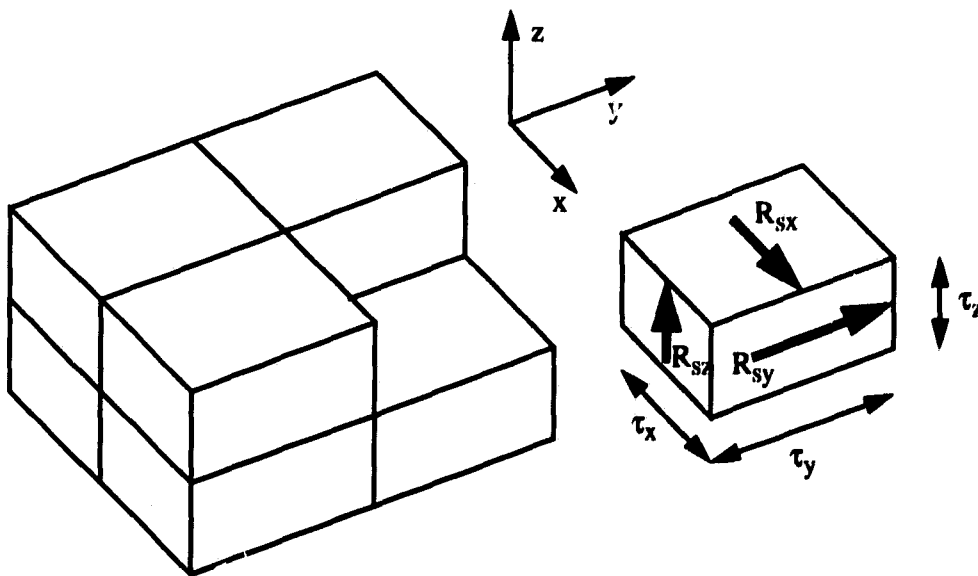


Figure 1. Dielectric subdivision, with one cell removed for illustrative purposes.

3.3 Defining the Surface Impedance

We choose a sheet impedance — or equivalently the surface impedance, because the sheets have zero thickness — such that the impedance is the same between two planes that sandwich a cell of either the solid dielectric or the thin-wall structure. Applying the volume equivalence theorem [106], we include only the contribution related to the volume polarization; in other words, we omit the free space contribution. This is a major advantage of this formulation, as the environment of a circuit (assumed here as free space) need not be incorporated in the modeling procedure. From Figure 1, the total impedance R_x [Ω] along the x direction for a single cell of solid dielectric is

$$R_x = \frac{\tau_x}{j\omega\epsilon_0(\epsilon_r - 1)\tau_y\tau_z}, \quad (3-1)$$

where ω is the angular frequency, ϵ_0 is the permittivity of free space, ϵ_r is the relative dielectric constant, and $\exp(j\omega t)$ is the time dependence. For the thin-wall structure, the surface impedance must be such that when multiplied by length τ_x and divided by perimeter $2(\tau_y + \tau_z)$, the result is again R_x . Thus, the surface impedance along x , R_{sx} [Ω], is given by

$$R_{sx} = R_x \frac{2(\tau_y + \tau_z)}{\tau_x} = \frac{2\left(\frac{1}{\tau_y} + \frac{1}{\tau_z}\right)}{j\omega\epsilon_0(\epsilon_r - 1)}. \quad (3-2)$$

For walls common to two cells, which may or may not have the same dielectric constant, R_{sx} would be the parallel combination of the two individual impedances. Through permutation of x , y and z , (3-2) also gives the surface impedances along y and z , namely R_{sy} and R_{sz} . Lossy dielectrics and lossy conductors are handled through the introduction of complex permittivity

$$\epsilon = \epsilon' - j\epsilon'' = \epsilon_0\epsilon_r - j\frac{\sigma}{\omega}, \quad (3-3)$$

where σ is the conductivity of the material.

The electric field boundary condition, applied over each dielectric cell wall and conductor surface, is

$$\mathbf{E}_t^{scat} - \mathbf{J}_s R_s = -\mathbf{E}_t^{inc}, \quad (3-4)$$

where \mathbf{E}_t^{scat} [V/m] is the tangential scattered electric field, \mathbf{E}_t^{inc} [V/m] is the tangential incident electric field, \mathbf{J}_s [A/m] is the sheet current density and R_s is the appropriate surface impedance. For dielectric volumes, R_s is either R_{sx} , R_{sy} or R_{sz} . For perfect conductors, R_s is zero, and for imperfect conductors it may be determined through skin-effect considerations — for example, recalling that depth of penetration in a conductor is [107]

$$\delta = \sqrt{\frac{2}{\omega\mu\sigma}}, \quad (3-5)$$

where μ is permeability of the material, the surface impedance as defined above can be expressed as

$$R_s = \frac{1+j}{\delta\sigma}, \quad (3-6)$$

provided the thickness of metallization is much larger than δ [108]. From practical applications it appears that (3-6) can be used as long as the metallization thickness is greater than 3δ [107], [109].

To summarize, the use of the thin-wall alternative is a two-step procedure. The first step is the replacement of the original dielectric by an equivalent structure, and the second step is the modeling of the equivalent structure. Having justified the use of the equivalent structure, we now describe the basis functions used to model it.

3.4 Rooftop Representation

On the edges of individual cells, we define corner currents, which are mathematically represented by corner functions. As depicted in Figure 2, three types of junctions can occur: at an external edge, only one corner function is needed (Figure 2a); at three- and four-junctions, respectively, two and three corner functions are used, as shown in Figures 2b and 2c. Because current flows continuously around each corner function, the total current into a junction must be zero; only one, two and three corner functions, respectively, are linearly independent. Using more would ultimately lead to a singular impedance matrix.

Each junction current is associated with a pair of two half-rooftops (Figure 2a), one rising and one falling. The two half-rooftops create one full rooftop and represent the basis function of the particular junction current in the method-of-moments formulation. As each cell has twelve edges, by itself it contains twelve junction currents. The relationships between thin-wall sections and the rooftop functions that model the surface currents are shown in Figure 3.

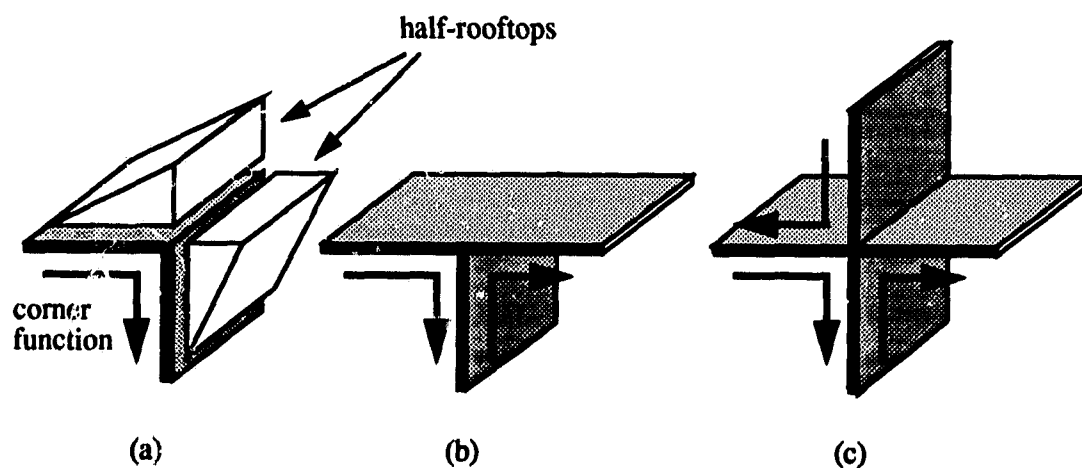


Figure 2. Representation of junction currents. (a) At an external edge. (b) At a three-junction. (c) At a four-junction.

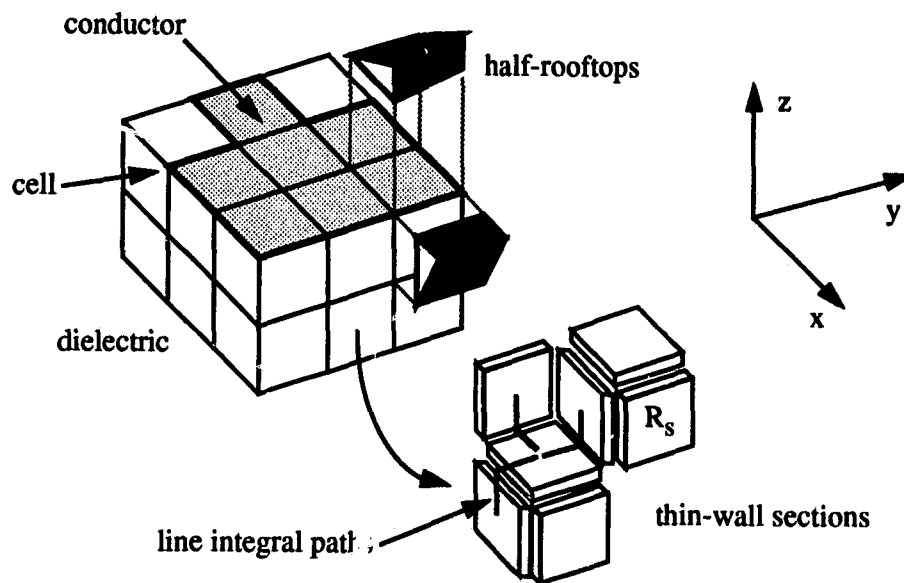


Figure 3. Diagram showing the use of thin-wall sections to model the dielectric and the use of rooftop functions to model the surface currents.

Let us consider a structure divided into N_1 , N_2 and N_3 cells, respectively, in the x , y and z directions. Surface currents in the $(i,j,1)$ layer, $i = 1, \dots, 3, j = 1, \dots, 4$, are depicted in Figure 4. The number of corner currents in the layer is $12N_1N_2 - (N_1-1)(N_2-1)$, for the layer contains $(N_1-1)(N_2-1)$ four-junctions. By analogy, the total number of corner currents in the entire structure, P , is $12N_1N_2N_3 - N_1(N_2-1)(N_3-1) - N_2(N_1-1)(N_3-1) - N_3(N_1-1)(N_2-1)$; after the arithmetics is performed,

$$P = 9N_1N_2N_3 + 2(N_1N_2 + N_1N_3 + N_2N_3) \cdot N_1 - N_2 - N_3 \quad (3-7)$$

In other words, the average number of corner currents per cell, P_{cell} , is

$$P_{cell} = 9 + 2\left(\frac{1}{N_1} + \frac{1}{N_2} + \frac{1}{N_3}\right) - \left(\frac{1}{N_1N_2} + \frac{1}{N_1N_3} + \frac{1}{N_2N_3}\right). \quad (3-8)$$

Upon inspection, $9 < P_{cell} \leq 12$. The extreme case of $P_{cell} = 12$ exclusively describes the $N_1 = N_2 = N_3 = 1$ configuration; if at least one of N_1, N_2, N_3 is greater than 1, which is true in virtually all practical applications, $9 < P_{cell} \leq 11.5$. The larger the values of N_1, N_2 and N_3 , the closer P_{cell} gets to nine.

We can come to the same conclusion by following a more straightforward line of thought: At each cell-edge internal to the structure, three corner rooftop functions appear (Figure 2c). Nine basis functions per cell are required to represent large dielectric volumes, considering that there are twelve edges per cell but that each edge is shared by four neighboring cells.

The forcing of currents to be continuous around bends, by combining half-rooftops to form corner functions, full rooftops, guarantees a smoother current distribution.

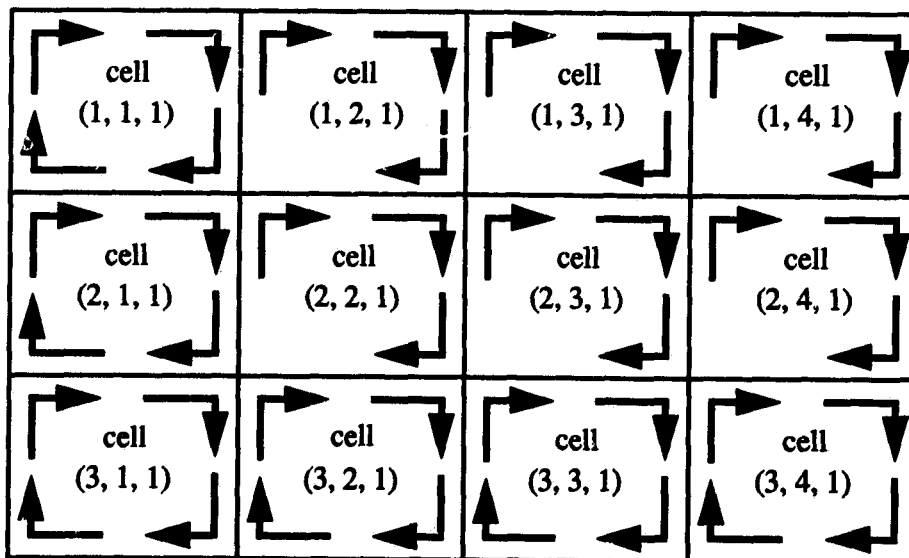


Figure 4. Surface currents in the $(i,j,1)$ layer, $i = 1, \dots, N_1$, $j = 1, \dots, N_2$, of a structure divided into $N_1=3$, $N_2=4$ and N_3 cells, respectively, in the x , y and z directions.

Mathematically, this is accomplished by making the coefficients of associated half-rooftops equal. This prevents the introduction of bound line charges that physically do not exist. Furthermore, we incorporate another mechanic that does not allow the introduction of fictitious charges — we extend the longitudinal bases of rooftop functions beyond the actual currents; this creates a system of mutually *overlapping* corner functions, which ensures that the resulting current distribution is *continuous*.

The use of surface currents to represent a volume current distribution is analogous to the use of a wire grid to represent a surface for scattering or radiation purposes [110]—[112]. In either case, the basis functions have one fewer dimension than the actual current distribution. In wire-grid modeling, the current is defined over segments having finite length but zero radius. Because the inductance of a filament becomes infinite as its radius approaches zero, to model a surface, the filament must be given an effective radius; this is usually accomplished by testing the electric field at a position radially offset from the filament. The choice of radius does affect the scattered field, so that considerable skill is required to obtain reasonable results. Fortunately, a surface current is more physical (a surface is two dimensional and, therefore, has finite inductance), and our approach requires neither the tuning that a wire approach does nor the quasi-tuning that results from the approximate numerical integration introduced by the authors of the paper that this dissertation is based on [62]. The validity of this representation will become evident through the examples.

As already indicated, large dielectric volumes require nine full rooftops, basis functions. This compares with only three for wire-grid, three-dimensional pulse or three-dimensional rooftop representations. However, the actual number of basis functions per cell, alone, is not a sufficient indicator of the efficiency of such an approach. Often, a smoother basis function can produce results of the same or better accuracy than another, so that fewer cells may be needed to solve a particular problem. In particular, for linear antenna problems, fewer linear basis functions (overlapping triangles) are needed than

pulse functions [101]. In the approach presented here, the linear fit (along one direction of the rooftop), the absence of fictitious charges and the versatility afforded, yield significant advantages.

One of the intriguing properties of the surface-current model based on the thin-wall structure is that the problem can no longer be solved through standard circuit analysis, since there are no longer any nodes: junctions are formed where as many as four sheets (thin walls) intersect, and these junctions are not points, but lines. Because each sheet supports current in two orthogonal directions, there is — in general — a voltage drop across these line junctions, and this precludes treating them as circuit nodes. Since any electromagnetic problem corresponds to a physical structure having well-defined boundary conditions, it clearly can be solved by defining an appropriate set of surface basis functions and using either integral or finite techniques. For example, at higher frequencies, a full-wave solution could be obtained as follows in Section 3.5.

The representation of currents, as described, can be used to solve scattering, radiation and propagation problems. The significant feature is the use of the equivalent, thin-wall structure to represent the dielectric and conductor regions, and the use of rooftop functions to model the surface current density on any conductors or thin-wall regions.

To solve a particular problem, after representing the current flow on the structure, one needs to generate a matrix equation. This involves testing the electric field at a sufficient number of places to obtain a matrix equation. In determining the electric field, one may employ the intermediate use of potentials, such as scalar and vector potentials, or work directly with the field quantities. One may employ testing functions that are the same as the expansion functions (the Galerkin procedure) or use another set of testing functions, such as the line functions that are chosen here. The procedures for generating appropriate matrix equations are now to be described.

3.5 Scattering and Radiation Formulations

A three-dimensional rectangular region that encloses the structure is defined and subdivided into N_1 , N_2 and N_3 sections along the coordinate axes. The region has dimensions along the x , y and z directions of d_1 , d_2 and h . For consistency with τ_x , τ_y and τ_z shown in Figure 1, $N_1 = d_1/\tau_x$, $N_2 = d_2/\tau_y$, and $N_3 = h/\tau_z$. The structure is fitted with full and half-rooftop functions. The current distribution on the structure, and this includes both the conduction and polarization currents, is approximated by a linear combination of rooftop-shaped functions.

The following are unit vectors directed along a positive axis direction and associated with the rooftop function having index α . Let $\mathbf{e}_{u\alpha}$ be along the direction of current flow, let $\mathbf{e}_{w\alpha}$ be normal to the plane containing the rooftop, and let $\mathbf{e}_{v\alpha}$ be orthogonal to both $\mathbf{e}_{u\alpha}$ and $\mathbf{e}_{w\alpha}$. Defining variables u , v , w , $\tau_{u\alpha}$, $\tau_{v\alpha}$ and $\tau_{w\alpha}$ in terms of x , y and z — where \mathbf{e}_x , \mathbf{e}_y and \mathbf{e}_z are unit vectors along the x , y and z axes, respectively — as

$$\begin{aligned}
 u &= \mathbf{e}_{u\alpha} \cdot (x\mathbf{e}_x + y\mathbf{e}_y + z\mathbf{e}_z) \\
 v &= \mathbf{e}_{v\alpha} \cdot (x\mathbf{e}_x + y\mathbf{e}_y + z\mathbf{e}_z) \\
 w &= \mathbf{e}_{w\alpha} \cdot (x\mathbf{e}_x + y\mathbf{e}_y + z\mathbf{e}_z) \\
 \tau_{u\alpha} &= \mathbf{e}_{u\alpha} \cdot (\tau_x\mathbf{e}_x + \tau_y\mathbf{e}_y + \tau_z\mathbf{e}_z) \\
 \tau_{v\alpha} &= \mathbf{e}_{v\alpha} \cdot (\tau_x\mathbf{e}_x + \tau_y\mathbf{e}_y + \tau_z\mathbf{e}_z) \\
 \tau_{w\alpha} &= \mathbf{e}_{w\alpha} \cdot (\tau_x\mathbf{e}_x + \tau_y\mathbf{e}_y + \tau_z\mathbf{e}_z)
 \end{aligned} \tag{3-9}$$

the volume current density \mathbf{J} [A/m^2] may be compactly expressed as

$$\mathbf{J} = \sum_{\alpha=1}^P R_{\alpha}(x, y, z) I_{\alpha} \mathbf{e}_{u\alpha}, \tag{3-10}$$

where $R_{\alpha}(x, y, z)$ [$1/\text{m}$] is the rooftop function centered at $x = x_{\alpha}$, $y = y_{\alpha}$, $z = z_{\alpha}$, I_{α} [A/m] is the corresponding current coefficient, and P is the total number of rooftop functions,

defined by (3-7). Using the same notation as in (3-9), the rooftop function may be expressed as

$$R_{\alpha}(x, y, z) = q_{\tau_{u\alpha}}(u - u_{\alpha}) p_{\tau_{v\alpha}}(v - v_{\alpha}) \delta(w - w_{\alpha}), \quad (3-11)$$

where $q_{\tau}(u)$ is the triangle function defined as

$$q_{\tau}(u) = \begin{cases} 1 - \left| \frac{u}{\tau} \right| & -\tau \leq u \leq \tau \\ 0 & \text{elsewhere} \end{cases}, \quad (3-12)$$

$p_{\tau}(v)$ is the pulse function defined as

$$p_{\tau}(v) = \begin{cases} 1 & -\tau/2 \leq v \leq \tau/2 \\ 0 & \text{elsewhere} \end{cases}, \quad (3-13)$$

and $\delta(w)$ [1/m] is the Dirac delta function. Associated with each rooftop α is a line interval, or integration path (see Figure 3), over which the electric field is tested. This interval is defined by its end points, located at $(u_{1\alpha}, v_{\alpha}, w_{\alpha})$ and $(u_{2\alpha}, v_{\alpha}, w_{\alpha})$, where

$$\begin{aligned} u_{1\alpha} &= u_{\alpha} - \tau_{u\alpha}/2 \\ u_{2\alpha} &= u_{\alpha} + \tau_{u\alpha}/2 \end{aligned} \quad (3-14)$$

As an example, for a rooftop that lies in the yz plane and has current directed along the y direction, $R_{\alpha}(x, y, z) = \delta(x - x_{\alpha}) q_{\tau_y}(y - y_{\alpha}) p_{\tau_z}(z - z_{\alpha})$ and $u_{1\alpha} = y_{\alpha} - \tau_y/2$ and $u_{2\alpha} = y_{\alpha} + \tau_y/2$.

The above expressions apply only for a full rooftop. For a half-rooftop that is rising (falling) along the positive axis direction, the upper (lower) bound of the inequality in the triangle definition (3-12) is replaced by 0, and $u_{2\alpha}$ ($u_{1\alpha}$) in (3-14) is set equal to u_{α} . The variables defined by (3-9) allow for a more compact mathematical representation of the various currents and field quantities. Any of the following equations may be expressed explicitly in terms of x , y and z through substitutions from (3-9).

The electric field produced by the current distribution (3-10) is calculated using scalar and vector potentials and may be expressed as

$$\mathbf{E}^{scat} = -j\omega\mathbf{A} - \nabla\Phi, \quad (3-15)$$

where \mathbf{A} [Vs/m] is the vector potential, given by

$$\mathbf{A} = \frac{\mu_0}{4\pi} \iiint \frac{\mathbf{J}e^{-jkr(x-x', y-y', z-z')}}{r(x-x', y-y', z-z')} dx' dy' dz', \quad (3-16)$$

and Φ [V] is the scalar potential, given by

$$\Phi = \frac{1}{4\pi\epsilon_0} \iiint \frac{\rho e^{-jkr(x-x', y-y', z-z')}}{r(x-x', y-y', z-z')} dx' dy' dz', \quad (3-17)$$

where

$$r(x, y, z) = \sqrt{x^2 + y^2 + z^2}, \quad (3-18)$$

$$k = \omega\sqrt{\mu_0\epsilon_0},$$

μ_0 is the permeability of free space, x , y and z are the field coordinates, and x' , y' and z' are the source coordinates. The charge density ρ [C/m³] is expressed in terms of the current density through the continuity equation

$$-j\omega\rho = \nabla \cdot \mathbf{J}. \quad (3-19)$$

Combining (3-10), (3-11) and (3-16), \mathbf{A} may be expressed in terms of the current coefficients as

$$\mathbf{A} = \frac{\mu_0}{4\pi} \sum_{\alpha=1}^P I_{\alpha} \mathbf{e}_{u\alpha} F_{\alpha}, \quad (3-20)$$

where

$$F_A = \iint q_{\tau_{u\alpha}}(u' - u_\alpha) p_{\tau_{v\alpha}}(v' - v_\alpha) \frac{e^{-jkr(u-u', v-v', w-w_\alpha)}}{r(u-u', v-v', w-w_\alpha)} du' dv' . \quad (3-21)$$

Similarly, combining (3-10), (3-11) and (3-19), Φ may be expressed as

$$\Phi = \frac{1}{j4\pi\omega\epsilon_0} \sum_{\alpha=1}^P I_\alpha (F_S^f - F_S^r) , \quad (3-22)$$

where

$$F_S^{f/r} = \frac{1}{\tau_{u\alpha}} \iint p_{\tau_{u\alpha}}\left(u' - u_\alpha \mp \frac{\tau_{u\alpha}}{2}\right) p_{\tau_{v\alpha}}(v' - v_\alpha) \frac{e^{-jkr(u-u', v-v', w-w_\alpha)}}{r(u-u', v-v', w-w_\alpha)} du' dv' \quad (3-23)$$

The preceding integrations are over all space. The F_S^f term corresponds to the falling half of the full rooftop, and the F_S^r term corresponds to the rising half. The pulse function along the u direction and the division by $\tau_{u\alpha}$ arise because of the divergence operation in (3-19) on the triangle function in (3-11). For a half-rooftop, only one of the F_S^f, F_S^r terms appears in (3-22). For a full rooftop, the presence of both F_S^f and F_S^r represents a charge doublet. As discussed earlier, $q_A(u)$ is defined differently for full and half-rooftop functions. Combining (3-15), (3-20) and (3-22) we find that

$$\mathbf{E}^{scat} = -\frac{1}{4\pi} \sum_{\alpha=1}^P I_\alpha \left[j\omega\mu_0 F_A \mathbf{e}_{u\alpha} + \frac{1}{j\omega\epsilon_0} \nabla (F_S^f - F_S^r) \right] . \quad (3-24)$$

In evaluating F_A [m] and F_S (here and in the following, F_S will serve as an abbreviation for $F_S^{f/r}$), a combination of Taylor series expansions and point-source approximation was used in [62]. The procedure approximates the integrands of (3-21) and

(3-23) by respecting only one real and one imaginary terms of the Taylor series; furthermore, yet another approximation is introduced, in the calculation of the real term. Consequently, the algorithm in [62] is of questionable accuracy, and the results depend on what is commonly referred to as *numerical tuning*; i.e., the solution converges — if at all — to largely different values depending on the individual choice of numerical parameters arrived at by trial and error. Therefore, this procedure is replaced here with an *exact* numerical technique for the calculation of integrals of (3-21) and (3-23). As a result, the algorithm, to be described in the next section, makes the method of the thin-wall model systematic.

The electric field boundary condition (3-4) is then applied; it is only here that distinction is made, through the choice of appropriate R_s , between conduction and polarization currents. Line function testing of the electric field yields a matrix equation of the form

$$\mathbf{ZI} = \mathbf{V} . \quad (3-25)$$

For a current representation involving P currents, \mathbf{Z} [Ωm] is an impedance matrix of order P , \mathbf{I} [A/m] is a current column vector of length P , and \mathbf{V} [V] is a column vector of length P that is obtained from the incident field. The matrix element in row β and column α is

$$Z_{\beta\alpha} = \int_{u_{1\beta}}^{u_{2\beta}} \left[\mathbf{E}^{scat}(x, y, z) / I_{\alpha} - \frac{\tau_{v\alpha}}{2(\tau_{v\alpha} + \tau_{w\alpha})} R_{s\alpha} R'_{\alpha}(x, y, z) \mathbf{e}_{u\alpha} \right] \cdot \mathbf{e}_{u\beta} du , \quad (3-26)$$

and the elements of \mathbf{V} are given by

$$V_{\beta} = - \int_{u_{1\beta}}^{u_{2\beta}} \mathbf{E}^{inc}(x, y, z) \cdot \mathbf{e}_{u\beta} du , \quad (3-27)$$

and

$$R'_\alpha(x, y, z) = \begin{cases} q\tau_{u\alpha}(u-u_\alpha)p_{v\alpha}(v-v_\alpha) & w = w_\alpha \\ 0 & w \neq w_\alpha \end{cases}, \quad (3-28)$$

$u_{1\beta}$ and $u_{2\beta}$ are given by (3-14), and (3-26) is evaluated at $v = v_\beta$ and $w = w_\beta$. The factor $R_{s\alpha}$, depending on the orientation of rooftop α , is either R_{sx} , R_{sy} or R_{sz} .

The current coefficient I_α is associated with one particular full rooftop. Each of the two half-rooftops that form the full rooftop is positioned on only one of the four sidewalls that correspond to the surface current whose density is \mathbf{J}_s and that is spread across the perimeter $2(\tau_{v\alpha} + \tau_{w\alpha})$. Of the surface current that flows across the perimeter, only the $\tau_{v\alpha}/2(\tau_{v\alpha} + \tau_{w\alpha})$ part belongs to the half-rooftop linked to the current coefficient I_α (see Figure 5).

The factor $R'_\alpha(x, y, z)$, which is not quite the same as $R_\alpha(x, y, z)$, is required in (3-26) because we have employed in (3-10) the volume current density \mathbf{J} and not the sheet (surface) current density \mathbf{J}_s as found in (3-4). Translating the language of mathematics, in the calculation of individual $Z_{\beta\alpha}$'s, the voltage drop on the surface imped-

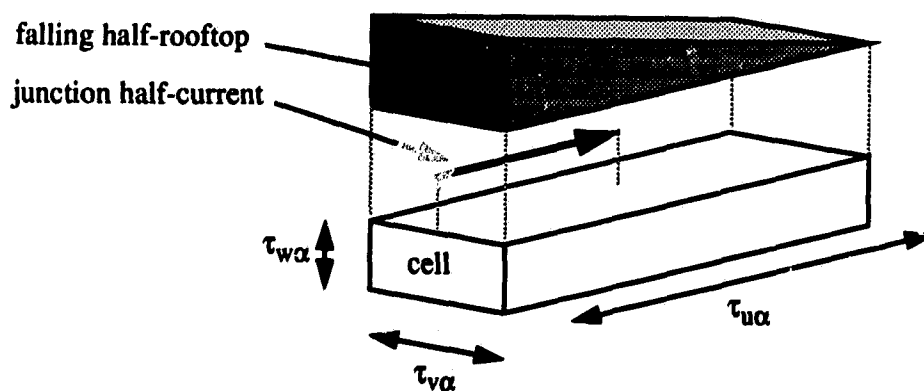


Figure 5. Falling half-rooftop and junction half-current associated with the current coefficient I_α .

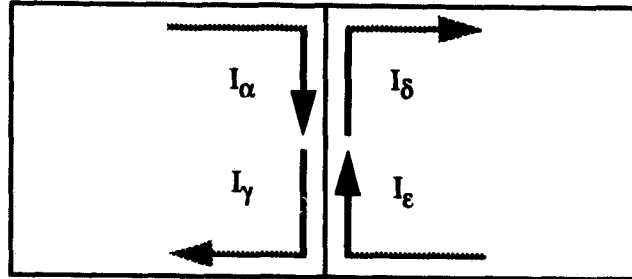


Figure 6. Two adjacent cells, with currents at the common sidewall, the interface, standing out prominently.

ance R_s is subtracted only for those integration paths that are positioned in the source currents' sidewall — this is illustrated in Figure 6, where for the falling half-rooftop of I_α as the source, in the calculation of individual $Z_{\beta\alpha}$'s, the voltage drop on the surface impedance is subtracted only for $\beta=\alpha$, $\beta=\gamma$, $\beta=\delta$ and $\beta=\epsilon$.

A full rooftop has two components — a falling and a rising half-rooftops — directed along two different coordinates of the Cartesian system. Therefore, evaluation of all $Z_{\beta\alpha}$'s, as prescribed by (3-26), generally takes two steps: one accounting for the falling the other for the rising half-rooftop of the source current I_α (in other words, each corner function is treated as if it consisted of two independent half-rooftops). Only for some mutual impedances, the two-step operation is reduced to a single-step one; this occurs when the source current I_α has only one component parallel with the current of the target element, upon which the voltage V_β is calculated. One of the consequences of the fact that all possible variations of source and target full rooftops form *at least* one pair of parallel current components is that the resulting impedance matrix is dense; moreover, the matrix does not contain a single zero element.

For the integration of (3-26), the Gauss-Legendre quadrature is employed. Though an integration operation is indicated along the u direction in (3-26), because of the

gradient operation in (3-15), the Φ component is not actually integrated but merely evaluated at the end points of the integration path.

For scattering problems, \mathbf{E}^{inc} will be that associated with a plane wave, so that \mathbf{V} becomes an array of complex constants. The current density is found from (3-25) using standard Gaussian elimination or matrix inversion through the singular value decomposition [113]. Once the current coefficients I_α have been found, the near- or far-field electric field may be calculated using (3-24).

For a source-driven radiation problem, an impulse electric field is impressed across an infinitesimal gap (delta gap) located within the conductor region associated with the source. Appropriate elements in the voltage column vector, corresponding to rooftops that overlap and are aligned with the source region, are set to unity, as is conventionally done in moment methods involving wire antennas [101]. Care must be taken to ensure that none of these elements are inadvertently zeroed, as this will cause the delta-gap source to be shorted out. If line-integral testing is employed, then the source location can only be specified to within half a subsection, since an impressed-impulse electric field will produce the same effect no matter where on a particular line interval it appears.

3.6 Calculation of F_A and F_S

The factors F_A and F_S must be calculated with care. At low frequencies, the electric field is so dominated by the scalar potential that the contributions to the electric field from the vector potential may be lost [114]. The scalar potential, unfortunately, does not in general contain enough information to determine the current density. Even at higher frequencies and especially if the basis functions are defined over patches that have a high aspect ratio, the matrix elements corresponding to the self- and adjacent (side-by-side) elements may

have nearly equal values. Even a slight error in the calculation of the scalar potential, if the error is comparable to the vector potential contribution, could cause large variations in the results. We have observed that if quadrature integration procedures or the Taylor series expansion combined with point-source approximations employed in [62] are used to evaluate F_A and F_S , such problems do arise and manifest themselves in many ways, including incorrect current flows and input impedances with negative real parts. Mautz and Harrington [114] circumvent the low-frequency problem, though in a rather involved fashion, by using two sets of basis functions. We have avoided such problems, as well as the effective quasi-tuning resulting from the procedure of Rubin and Daijavad [62], by devising an exact algorithm for the calculation of F_A and F_S . In the remainder of this section, the Rubin and Daijavad algorithm and our exact integration technique are described and discussed, and our technique is proven to perform better.

Accurate calculation of the generalized exponential integral is of paramount importance for the method-of-moments solutions of problems involving radiating structures. Inaccuracies of the numerical evaluation of self- and mutual impedances can lead to grossly incorrect current distributions. In addition, varying the degree of inaccuracy of the numerically integrated elements of the impedance matrix is equivalent to tuning the results, which in effect means inability to predict unknown values.

The generalized exponential integral has found a host of applications in electromagnetic theory. Among the best known examples of the utilization of the integral in its one-dimensional form is the calculation of mutual and self-impedances of wire-antenna elements, which is necessary for obtaining current distributions on these radiators. The problem of the calculation of self-impedance of a wire element of length $2x$ and radius a is — from the numerical point of view — reduced to the evaluation of the integral

$$I_1 = \int_{-x}^x \frac{e^{-jk\sqrt{x'^2+a^2}}}{\sqrt{x'^2+a^2}} dx' \quad (3-29)$$

The presence of radius a in the expression reflects sampling the electric field just above the surface of the wire, which is in direct correspondence with physical reality; evaluation of the integral on the axis of the wire (or filaments parallel with the axis and contained in the wire) is neither needed nor desirable. Despite the fact that an infinitesimally thin wire ($a=0$) is not of practical importance, it should not be left unnoticed that integral I_1 in (3-29) does not exist for $a=0$.

A multitude of techniques for the evaluation of I_1 can be found in the literature, and we will mention here only a few representative ones. In [115], the one-dimensional exponential integral is expressed in terms of three integrals, where the first is available in closed form, while the remaining two are given by tabulated generalized sine and cosine integrals. Among the options suggested in [101] is the expansion of I_1 into a Maclaurin series and an approximation that accounts for only the first real and first imaginary terms. Several exact methods for the calculation of the one-dimensional generalized exponential integral for wires of arbitrary nonzero radii were found recently. Of particular significance is the technique announced in [116]. This algorithm is based on an exact series representation that converges rapidly in the induction and near-field regions of an antenna. It is demonstrated that the algorithm is stable for a wire-radius-to-wavelength ratio as small as 10^{-19} [116].

Planar radiators, by analogy, require evaluation of the double integral

$$I_2 = \int_{x_1 < 0}^{x_2 > 0} \int_{y_1 < 0}^{y_2 > 0} \frac{e^{-jk\sqrt{x'^2+y'^2+a^2}}}{\sqrt{x'^2+y'^2+a^2}} dy' dx' \quad (3-30)$$

which corresponds to the usage of pulses in the role of subsectional expansion functions in

the method-of-moments formulation. If different expansion functions are desired, the integrand of I_2 needs to be properly modulated and the limits of integration may change, where the origin $(x',y')=(0,0)$ may be located inside, or on the boundary, of the integration region. As a matter of fact, evaluation of F_A in (3-21) is reduced to the evaluation of

$$I_3 = \int_0^{x_2} \int_{-y_2}^{y_2} \left(1 - \frac{x'}{x_2}\right) \frac{e^{-jk\sqrt{x'^2+y'^2+a^2}}}{\sqrt{x'^2+y'^2+a^2}} dy' dx' . \quad (3-31)$$

It should be pointed out that while the case of $a=0$ is of merely academic importance in one-dimensional wire-antenna applications, it has a perfectly valid physical equivalent for two-dimensional planar radiator configurations — it corresponds to integrating the electric field on the surface of a radiating element.

Integrals of the types of I_2 and I_3 have been evaluated by techniques that — although different in approach to the problem — have one feature in common: they fail to integrate the singularity that emerges at $a=0$ and $(x',y')=(0,0)$. When evaluating I_2 through the forthcoming slice-and-dice scheme, the singularity cannot be rigorously integrated over. The approach that has become standard in antenna engineering is to evaluate the integral for a small, non-zero value of a instead, which in effect introduces an offset in the third coordinate of the Cartesian system. However, there is no physical justification for the introduction of any offset, as the integration is supposed to stand for sampling the electric field intensity in the infinitesimally small elevation above the target-element surface. Introducing the non-zero offset, however small, does not correspond to physical reality; furthermore, it — artificially and unnecessarily — adds to the system an unknown variable, which somehow has to be determined.

As we reported in [117], proper determination of the non-zero a , where $a=0$ is actually required, assuming one still can use the word “proper” in this context, has almost become a discipline in itself, thus rendering a software package “more” or “less” efficient.

Without contributing to the discussion, one can safely conclude that the determination of the offset, customarily called tuning, requires skills and extra computation, which both are time consuming. One way of determining the offset is to observe the effects of varying a on the radiation pattern and, through stability analysis and experience, find the usually small range of a where the radiating structure behaves as expected. This approach, however, is not reliable, for the calculation of a radiation pattern involves a double integration, which smoothens the pattern, even if the utilized current distribution is not very accurate. A better technique to determine the offset is to follow how the changing non-zero a affects the input impedance of the structure, namely its real part. As a varies, typically there is a range where the real part of the input impedance is positive and stable; the most rational choice to make is to select the value of a that corresponds to the center of that range.

Besides the inability to evaluate the integrals of the types of I_2 (3-30) and I_3 (3-31) for $a=0$, all previous techniques — in addition — very often implement various convenient approximations that reduce numerical complexity at the cost of introducing more inaccuracy and limit the application range of the algorithm, often making it custom-made for one particular class of problems or application. For illustration, the Rubin-Daijavad technique [62] evaluates I_3 through the common expansion of the complex exponential into a Maclaurin series — respecting only one real and one imaginary terms. This is followed by a term-by-term integration, where two of the three resulting integrals are presented in a closed form, and the computation of the remaining integral is transformed to the evaluation of logarithmic functions at the centers of four auxiliary integration regions. The four-auxiliary-regions approach, while advantageous with respect to reducing CPU-time requirements, is implicitly inaccurate, resulting in the introduction of an approximation into the already introduced approximation of the one real and one imaginary terms of the Maclaurin expansion; eventually, this manifests itself in over-the-scale dependence of the current distribution (obtained through inversion of the calculated impedance matrix) on N_1, N_2, N_3 , the numbers of cells in each direction — this in effect is

nothing else than just a somewhat less obvious form of tuning, *quasi-tuning*. Additionally, the technique leads to the evaluation of the natural logarithm at zero in the real part of I_3 if $a=0$. Consequently, the real part of I_3 is finite only if a differs from zero, and is singular otherwise. Moreover, the four-auxiliary-regions approach is based on the symmetrical nature of the third integral, making the approach inapplicable for the cases where the lower limit for the integration over x in I_3 is required to be different from zero.

In the following it will be shown that there is absolutely no need for introducing and tuning an offset, since the singularity of the *two-dimensional generalized exponential integral*, i.e., integrals of the types of I_2 and I_3 , that arises with $a=0$ is integrable; that the integral is finite, thus does exist, and can be exactly calculated. Furthermore, we present algorithms that evaluate I_2 and I_3 without any need for time-consuming computing, and we demonstrate the stability of the algorithms.

The general configuration for integrals of the type of I_2 is depicted in Figure 7. Instead of performing integration in the Cartesian coordinate system, we evaluate I_2 in polar coordinates, resulting in

$$I_2 = \int_0^{2\pi} \int_0^{\rho_c(\theta)} \frac{e^{-jk\sqrt{\rho^2+a^2}}}{\sqrt{\rho^2+a^2}} \rho d\rho d\theta, \quad (3-32)$$

where $\rho = \sqrt{x^2+y^2}$ and $\rho_c(\theta)$ is the radial distance from the origin of the coordinate system to the contour of the integration region (Figure 7). It is obvious that the technique is directly applicable also to the cases where the origin of the coordinate system is located outside of the integration region — in these cases the lower integration limit over ρ would be some positive value $\rho_{cl}(\theta)$ instead of zero. After the change of variables

$$u = \sqrt{\rho^2+a^2} \quad (3-33)$$

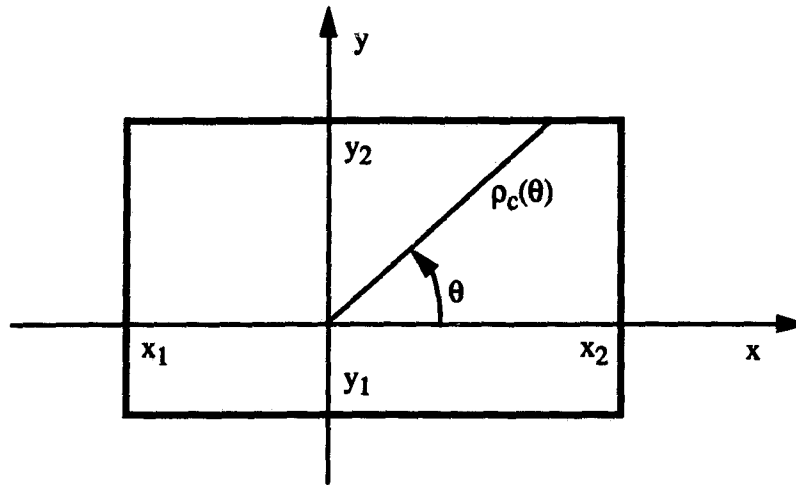


Figure 7. Rectangular integration region in the Cartesian coordinate system, with some additional notation.

we get:

$$I_2 = \frac{j}{k} \int_0^{2\pi} \left(e^{-jk\sqrt{\rho_c(\theta)^2 + a^2}} - e^{-jk|a|} \right) d\theta. \quad (3-34)$$

Clearly, the singularity, which arises at $a=0$ in Cartesian coordinates (c.f. (3-30)), has been removed, and the integral poses no numerical difficulties. Note that (3-34) is independent of the shape of the contour describing the boundary of the integration region. For the rectangular contour of Figure 7, $\rho_c(\theta) = x_2/(\cos\theta)$ for the right vertical line, $\rho_c(\theta) = y_2/(\sin\theta)$ for the upper horizontal line, $\rho_c(\theta) = x_1/(\cos\theta)$ for the left vertical line, and $\rho_c(\theta) = y_1/(\sin\theta)$ for the lower horizontal line.

In order to evaluate I_3 , beside I_2 , it is necessary to calculate the following integral:

$$I_4 = \int_0^{x_2} \int_{-y_2}^{y_2} x' \frac{e^{-jk\sqrt{x'^2 + y'^2 + a^2}}}{\sqrt{x'^2 + y'^2 + a^2}} dy' dx' = \int_0^{2\pi} \int_0^{\rho_c(\theta)} \rho^2 \frac{e^{-jk\sqrt{\rho^2 + a^2}}}{\sqrt{\rho^2 + a^2}} d\rho \cos\theta d\theta. \quad (3-35)$$

We calculate the integral over ρ by parts

$$\int_0^{\rho_c(\theta)} \rho^2 \frac{e^{-jk\sqrt{\rho^2+a^2}}}{\sqrt{\rho^2+a^2}} d\rho = \frac{j}{k} \rho_c(\theta) e^{-jk\sqrt{\rho_c(\theta)^2+a^2}} - \frac{j}{k} \int_0^{\rho_c(\theta)} e^{-jk\sqrt{\rho^2+a^2}} d\rho, \quad (3-36)$$

resulting in the following expression for I_3 :

$$I_3 = I_2 - \frac{j}{kx_2} \int_0^{2\pi} \left[\rho_c(\theta) e^{-jk\sqrt{\rho_c(\theta)^2+a^2}} - \int_0^{\rho_c(\theta)} e^{-jk\sqrt{\rho^2+a^2}} d\rho \right] \cos\theta d\theta. \quad (3-37)$$

Once again, the singularity is no longer present.

Of course, the numerical integration over θ , although involved in both components of I_3 , does not have to be performed in two separate cycles. This integration, for two different integrands (where the second integrand requires also integration over ρ), can be executed in a single cycle; as a result of that, our software implementation of I_3 requires only two loops, one submerged in the other.

The following demonstrates the performance of our integration procedure. Figures 8 show plots of the real and imaginary parts of integral I_3 versus a . Calculations produced by three different algorithms are presented: 1. the technique suggested by Rubin and Daijavad in [62] (dash-dotted lines); 2. two-dimensional Gaussian integration in Cartesian coordinates (dashed lines); 3. the technique described in this section, i.e., exact two-dimensional integration in polar coordinates, using the Gauss quadrature (solid lines). The Gaussian-integration results in polar coordinates (technique 3) were obtained by integrating in only 3 points in the inner integral and 6 points in the outer integral (c.f. (3-37)), for each particular value of a . However, those in Cartesian coordinates (technique 2) were calculated with 6 points in the inner and 3 points in the outer integral (c.f. (3-31)). This reversal of the number of points for inner and outer integrations in Cartesian coordinates produces more accurate results, because a higher number of points in the inner integral

smoothes the integrand of the outer integral. Each curve in Figures 8 contains 2001 points and took 1.4 seconds of CPU time of an IBM RS/6000 530 machine.

Before evaluating the results of Figures 8, some remarks about the presentation of values at $a=0$ are in order. The solid line is calculated exactly at $a=0$, as no singularity exists in (3-37). Also the dashed line is calculated at $a=0$, but the numerical integration carefully avoids the sampling point $(x',y')=(0,0)$, for which the integration in Cartesian coordinates (3-31) fails to produce a finite value. The dash-dotted line starts at $a=10\mu\text{m}$, since the method implemented in [62] renders the integrand singular at $a=0$.

Obviously, the method suggested in [62] produces some considerable differences in the real part of I_3 — in this example up to 50 percent (dash-dotted line in Figure 8a) — with respect to our technique (solid line). As expected, the results of the Gaussian integration in Cartesian coordinates (dashed line) converge to those in polar coordinates (solid line) as a increases. Better convergence for smaller a can be achieved by significantly increasing the number of integration points in (3-31). This is demonstrated in the inset of Figure 8a, using 96x96 integration points in Cartesian coordinates. However, the CPU time increases from the aforementioned 1.4 seconds to 199.2 seconds, which clearly makes a further increase of precision in Cartesian coordinates unreasonable. On the other hand, the new technique using integration in polar coordinates (3-37) is stable with respect to an increase in the number of integration points. The maximum difference between the (6,3)- and (96,96)-point integrations in polar coordinates occurs at $a=0$ and is 0.1 percent, thus falls within the plotting accuracy of the solid line in the inset of Figure 8a.

Figure 8b shows the results of the imaginary part of I_3 . Computations using integration in both Cartesian and polar coordinates are in excellent agreement even for small values of a . Again, the values produced by the method suggested in [62] (dash-dotted line) differ considerably from those of the other two techniques. Moreover, the imaginary part is independent of a , because only one imaginary term, $-jk$, of the Maclaurin series of the integrand is respected in [62].

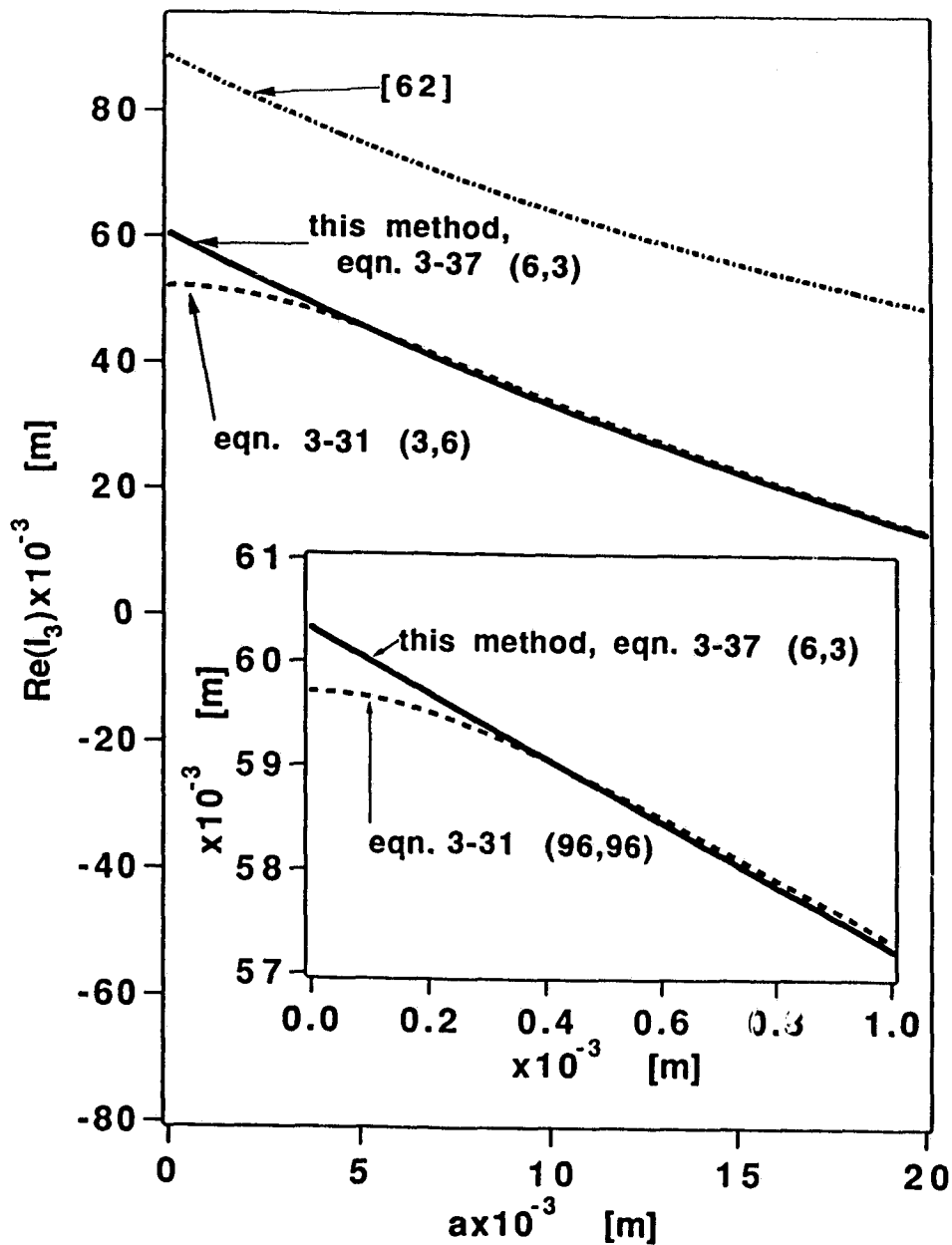


Figure 8a. Calculated real part of integral I_3 versus a . (Parameters: $x_1=0$, $x_2=5\text{cm}$, $y_1=-3\text{cm}$, $y_2=3\text{cm}$, frequency = 2GHz.) Solid line: 6-outer/3-inner-point Gaussian integration in polar coordinates according to (3-37); dashed line: 3-outer/6-inner-point Gaussian integration in Cartesian coordinates according to (3-31); dash-dotted line: tech-

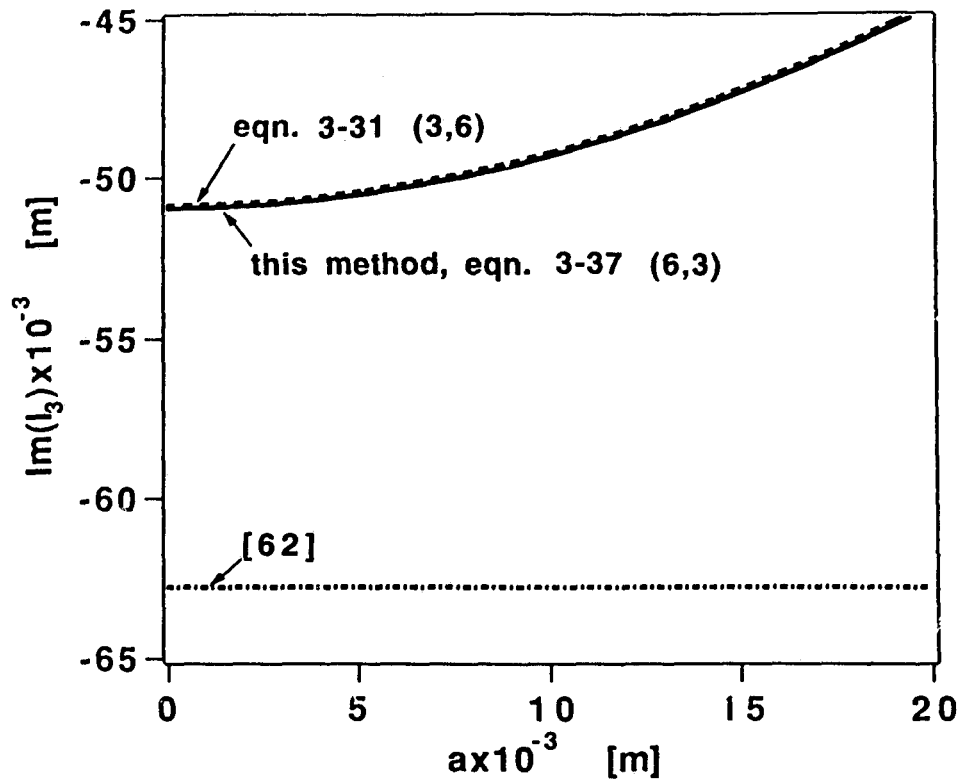


Figure 8b. *Calculated imaginary part of integral I_3 versus a . (Parameters: $x_1=0$, $x_2=5\text{cm}$, $y_1=-3\text{cm}$, $y_2=3\text{cm}$, frequency = 2GHz.) Solid line: 6-outer/3-inner-point Gaussian integration in polar coordinates according to (3-37); dashed line: 3-outer/6-inner-point Gaussian integration in Cartesian coordinates according to (3-31); dash-dotted line: technique suggested in [62]. (Note that the values of the dash-dotted line labeled [62] are independent of a , because only one imaginary term, $-jk$, of the Maclaurin series of the integrand is respected in [62].)*

Figure 8a (cont'd): *nique suggested in [62]. Inset: solid line: 6-outer/3-inner-point Gaussian integration in polar coordinates according to (3-37); dashed line: 96-outer/96-inner-point Gaussian integration in Cartesian coordinates according to (3-31).*

Figures 8 prove all three techniques are stable, but their accuracies are very different. Integrating the complete integrand — in either polar or Cartesian coordinates — proves I_3 is *finite* and can be calculated exactly, even at $a=0$. The convergence analysis of the Gaussian integration proves that our technique is superior to the integration in Cartesian coordinates. We have stressed out the precision of integration at $a=0$ and at small a 's, because these are the situations that are involved in the evaluation of self- and mutual impedances, respectively, of planar-radiator elements. Varying the degree of inaccuracy in the evaluation of the impedance elements results in a wide range of possible but inaccurate current distributions.

3.7 Time Reduction Strategy

Rubin and Daijavad [62] suggested a time reduction algorithm for the calculation of F_A and F_S . The algorithm is based on the following rationale. When setting up the impedance matrix, each full rooftop is calculated as if it consisted of two independent half-rooftops. If the rectangle associated with the source half-rooftop is within a small fraction of a wavelength from the test region (the line path defined in section 3.5 and depicted in Figure 3), i.e., if the target element cannot be classified as positioned in the far zone of the source element, then numerical integration is used to calculate F_A and F_S . If the distance from the center of the rectangle to the test region is more than several times the largest dimension of the rectangle, then the integrals are calculated using the point-source approximation. If neither of the two is true, i.e., if the target element is positioned in the intermediate region between the near and far zones of the source element, the source rectangle is subdivided. For each rectangular subdivision, as for the original rectangle and depending upon certain criteria, numerical integration (a Taylor series expansion) or point-source approximation is

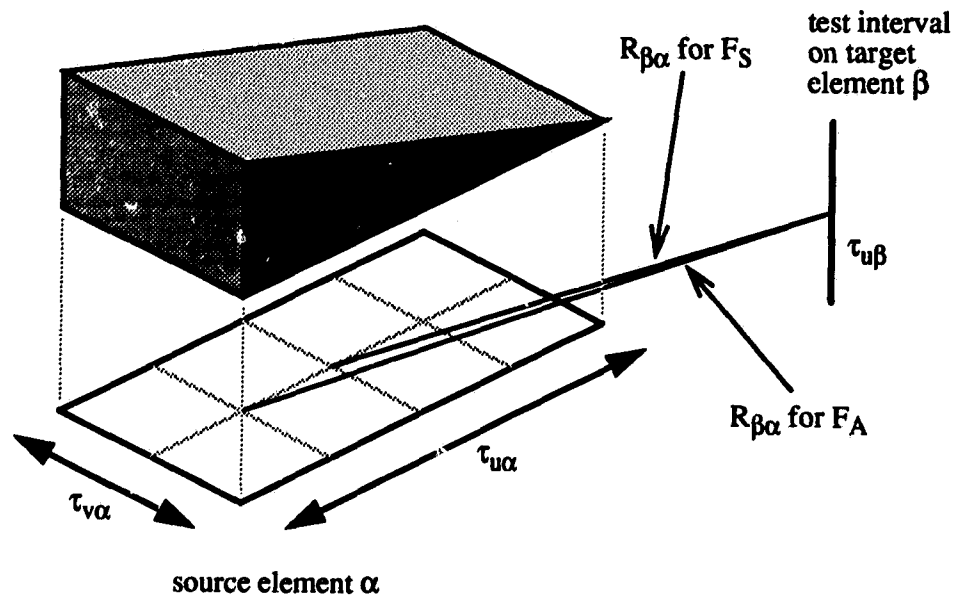


Figure 9. Subdivided source region of the source current I_α and test interval of the target element upon which the voltage V_β is calculated.

employed. The individual contributions are then summed up. The procedure always involves a Taylor series expansion for the calculation of the self terms (self-impedances). For the point-source approximation of F_S , all the charge is lumped at the center of the source patch and the electric field is calculated along the test interval. For the point-source approximation of F_A , all the current is lumped at a point $\tau_{u\alpha}/4$ from the center of the source element, as illustrated in Figure 9.

Algorithm A:

Step 1. Consider each source-element half-rooftop and target-element test interval individually (Figure 9). The rectangular region over which the source half-rooftop is non-zero is labeled source element α ; the line interval on the target element over which the electric field is integrated is labeled test interval β .

Step 2. Calculate the distance between the centers of the source element α and test interval β — this distance, to be referred to as $r_{\beta\alpha}$, is identical with the distance $R_{\beta\alpha}$ for the point-source approximation of F_S (Figure 9).

Step 3. If $r_{\beta\alpha} + \Delta_1 \leq \text{lim}_1$, where Δ_1 and lim_1 are parameters to be selected, then calculate the integral using the Taylor series expansion and stop.

Step 4. If $r_{\beta\alpha} - \Delta_2 \leq \text{lim}_2$, where Δ_2 and lim_2 are parameters to be selected, then calculate the integral using the point-source approximation and stop.

Step 5. If neither of the conditions in Step 3 or Step 4 is satisfied, divide the source element into subelements. Divide the longer dimension into N_l sections and the shorter dimension into N_w sections, where N_w is the smallest integer that satisfies $N_w \geq N_l \cdot \min(\tau_{u\alpha}, \tau_{v\alpha}) / \max(\tau_{u\alpha}, \tau_{v\alpha})$.

Step 6. For each subelement defined, appropriately reorder the indices α and find the distance between subelement α and test interval β .

Step 7. If $r_{\beta\alpha} \leq \text{lim}_1$, calculate the contribution from subelement α using the Taylor series expansion.

Step 8. If $r_{\beta\alpha} > \text{lim}_1$, calculate the contribution from subelement α using the point-source approximation.

Step 9. Accumulate the contributions from Steps 7 and 8 and repeat these steps until all contributions from $N_l N_w$ subelements are accounted for.

In the algorithm, lim_1 is the distance that in [62] has been chosen to be $0.3 / (k\sqrt{\epsilon'_r})$, where ϵ'_r is the largest relative dielectric constant in the structure. The idea is that if kr is reasonably small, $\exp(-jkr)/r$ may be replaced by a two-term Taylor series expansion with only a small error introduced. At frequencies where the entire structure is only a small fraction of the wavelength, each matrix element is calculated exclusively through the Taylor expansion. The value of lim_1 in the context of the two-term Taylor series expansion for small r

$$\frac{e^{-jkr}}{r} = \frac{\cos(kr)}{r} - j\frac{\sin(kr)}{r} \approx \frac{1}{r} - jk \quad (3-38)$$

essentially means acceptance of a 4.5-percent error in the calculation of the real part and a 1.5-percent error in the calculation of the imaginary part, as (3-38) assumes both $\cos(0.3)=0.955$ and $\sin(0.3)/0.3=0.985$ to be unity. The factor involving ϵ'_r is believed necessary to insure accuracy for structures composed of high dielectric-constant materials. The parameter Δ_1 was employed to reduce the complexity of the calculations in Step 3; the distance $r_{\beta\alpha}$ should actually be the maximum distance between any point of the source element and any point of the test interval. By using a parameter that is a simple function of $\tau_{u\alpha}$, $\tau_{v\alpha}$ and $\tau_{u\beta}$, this can be accomplished, albeit approximately, with minimal computational effort. In [62], $\Delta_1=\max(\tau_{u\alpha},\tau_{v\alpha})+0.5\tau_{u\beta}$ was used. In Step 4, \lim_2 is a distance that is related to the dimensions of the source patch, which was chosen to be $4.1 \max(\tau_{u\alpha},\tau_{v\alpha})$ in [62]. The factor Δ_2 serves a purpose similar to Δ_1 ; Rubin and Daijavad [62] set $\Delta_2=\Delta_1$ and use $N_f=7$.

The above values of \lim_1 , \lim_2 , Δ_1 , Δ_2 and N_f , based on physical reasoning and comparison with the literature, represent a set of values that the authors of [62] report to work well with their model. The algorithm is said to appear quite stable; the authors varied the five parameters, though not systematically, and have found the results vary only minimally. The authors of [62] also warn that any choice of parameters represents a trade-off between accuracy and run time; the parameters that give optimal results, however, may be problem dependent and at the minimum would require exhaustive reruns on many different structures.

We have applied our exact integration technique to the time reduction algorithm described above. While we can confirm values of \lim_2 , Δ_1 and Δ_2 as fitting, we have found the value of \lim_1 , as suggested by Rubin and Daijavad, highly controversial, to say the least. The problem is that at low frequencies — more precisely, at frequencies

whose wavelengths are large in comparison with physical dimensions of the structure under analysis (e.g., the example to be presented in Section 4) — $\lim_1 = 0.3 / (k\sqrt{\epsilon'})$ comes out *much larger* than \lim_2 . Physically, it would require to subdivide the source elements that are *close* to the target element and for each of the subelements test individually whether the subelement's contribution is to be calculated as accurately as possible (via numerical integration) or approximately (through the point-source approximation), while the accurate procedure would be applied to *distant* target elements. Clearly, this does not make much sense. We have found it more appropriate to set $\lim_1 = \lim_2$ instead. Also, our exact integration technique allows to reduce the suggested value of N_I to 3.

Algorithm A does reduce the CPU time necessary to set up the impedance matrix of a structure. Nevertheless, the price to pay — as will be shown in Section 4 — is a certain, albeit small, deterioration in precision. As a rule, however, the deterioration pronounces itself to a higher degree when the order of the impedance matrix increases. With the primary goal not to sacrifice precision, yet still reduce requirements for computational resources whenever possible, we have developed an alternative time reduction algorithm — Algorithm B, to be described later in this section — which we prefer to Algorithm A.

The algorithm is based on the following rationale: Clearly, numerical evaluation of F_A and F_S , which are defined by (3-21) and (3-23), is the most important factor dictating the amount of CPU time necessary for setting up the impedance matrix \mathbf{Z} . Any reduction in processor time needed for the evaluation of F_A and F_S will lower overall requirements for computer resources. Now, let us define an auxiliary variable T as

$$T = \frac{e^{-jk\sqrt{[(x_1+x_2)/2]^2 + [(y_1+y_2)/2]^2 + a^2}}}{\sqrt{[(x_1+x_2)/2]^2 + [(y_1+y_2)/2]^2 + a^2}}, \quad (3-39)$$

where x_1, x_2, y_1 and y_2 are the same physical quantities as in (3-30). With this notation, integral I_2 , defined by (3-30), can be expressed as

$$I_2 = T \cdot (x_2 - x_1) (y_2 - y_1) + \int_{x_1 < 0}^{x_2 > 0} \int_{y_1 < 0}^{y_2 > 0} \left(\frac{e^{-jk\sqrt{x'^2 + y'^2 + a^2}}}{\sqrt{x'^2 + y'^2 + a^2}} - T \right) dy' dx' . \quad (3-40)$$

Similarly, integral I_3 , defined by (3-31), can be written as

$$I_3 = 0.5T \cdot x_2 \cdot 2y_2 + \int_0^{x_2} \int_{-y_2}^{y_2} \left[\left(1 - \frac{x'}{x_2} \right) \frac{e^{-jk\sqrt{x'^2 + y'^2 + a^2}}}{\sqrt{x'^2 + y'^2 + a^2}} - 0.5T \right] dy' dx' . \quad (3-41)$$

While — in comparison with (3-31) — there are extra additive and subtractive operations in (3-41), the integrand of (3-41), in general, is a smoother function than the integrand of (3-31), even more so for large values of $\sqrt{x'^2 + y'^2 + a^2}$ in the integrand. As a result, the double integration of (3-41) requires evaluation of its integrand in fewer integration points than the integration of (3-31), with virtually no sacrifice in precision.

With this in mind, we now define the alternative algorithm, replacing Steps 3 to 9 of Algorithm A:

Algorithm B:

Step 1. Consider each source-element half-rooftop and target-element test interval individually (Figure 9). The rectangular region over which the source half-rooftop is non-zero is labeled source element α ; the line interval on the target element over which the electric field is integrated is labeled test interval β .

Step 2. Calculate the distance between the centers of the source element α and test interval β — this distance, to be referred to as $r_{\beta\alpha}$, is identical with the distance $R_{\beta\alpha}$ for the point-source approximation of F_S (Figure 9).

Step 3. If $r_{\beta\alpha} + \Delta_1 \leq \text{lim}_2$, where Δ_1 and lim_2 are parameters specified earlier, then calculate the integrals of F_A and F_S using the exact numerical integration, based on (3-31), and stop.

Step 4. If the condition in Step 3 is not satisfied, calculate the integrals of F_A and F_S using the modified numerical integration, based on (3-41), and stop.

In conclusion of this section, a few words about values of N_1 , N_2 and N_3 . From the way the system of overlapping rooftop functions is defined in the model, it is obvious that the values of N_1 , N_2 and N_3 affect the degree of resemblance between the calculated current distribution on a given structure and the real current distribution, dictated by laws of physics — the finer the division of the structure, the more accurate the resulting current distribution. In the same breath, however, it is equally obvious that any increase of the N_1 , N_2 and N_3 values is accompanied by a number of shortcomings and limitations, most important of which are: 1.) the total number of corner functions (c.f. (3-7)) — i.e., the order of impedance matrix \mathbf{Z} — increases rapidly, which translates itself to a rapid growth of requirements on computer memory; 2.) as a direct consequence of the previous, demands on the overall processor time are sky-rocketing, not excluding the potential necessity of having to assign a dedicated workstation to the problem. Therefore, the task of an applications engineer is transformed to finding a compromise between desires of the highest achievable computational precision on one hand and limited resources on the other hand.

Our experience has shown that, as a general rule, at least sixteen cells per guided wavelength are needed in order to obtain a fairly accurate current distribution. This general requirement may fluctuate slightly from one structure to another: if the current on a structure has components directed predominantly along one axis of the coordinate system, the numbers of cells along the remaining two axes can be lowered accordingly. Once the values of N_1 , N_2 and N_3 are chosen, convergence analysis should be performed in order to

find out proper numbers of sampling points for the integrations prescribed by (3-31) and (3-41) — twenty-four and twelve sampling points, respectively, usually suffice. A fine division of the structure (i.e., high values of N_1 , N_2 and N_3) renders small integration regions (Figure 7), which in turn reduces the number of sampling points in the integrals of (3-31) and (3-41) for a desired precision. An overkill in the numbers of sampling points unnecessarily prolongs the computation; an underestimation, on the other hand, makes a chosen computational precision unachievable.

To summarize, there are two mutually coupled sets of variables to control: the numbers of cells along the axes of the coordinate system and the numbers of sampling points in the integrals of (3-31) and (3-41). Careful consideration in selecting the values is advisable.

4 POLARIZATION CHARGE IN A DIELECTRIC CUBE

The first application of the model described in Section 3 demonstrates the absence of fictitious charge in the solution within homogeneous dielectrics, a condition dictated by physical principles. Though the formulation contains no explicit constraints forcing the polarization charge to be zero, numerical simulations show that the charge density falls off rapidly with distance from dielectric interfaces.

A dielectric cube with a relative dielectric constant of 9 has one of its sidewalls illuminated by a plane wave — as illustrated in Figure 10 — having a frequency

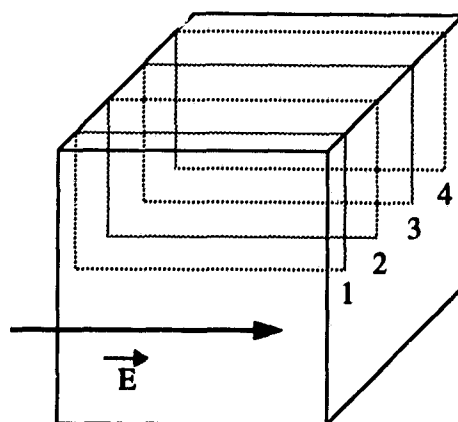


Figure 10. Dielectric cube of sidelength $A=0.2 \times 10^{-4} \lambda_0$ and relative permittivity $\epsilon_r=9$ illuminated by a 1V/cm plane-wave incident electric field. Layers 1—4 correspond to the locations of computed current distributions in Figures 11 and 12. For symmetry reasons, only one half cube volume is of interest.

such that each side of the cube is only 2×10^{-5} wavelength (more specifically, the frequency of the incident wave is 1.5 MHz and the cube edges measure 4 mm each). This is a recalculated example of [62]. We have employed our improved algorithm that calculates the involved integrals exactly. As in [62], the structure was segmented into the grid of $4 \times 4 \times 4$ cells, of which only the distributions on the upper half will be presented for symmetry reasons. Figure 11 presents the normalized net polarization currents on layer 1 of Figure 10 as reported in [62]. In comparison, Figure 12 shows the net polarization currents on layers 1—4 obtained through our integration technique and normalized to the “1000”-value net current of Figure 11. As a result of the long wavelength, the solution corresponds to that in a static electric field. From Figure 12 it is clearly seen that as the incident electric field penetrates the piece of dielectric, the induced polarization currents are attenuated, as one would expect. Also as expected, the symmetry of horizontally directed currents and the antisymmetry of vertically directed currents are perfectly preserved — up to 3 and 8 significant figures if Algorithms A (retrofitted with our exact inte-

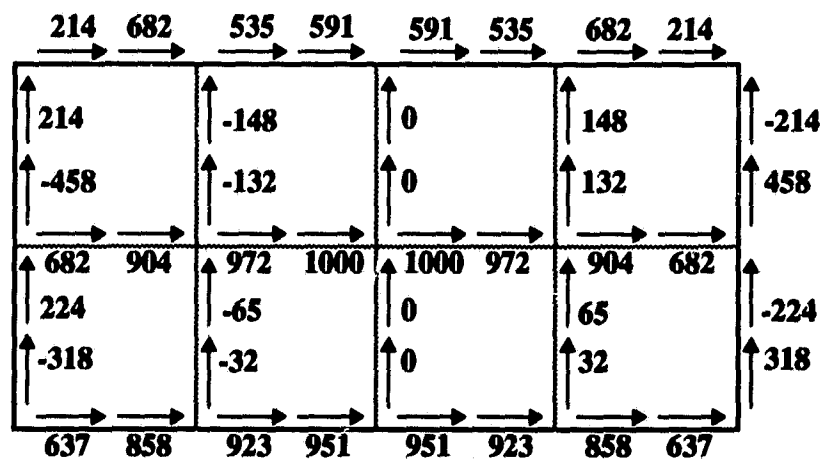
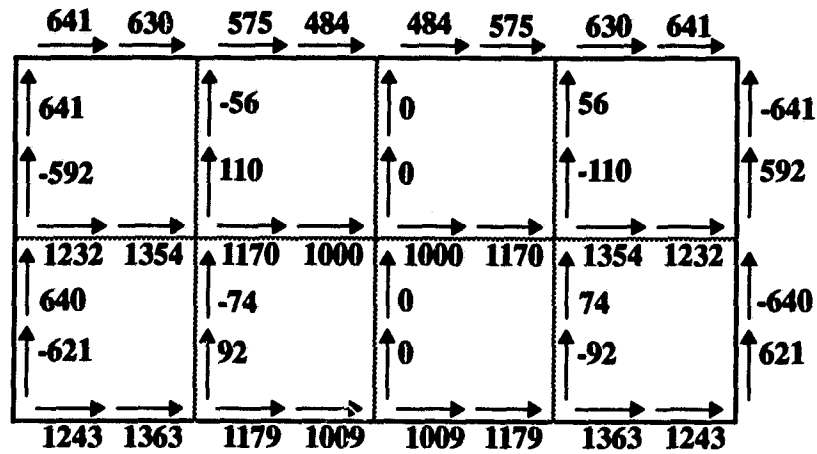
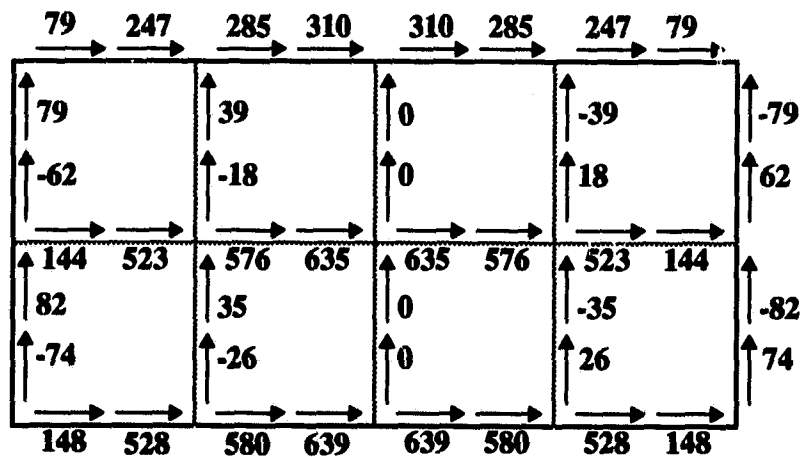


Figure 11. Polarization current distribution on layer 1 (cf. Figure 10) of the cube according to [62].

gration procedure) and B are implemented, respectively — through the entire structure. Similarly, the currents along the fictitious axes of symmetry in all four layers — though not explicitly forced to zero in the solution — come out zero in the entire structure, simply because of the antisymmetrical nature of charge distribution. Since our integration procedure is stable and straightforward, leaving the number of integration points as the only variable in the numerical process, convergence of the solution, as detailed in Section 3.6, is readily obtained. Therefore, the discrepancies between our results (Figure 12, layer one) and those of [62] (Figure 11) are attributed to the different — and rather arbitrary — integration process in [62]. Contrary to [62], our results are obtained without the need for point-source approximations. Even after artificially introducing such approximations, we have not been able to reproduce the results of Figure 11. Regrettably, we cannot compare our spatial current distributions in layers 2 to 4 with [62], as the respective results are not shown in that reference.

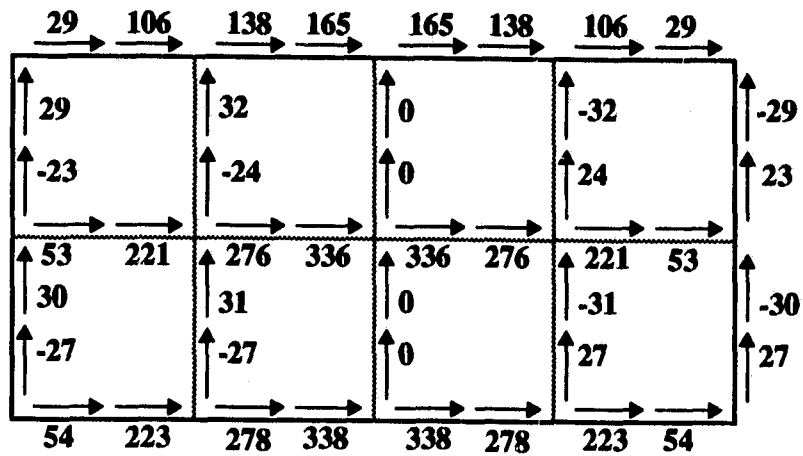


Layer 1

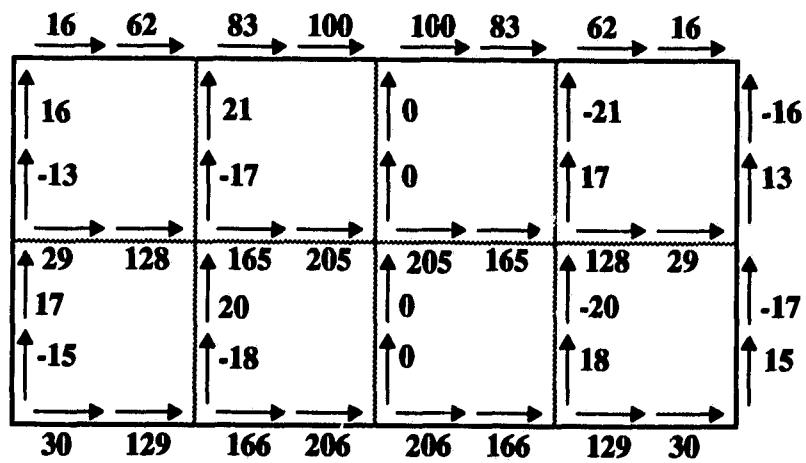


Layer 2

Figure 12. Polarization current distributions on layers 1—4 (c.f. Figure 10) calculated after implementing the integration procedure of this paper in the model of [62].



Layer 3



Layer 4

Figure 12 (cont'd). Polarization current distributions on layers 1—4 (c.f. Figure 10)) calculated after implementing the integration procedure of this paper in the model of [62].

5 INPUT REFLECTION COEFFICIENT OF A PATCH ANTENNA

In this section, we present two calculations of input reflection coefficient versus frequency. They correspond to two different models of a patch antenna — one used in this thesis, as described in Section 3, and one simplified, to be discussed shortly. Furthermore, better performance of our exact numerical integration technique, explained in Sections 3.6 and 3.7, over the traditional numerical tuning will be proven *on an antenna application*.

5.1 Approximate Solution

The first example is the frequency dependence of a rectangular patch fed by a 50-Ohm microstrip transmission line; the antenna's length is 3.85 cm, the width is 3.18 cm, the substrate has relative dielectric constant of 2.34 and is 1.568 mm thick. The model that was used for the patch is a simplified one — it assumes that current on the patch flows only in the direction of the feeding microstrip transmission line, and the ground plane (bottom metallization) is present in the model only indirectly, in the guided wavelength. In addition, the basis functions in the moment-method formulation are non-overlapping rectangular pulses along the length as well as the width of the metallic patch, and dielectrics and metallizations are assumed perfect. The assumptions, while perfectly valid once the application engineer is aware of the limitations imposed by them, are — indeed — only

approximations: It is true that unless a patch's width is much larger than its length, the dominant current component has the direction of the feeding microstrip transmission line; however, perpendicular components — directed along the antenna width — do appear as well. Similarly, the system of non-overlapping pulses employed in the role of basis functions is also an approximation — its ability to represent the continuous current distribution excited on the patch's surface is only limited, and the fact that the pulses do not overlap introduces fictitious bound charges that do not exist in the corresponding physical structure. In very much the same way, by employing the guided wavelength, which is calculated on the basis of an infinitely large substrate, the model cannot account for substrates of finite extent.

Applying the simplified model, we have calculated the input reflection coefficient of the patch described above; as we reported in [111], the integral of (3-30) was evaluated by means of numerical tuning. The calculation (dotted line) — compared with measurement [29] (dashed line) — is presented in Figure 13. Using the same simplified model, we then replaced numerical tuning with our exact integration technique, given by (3-34); the resulting curve is drawn as the solid line in Figure 13.

From Figure 13 it is evident that exact numerical integration leads to much better agreement — in both amplitude and phase — with measurement than numerical tuning. Furthermore, it requires less computer time, because no search for a “proper” value of the offset is needed. Also, it is noteworthy that the phase of the two calculated curves converges to zero at low frequencies — this is so because, by not having the ground plane in the simplified model directly, we cannot apply exciting voltage between the patch itself and the ground plane; instead, we apply the voltage along that section of the metallic patch that corresponds to the direction of the feeding microstrip. In terms of the moment-method formulation, this means there is an infinitesimal gap in the metallization of the feeding section, thus resulting in a phase change of π at low frequencies. In comparison, the measurement represents the standard excitation mechanism, in which the feeding voltage is

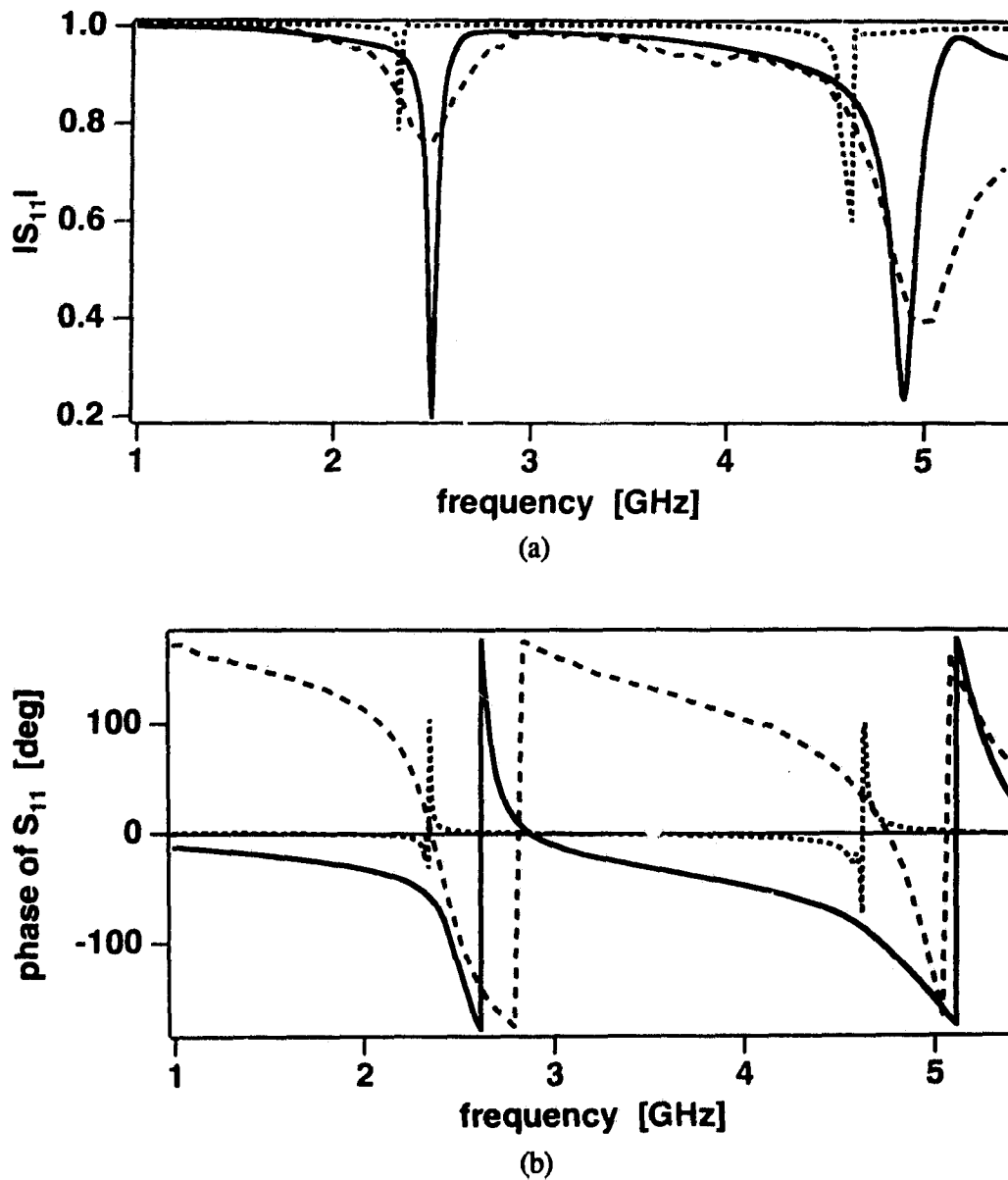


Figure 13. Frequency dependence of the input reflection coefficient — amplitude (a) and phase (b) — for a rectangular patch of length 3.85 cm, width 3.18 cm, substrate thickness 1.568 mm and substrate relative dielectric constant 2.34, according to the simplified model of [111]. Solid line: calculation based on our exact numerical integration, c.f. (3-34); dotted line: calculation based on numerical tuning [111]; dashed line: measurement [29].

applied between the upper and lower metallizations.

5.2 Full-Wave Solution

We have applied the full-wave model that this dissertation deals with and that is described in detail in Section 3 to the asymmetrically edge-fed rectangular patch of Figure 14. Our calculated values of $|S_{11}|$ (solid line) are plotted in comparison with measurement (dotted line) and significant measured values (square markers) of [69] in Figure 15a. We have attempted to reproduce the measured results as closely as possible. The calculated values confirm the measurement over the entire frequency band; while the length of the launching microstrip section in the measured prototype was not known, the calculation corresponds to the launcher 16.4 mm long. The slight ripple in the measurement is in [69] attributed to imperfections of measuring equipment. Because the radiator is fed asymmet-

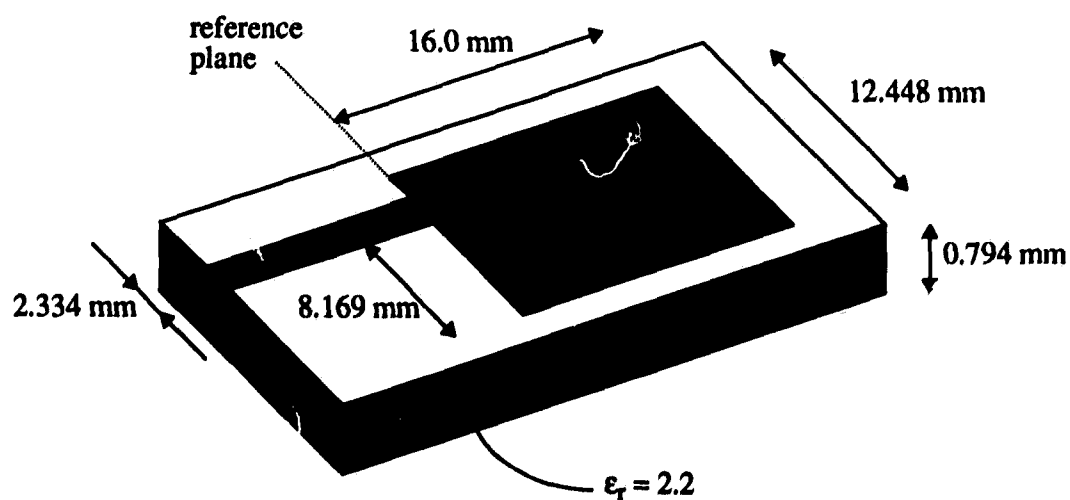
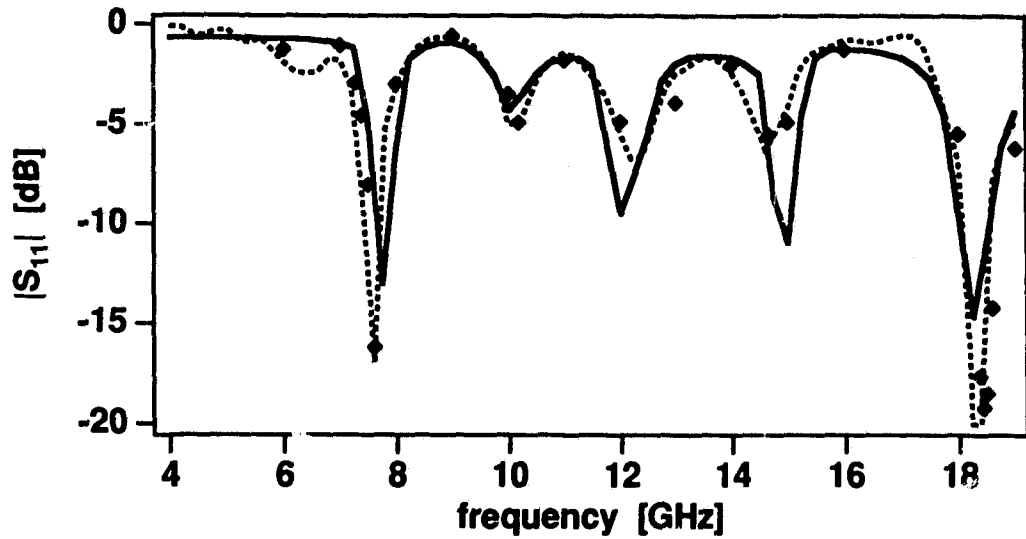


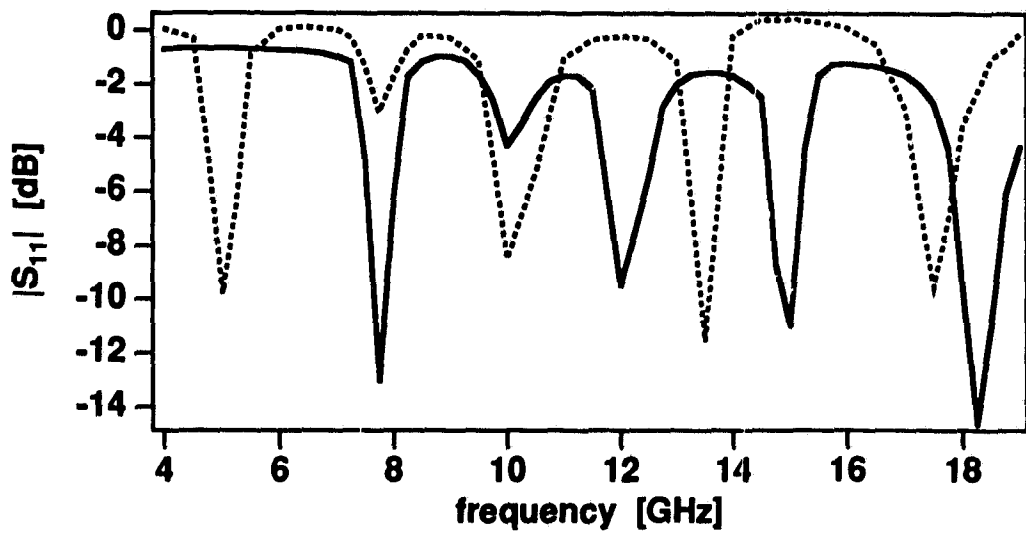
Figure 14. *Dimensions of asymmetrically edge-fed rectangular patch antenna.*

rically — unlike a symmetrically-fed patch, which resonates on the primary frequency (given by the position on the feeding point and patch dimensions with respect to guided wavelength) and its harmonics — this radiator resonates on a number of other frequencies: in addition to the primary resonant frequency of 7.6 GHz and what clearly is its harmonic at 14.67 GHz, the radiator resonates — to a smaller degree — at approximately 10.18, 12.0 and 18.43 GHz.

To shed yet more light on the behavior of the utilized numerical model, Figure 15b — beside our accurate calculation (solid line, identical with the solid line of Figure 15a) — presents also a curve (dotted line) of the input reflection coefficient calculated when the structure is divided into one half the number of elementary cells required, as discussed at the end of Section 3. Under insufficient discretization, the input reflection coefficient may acquire absolute values higher than unity — which means that the real part of input impedance is small but negative — and relationships along the frequency axis are shifted and non-linearly scaled. As the discretization becomes finer, the discrepancies pronounce themselves to a smaller degree and eventually vanish, once the dimensions of elementary cells become sufficiently small. From that point on, any further increase in discretization results in only minute changes of calculated physical quantities, which for all practical purposes are typically negligible and by far do not justify the increased demand on computer resources.



(a)



(b)

Figure 15. Frequency dependence of the amplitude of the input reflection coefficient for the asymmetrically edge-fed patch of Figure 14. Solid lines of (a) and (b): full-wave calculation based on our exact numerical integration; dotted line of (a): measurement [69]; square markers of (a): significant calculated values according to [69]; dotted line of (b): our calculation under insufficient discretization (c.f. remarks at the end of Section 3), for demonstration purposes only.

6 INPUT IMPEDANCE OF AN INSET-FED PATCH ANTENNA

A patch antenna with an inset feed, like the antenna whose geometry is depicted in Figure 16, is widely used in monolithic microstrip phased arrays. The point behind moving the feed point from the patch's edge to its interior is to feed the antenna at a place where — in comparison with the edge — the amplitude of current is higher, thus antenna input impedance lower.

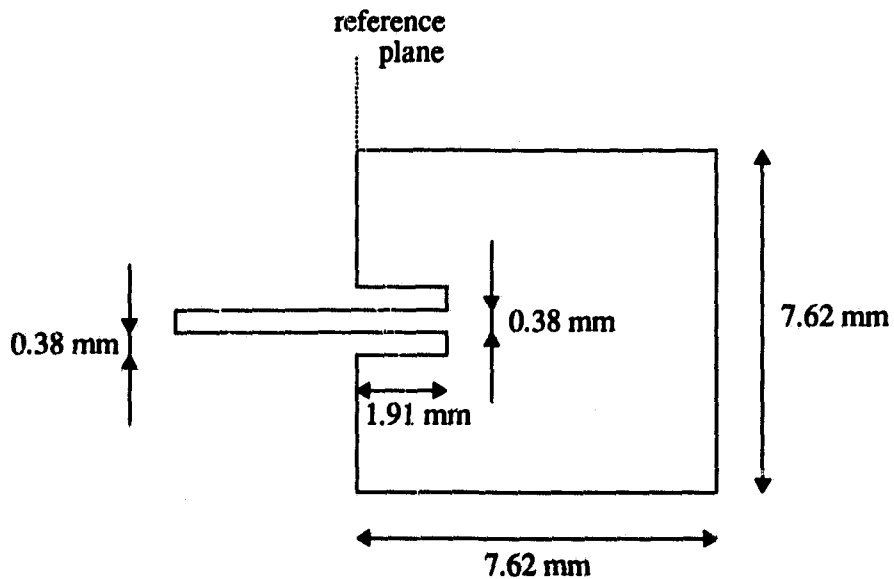


Figure 16. *Inset-fed rectangular patch antenna.*

In order to further test our numerical model and learn more about its behavior and performance, we have calculated frequency dependence for input impedance of the inset-fed rectangular patch of Figure 16; the substrate relative dielectric constant is 2.33 and thickness 1.575 mm. First, we excited the patch at the reference plane (c.f. Figure 16), as it is illustrated in Figure 17a. The corresponding input impedance curve is drawn in dashed line in Figure 18, where measured values [69] are represented by square markers. We found the frequency shift between measured and calculated values somewhat disconcerting. We hypothesized that the extension of the upper and lower metallizations across the thickness of the substrate — which is necessary to create the infinitesimal gap that excitation voltage is applied through — was in effect rendering the patch electrically longer, which would, indeed, give a lower resonant frequency. Therefore, an investigation into the matter was conducted. We enlarged the structure under analysis, by attaching an additional column of cells to the left of the reference plane (Figure 17b). Here again, the antenna is driven by a voltage applied across a delta gap within the conductor region of the patch, and the resulting calculated curve is drawn in solid line in Figure 18. The calculation

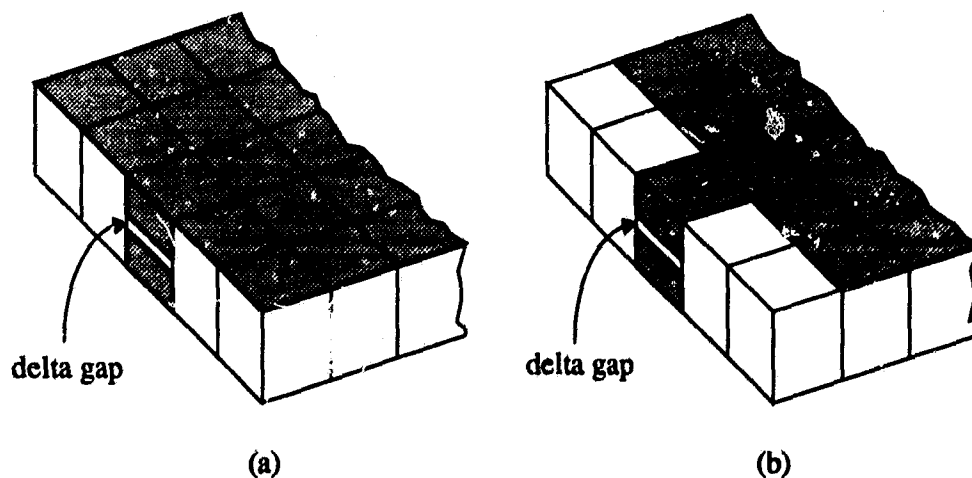


Figure 17. *Two feeding mechanisms for the rectangular patch antenna of Figure 16.*

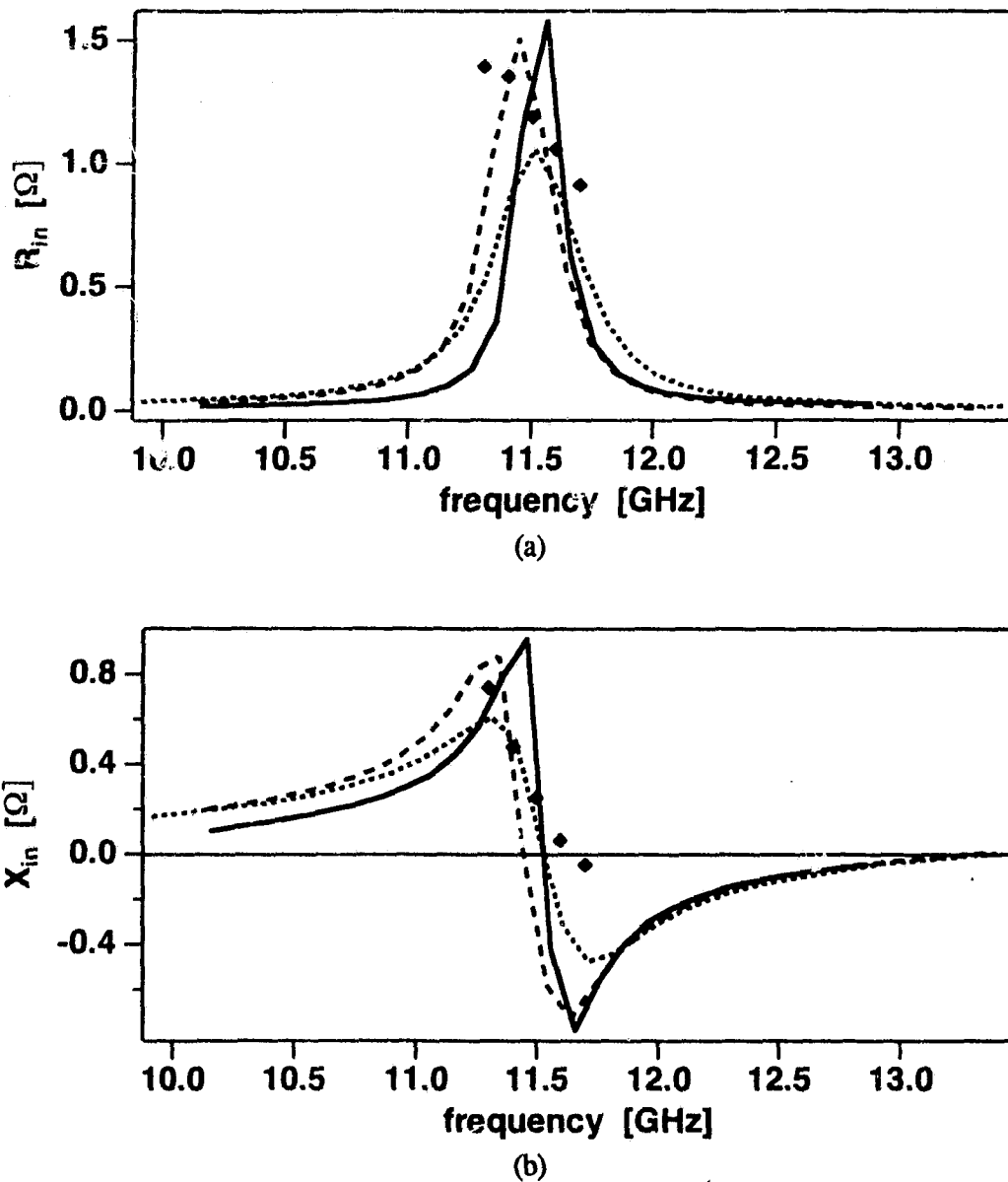


Figure 18. Frequency dependence of input impedance — real (a) and imaginary (b) parts — for the inset-fed rectangular patch of Figure 16, with the substrate relative dielectric constant 2.33 and thickness 1.575 mm. Dashed line: calculation for the feeding mechanism according to Figure 17a; solid line: calculation for the feeding mechanism according to Figure 17b; dotted line: calculation as the solid line, with an increased-conductivity dielectric substrate ($\tan \delta = 0.01$); square markers: measurement [69].

appears to confirm the hypothesis. When no microstrip launcher is inserted between the edge of the radiator and the delta gap, where excitation is applied, the corner functions associated with the two feeding currents actually penetrate the structure of the patch for one half of the cell dimension in the feeding-microstrip's direction (as discussed at the end of Section 3.5). Apparently due to the direct interaction between the feeding-currents corner functions and the radiator itself, the radiator's resonant frequency is affected. When a finite-length launcher section is inserted between the patch's edge and the feeding-currents corner functions, the resonance moves to a higher frequency, thus matching the measurement better.

The effect of resonant frequency shifting when the excitation is applied in a reference plane passing along the patch's edge was pronounced to a smaller degree in all other geometries. Apparently the fact that the transition between a microstrip transmission line and a patch — which by itself can be viewed as nothing else than a microstrip transmission line of a characteristic impedance different from that of the launcher — occurs at a place where the current is higher, makes the inset-fed patch geometry more sensitive to the phenomenon.

The results hitherto presented were calculated for metallic surfaces made of perfect conductors and substrates whose conductivity was that of RT Duroid (1×10^{-13} S/m). In the next calculation, perfect conductors of the feeding scenario defined by Figure 17b were replaced with copper. Calculated curves of frequency dependence for the real and imaginary parts of input impedance were within the plotting accuracy of those for perfect conductors in Figure 18. (It is noteworthy that the same behavior was observed in all subsequent calculations.)

As the logical next step, we increased conductivity of the dielectric to 1.49×10^{-2} S/m, i.e., losses in the dielectric rose to conform to $\tan \delta = 1 \times 10^{-2}$. This has resulted in the transition of solid curves in Figure 18 to the dotted ones. Not surprisingly, the loss increase has not affected the value of resonant frequency. Also as expected, the

resonant curves became wider and peaked at lower values, suggesting a significantly smaller quality factor. Because measured values of the equivalent lossy structure are not available, we consider the results to be at least a *qualitative* confirmation that the numerical model is also valid under lossy conditions.

7 FURTHER REMARKS ON INPUT IMPEDANCE/ ADMITTANCE OF PASSIVE COMPONENTS

In this section, we will discuss a few fine points associated with input impedance/admittance of passive components. Specifically, we will address one of their salient properties — the unique direct correspondence between the real and imaginary parts of their input admittance — and demonstrate how it can be beneficial in engineering analysis, design and verification.

First, as we described in [118], we will show that the imaginary part of an antenna input admittance can be calculated from its real part using Bode's integrals. Since the real part is typically a smoother function of frequency than the imaginary part, the procedure presented here requires computation at a smaller number of frequency points, thus saves time, and is ideal for systems whose input conductance exhibits sharp peaks. A numerical procedure to evaluate the singular Bode's integral will also be presented. Numerical examples using a wire antenna will be used to illustrate the advantages of this approach compared to calculations involving a densely scanned frequency range. The noise stability and robustness of the algorithm will be demonstrated through the successful prediction of the susceptance and the resonant frequencies of the antenna in the presence of random noise in the conductance.

Second, with finesse we will use Bode's integrals to verify the validity of predicted input impedance — obtained through the thin-wall numerical model that was introduced in Section 3 — for a short-circuited section of a microstrip transmission line.

7.1 Bode's Integrals

The integral relations between real and imaginary parts of response functions are widely used in quantum field theory, nuclear physics and solid state physics. Unfortunately, this extremely useful tool does not seem to find much use in microwave engineering. These integral relations are known under a variety of names. The Kramers-Kronig relations between the real and imaginary parts of the dielectric constants are well known to engineers and physicists. In quantum field theory and quantum many-body theory, they are sometimes known as Lehmann or spectral representations or dispersion relations [119], whereas mathematicians refer to them as Hilbert Transforms. In circuit theory, they are often called Bode's integrals, since Bode seems to have been the first to use them [120].

The Kramers-Kronig relations enjoyed substantial popularity in the sixties among researchers in optics, where it is possible to measure the imaginary part, since it is related to light (electromagnetic) absorption [121]. Once the imaginary part is known, these relations are used to calculate the real part. Such relations also provide a set of constraints on the moments of the functions involved as well as their asymptotic behavior and are very useful tools to check the numerical accuracy of the calculations [120], [122].

One of the most intensive numerical problems in modern antenna analysis and design is the accurate calculation of the resonant frequency, especially for antennas with sharply peaked input conductance. For such antennas, the imaginary part of the admittance oscillates violently around the resonant frequency, thereby requiring its evaluation at a very large number of frequency points in order to accurately predict the location of the resonance. Although empirically derived formulas for admittances and resonant frequencies of certain types of antennas exist, they are of low accuracy (e.g., $\pm 20\%$ for helices [123]) or not known at all for other structures, such as those involving anisotropic and lossy materials [124]. For all of these systems, however, the real part of the input admittance, although having sharp peaks, is much easier to describe than its

imaginary part, hence requiring fewer computations around the peak which can locally be approximated by a Lorentzian.

Fortunately, it is for these numerically demanding situations that Bode's integrals will be shown to work best. Indeed, the presence of a sharp peak in the real part determines the local behavior of the imaginary part because of the singularity in the integrand. Thus, it is possible to reliably predict the resonant frequency and susceptance from the real part without accurately reproducing the entire frequency dependence of the susceptance.

Since the presence of a Cauchy Principal-Value in these integral relations poses a numerical problem, which should be handled with care, a numerical procedure using cubic splines to calculate these integrals is presented. It is similar to the modified Simpson rules presented in [125] but, we feel, is more appropriate for real life quantities which are expected to be smooth functions.

The derivation of Bode's integrals is not presented here, the reader is referred to the literature for the details [120], [121], [126]. We only need to stress that they apply to any *linear response* function of a physical and causal system [126]. There are situations where the presence of poles on the imaginary axis renders the relationship between the real and imaginary parts nonunique [120]. Such situations do not represent physical reality, since there are always losses in the system which eliminate such pathologies. Care must, however, be taken in determining what a response function is. The admittance of a system represents its linear response (current) to an applied voltage. The causality and linearity of the response alone guarantee that the conductance and susceptance satisfy the following integral relationships [120], [126]

$$B(\omega) = \frac{2\omega}{\pi} P \int_0^{\infty} \frac{G(x) dx}{x^2 - \omega^2}, \quad (7-1)$$

$$G(\omega) = G(\infty) - \frac{2}{\pi} P \int_0^{\infty} \frac{x B(x) dx}{x^2 - \omega^2}. \quad (7-2)$$

Here P stands for the Cauchy Principal-Value, $G(\omega)$ is the input conductance and $B(\omega)$ the input susceptance. These two equations will be referred to as Bode's integrals [120].

In this paper only the first relation will be used, for the real part is much smoother than the imaginary part, thus fewer data points are needed to adequately describe it. In other areas, it is usually the imaginary part that enjoys this property, which explains why it is this quantity that one calculates first. In some cases, it is also possible to measure the imaginary part, since it is related to the absorption of the incident excitation, such as optical absorption, for example.

To illustrate the usefulness of these relations, we consider a resistance R in series with a capacitance C . Without loss of generality, we take the values of R and C to be unity; $R = 1$ and $C = 1$. The real and imaginary parts of the admittance of this circuit are:

$$G(\omega) = \frac{\omega^2}{1 + \omega^2}, \quad (7-3)$$

$$B(\omega) = \frac{\omega}{1 + \omega^2}. \quad (7-4)$$

It is straightforward to check that these two quantities satisfy Bode's integrals.

The situation that we are interested in involves a real part that is numerically known on a set of frequency points. The conductance of an antenna has maxima whose sharpness is determined by the q -factor that we define as the reciprocal of the difference between the two half-amplitude points in the first peak,

$$q = \frac{1}{\Delta x}. \quad (7-5)$$

Here, x is a dimensionless quantity, such as the ratio of a characteristic length of the antenna (often the largest dimension) to the wavelength in free space. For large values of q , the imaginary part oscillates rapidly and changes sign around the values at which the real part peaks. Accurately describing the imaginary part in these regions from a direct solution can be numerically costly, because a large number of frequency points is needed.

This subsection presents a technique to numerically evaluate the Cauchy Principal-Value integral in (7-1). The idea is similar to the one used in deriving the modified Simpson rules in [125], except that a cubic spline — instead of a local second order polynomial — is used for interpolation. The use of the cubic spline guarantees the smoothness of the interpolation, as the function and its first two derivatives are required to be continuous [113], [127].

It is advantageous to split the integral in (7-1) into two parts, each of the following form:

$$F(x) = P \int_{-\infty}^{\infty} \frac{f(y) dy}{y-x} . \quad (7-6)$$

Equation (7-1) is consequently reduced to two integrals of the type given by this last equation, on which we now concentrate.

A popular numerical integration technique is the Legendre-Gauss quadrature, where the weights and the mesh on which the function is evaluated are chosen such that the technique is exact for polynomials up to a given order. This technique, which is well suited for functions that can be approximated by polynomials, is usually used to carry out the numerical integration in (7-6), often with the trick of subtracting the singularity [128]. However, such a procedure is not numerically stable for functions varying rapidly around the point x [125]. Also, the quadrature approximates the entire integrand $f(y)/(y-x)$ by polynomials; instead, here we only approximate the function $f(y)$ by

a cubic spline. It is much easier to accurately approximate $f(y)$ than the integrand, because of the presence of the singularity. We, therefore, assume that the function $f(y)$ is known at a set of points $y_i, i = 1, 2, \dots, N$, where it has values s_i . A cubic spline is built from these points, following the standard procedure; the reader is referred to the literature for details [113], [127]. Once this is done, the integral in (7-6) is reduced to the sum of the contributions of each interval $[y_i, y_{i+1}]$. The result is

$$F(y) = \sum_{i=1}^N F_i(y), \quad (7-7)$$

where

$$\begin{aligned} F_i(y) = & \frac{y_{i+1}^3 - y_i^3}{18(y_{i+1} - y_i)} (z_i - z_{i+1}) - \frac{y_i + y_{i+1}}{12} \{ y(z_{i+1} - z_i) \\ & + 3(y_{i+1}z_{i+1} - y_i z_{i+1}) \} - \frac{1}{6(y_{i+1} - y_i)} \{ (s_{i+1} - s_i)(6y + y^3) \\ & - 6y_{i+1}s_i + 6y_i s_{i+1} - yy_i^2 z_i - 3y^2 y_{i+1} z_i + 2yy_i y_{i+1} z_i + y_i^2 y_{i+1} z_i \\ & + 2yy_{i+1}^2 z_i - 2y_i y_{i+1}^2 z_i + 3y^2 y_i z_{i+1} - 2yy_i^2 z_{i+1} - 2yy_i y_{i+1} z_{i+1} \\ & + 2y_i^2 y_{i+1} z_{i+1} + yy_{i+1}^2 z_{i+1} - y_i y_{i+1}^2 z_{i+1} \} \ln \left| \frac{y - y_i}{y - y_{i+1}} \right|. \quad (7-8) \end{aligned}$$

The quantities z_i are the derivatives calculated when constructing the spline [113], [127].

When y is large, it is usually advantageous to expand the integrand in (7-6) in powers of $1/y$ and then carry out the integration, thereby avoiding roundoff errors, which are dominant because of the strong cancellations that take place [125].

Now we apply Bode's integrals to calculate the susceptance of a wire antenna from its conductance. We assume a lossless wire antenna of length L fed at the center. The wire of diameter $2a$ is assumed lossless and radiating in free space.

The method of moments is used to calculate the input admittance of the antenna as a function of frequency; the code was checked against the results presented by Harrington in [101]. Figure 19 shows the input conductance of a dipole as a function of the

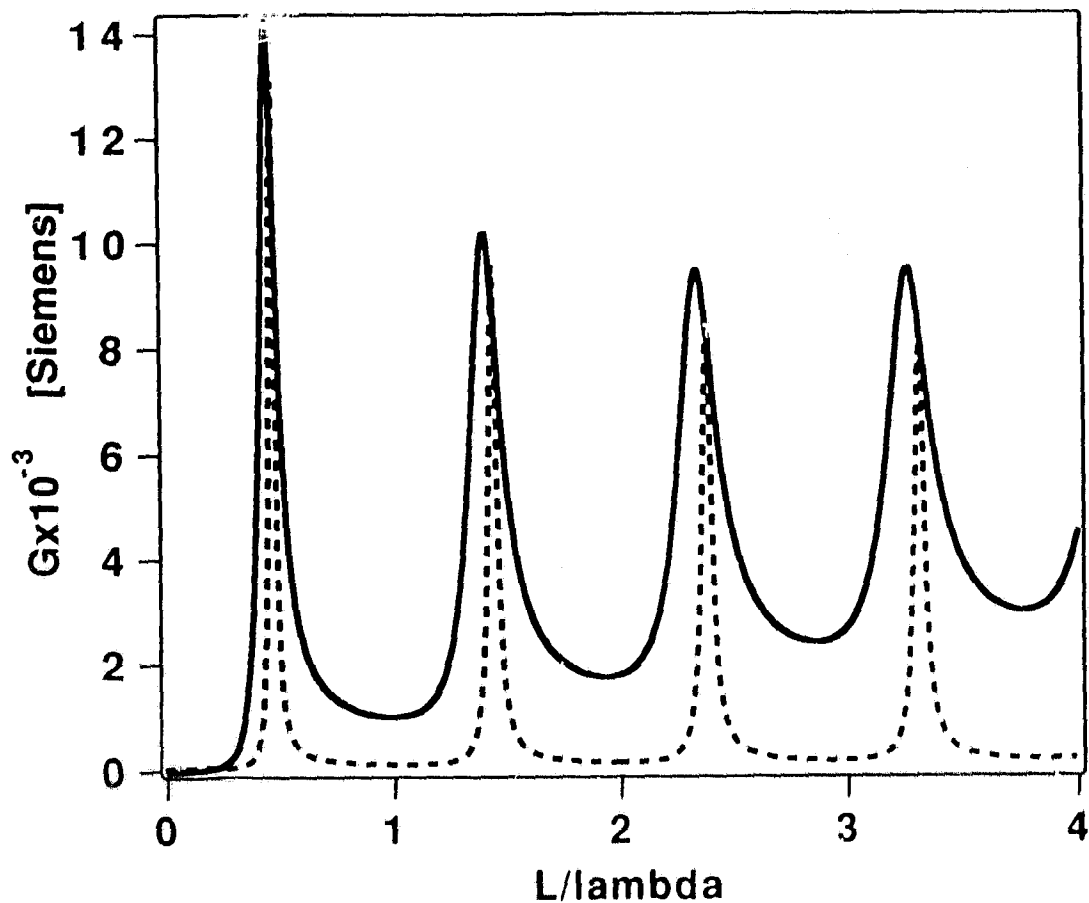


Figure 19. Input conductance of a wire antenna as a function of L/λ_0 , $q = 11.11$ (solid line) and $q = 33.33$ (dashed line).

ratio L/λ_0 for $L/2a = 74.2$ (solid line, $q = 11.11$), and $L/2a = 10^4$ (dashed line, $q = 26.3$). Our results for the case $L/2a = 74.2$ agree with those in [101] to within the readability of the latter. The conductance was calculated at 400 frequency points in both cases. Figure 20 shows the input susceptance calculated directly using the method of moments (solid line) and the one obtained through the present technique for $L/2a = 74.2$. It is evident that the

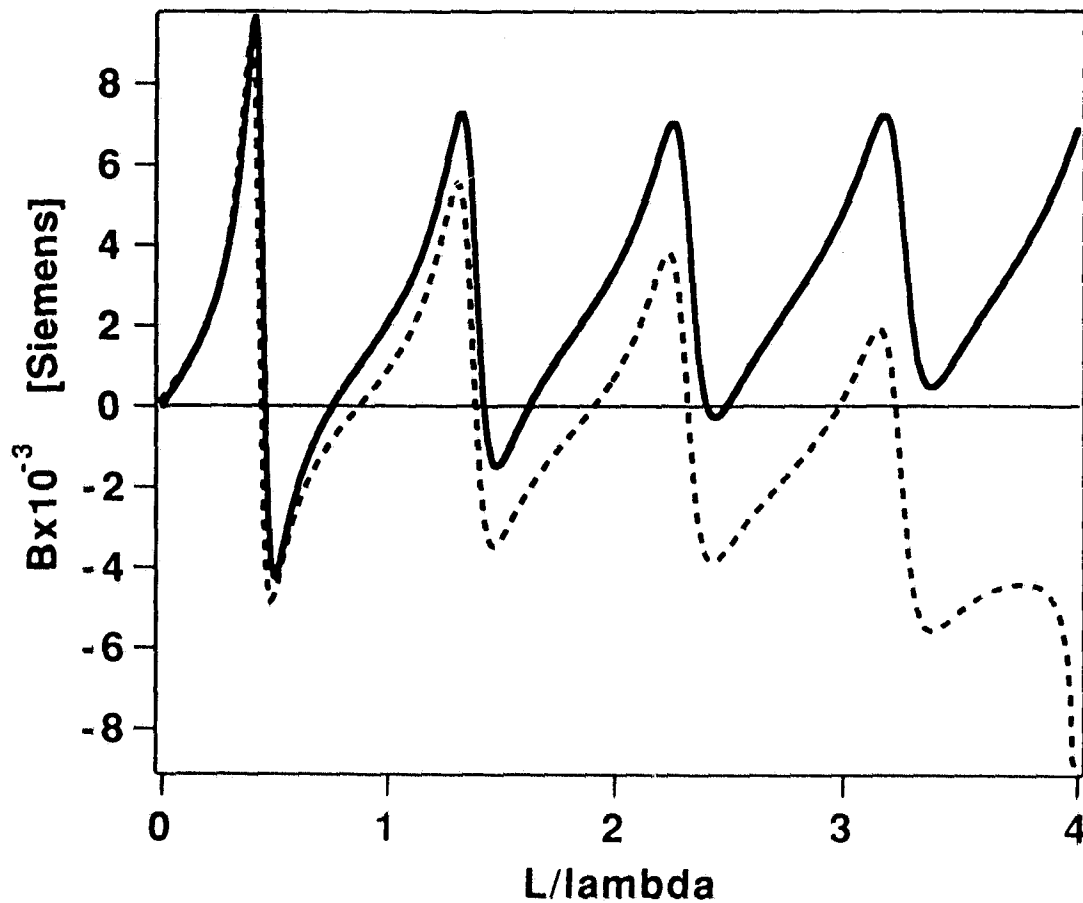


Figure 20. *Input susceptance of a wire antenna as a function of L/λ_0 . $q = 11.11$. The solid line is the direct method-of-moments solution and the dashed line is obtained through Bode's integrals.*

present method fails in the high frequency region but approximates the first resonance reasonably well. The origin of the discrepancy can be traced back to the fact that the integral in (7-1) extends over the entire real axis, which is not possible to incorporate into the present situation. The agreement improves rapidly if the real part is calculated over a wider range of frequencies. Despite this shortcoming, the method locates the first resonance reasonably well. For this case, where the peaks of the real part are not sharp, it is possible to approximate the real part over a wide range of frequencies without using a large number of points, thereby allowing the resonances to be more accurately located using the Bode's integrals. The agreement in susceptance is even much better when the peaks in the conductance are sharper, as shown in Figure 21. The solid curve is the direct method-of-moments solution. Locating the zeros of the susceptance-directly can be very time consuming. It is in this situation that the present method is most useful. As Figure 21 shows, the resonances are located within plotting accuracy, even though the two curves are distinct over the region between the resonances and at the right edge of the plot. The sharper the peaks in the conductance, the better the agreement and consequently the more reliable the present method is. Our investigations have shown that for values of q larger than 15, the first resonant frequency is predicted within plotting accuracy if only the first peak in the input conductance is used, i.e., the range $0 \leq L/\lambda_0 \leq 1$ in Figure 19.

It is worth pointing out that Bode's integrals allow an adequate description of the susceptance as long as the conductance is well described by the number of frequency points used. Figure 22 shows the susceptance obtained from only 50 frequency points in the conductance (dashed line) and the method-of-moments solution (solid line) calculated at 400 points. It is clear that the differences between the dashed curve of Figure 21, obtained from 400 points, and that from 50 points (dashed curve of Figure 22) are minor, especially around the resonant frequencies; in other words, the presented example results in eight-fold reduction of required CPU time.

Successful application of the present technique to calculate the input susceptance from measured profiles of the input conductance requires its stability to the errors inherently introduced by the measurement. To simulate these errors, random oscillations were superimposed on the calculated values of the conductance G . The oscillations represent a 10% random error in G .

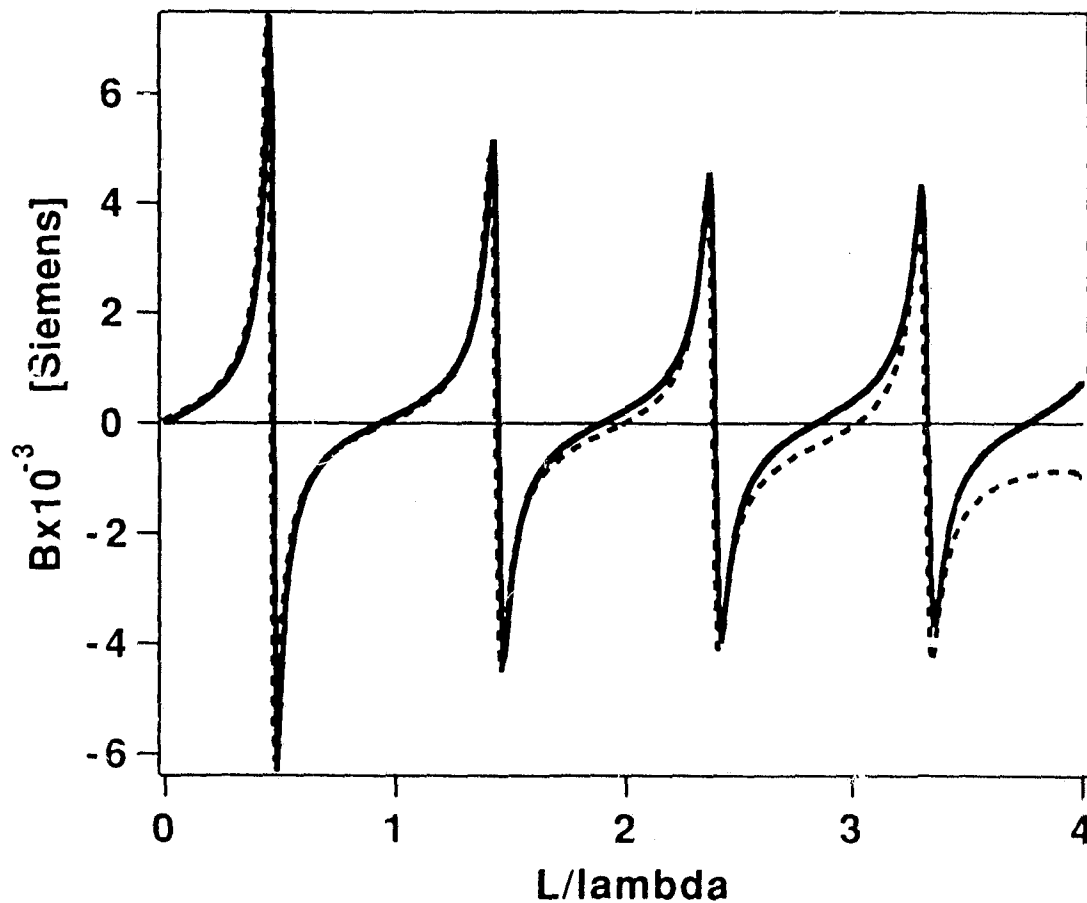


Figure 21. *Input susceptance of a wire antenna as a function of L/λ_0 . $q = 33.33$. The solid line is the direct method-of-moments solution and the dashed line is obtained through Bode's integrals, where the conductance was calculated at 400 frequency points.*

Figure 23 shows a plot of the corrupted real part of the input admittance for $q = 26.3$. Figure 24 shows the calculated imaginary part using the corrupted real part. Clearly, the resonant frequencies are accurately, the susceptance satisfactorily, predicted despite the presence of the corrupting noise. The inset shows the imaginary part obtained from only one single peak of the noisy real part. The resonant frequency and susceptance

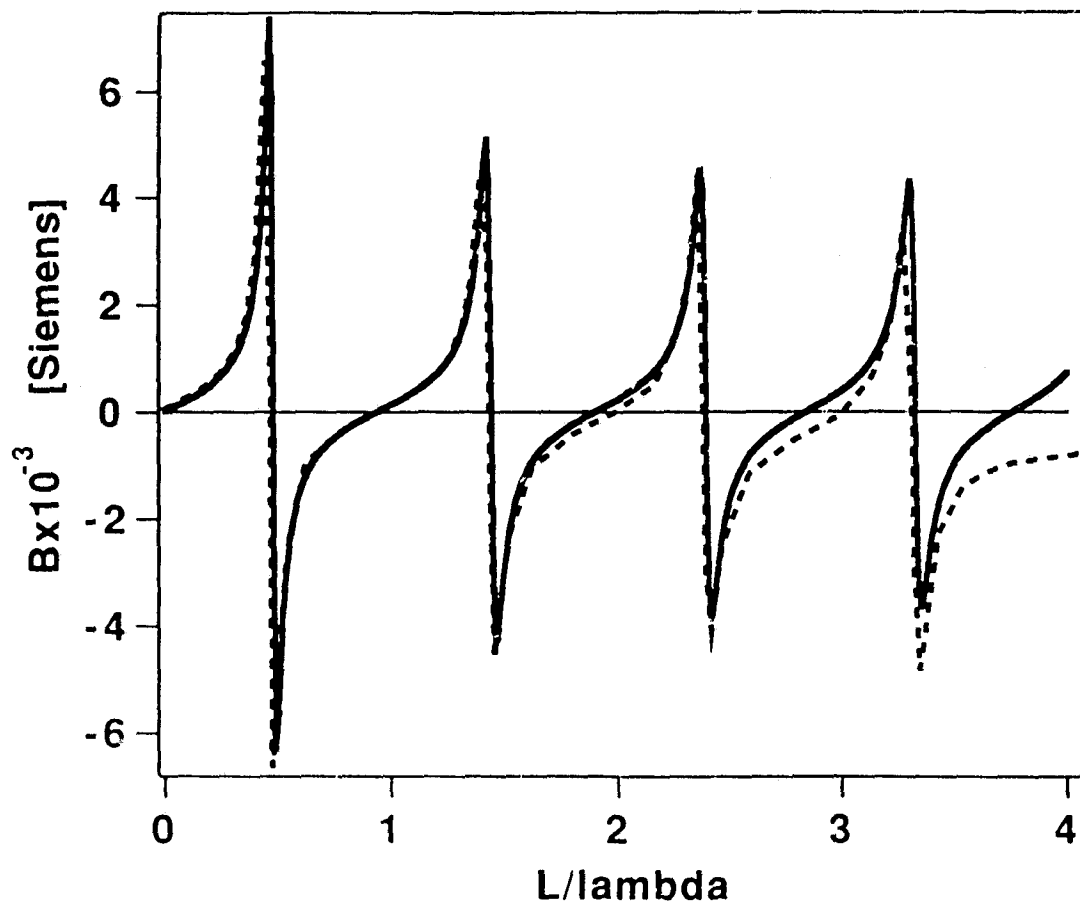


Figure 22. *Input susceptance of a wire antenna as a function of L/λ_0 . $q = 33.33$. The solid line is the direct method-of-moments solution and the dashed line is obtained through Bode's integrals, where the conductance was calculated at 50 frequency points.*

are again satisfactorily predicted despite the presence of the random errors and the reduced number of frequency points.

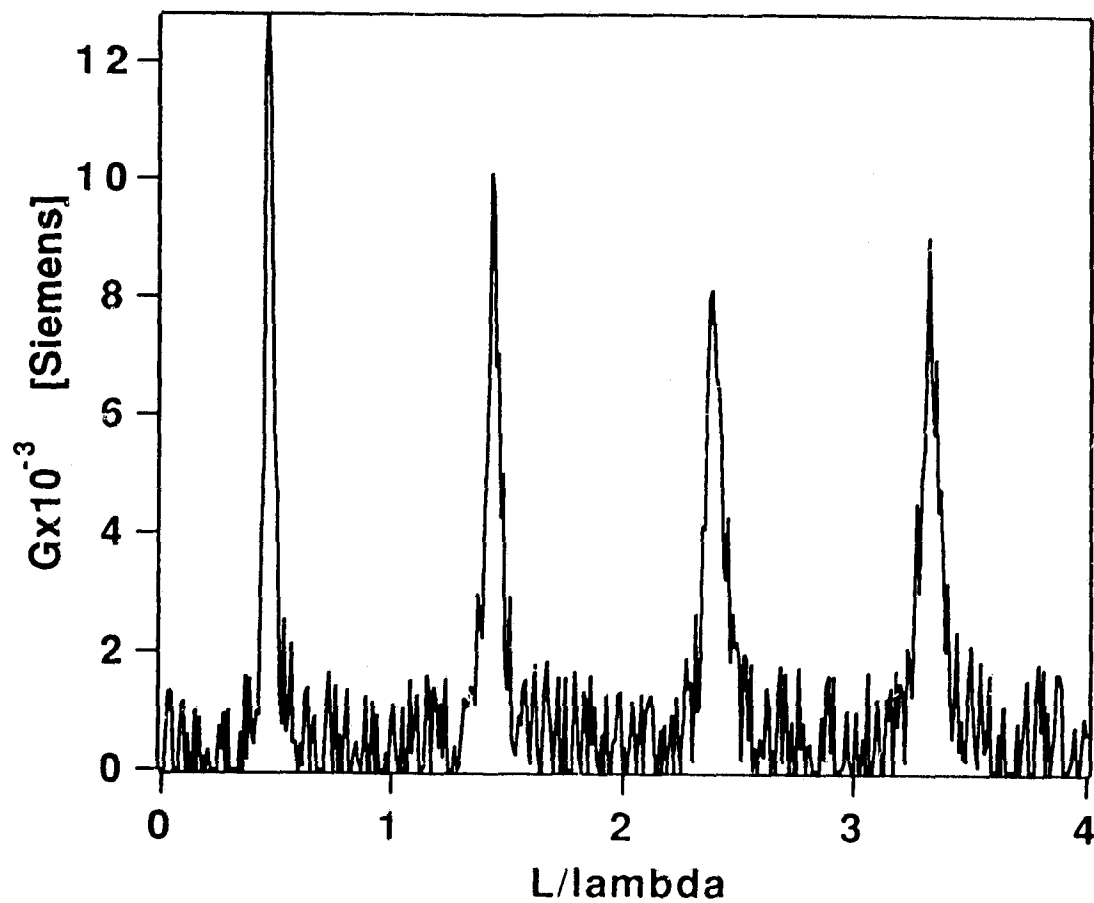


Figure 23. *Input conductance G of a wire antenna with $\pm 10\%$ (± 1.3 mS) of noise superimposed. (Note that negative conductances are eliminated by setting the respective values to zero.)*

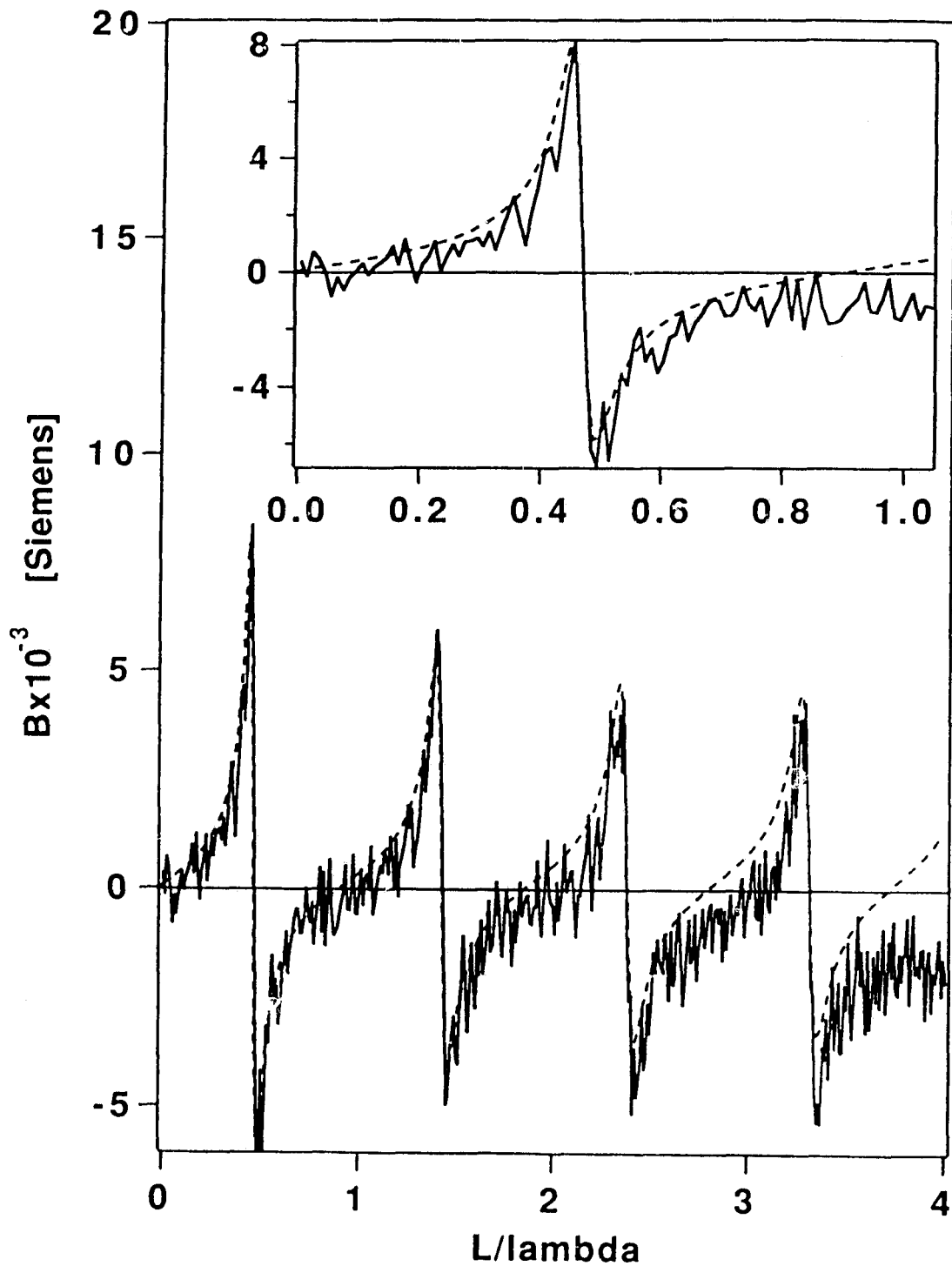


Figure 24. Calculated input susceptance B corresponding to conductance of Figure 23 (solid line) and conductance without noise (dashed line). The inset is the input susceptance calculated from only the first peak, $0 \leq L/\lambda_0 \leq 1$, of the conductance in Figure 23.

In summary, since the real part of an antenna's input admittance versus frequency is usually a smoother function than the imaginary part, Bode's integrals can be applied to significantly reduce computation times for admittance calculations. By using a cubic spline interpolation for the conductance in the numerical integration, the number of actual input admittance analyses can be reduced by at least a factor of eight — or even higher if the accuracy in the susceptance function is slightly sacrificed — while still satisfactory results are obtained for the resonances (zeros of susceptance). The algorithm is robust in the presence of random noise and can therefore be used *to validate* or improve measurements.

7.2 Input Impedance of a Short-Circuited Microstrip Transmission Line

We have calculated input impedance as a function of frequency for the structure of Figure 25 — a short-circuited section of a microstrip transmission line. Figure 26 details currents in the feeding region of the analyzed circuit. The physical nature of the model requires to apply feeding voltage across a delta gap located within the conductor region. As a result, voltages associated with the currents I_1 and I_2 are the ones that provide excitation. With I_1 and I_2 as excitation currents and V_1, V_2 as voltages accompanying the two currents, input impedance of the structure — and other objects that involve metallic surfaces — in the employed model is evaluated as:

$$Z_{in} = \frac{V_1}{I_1} + \frac{V_2}{I_2} = 0.5 \left(\frac{1}{I_1} + \frac{1}{I_2} \right). \quad (7-9)$$

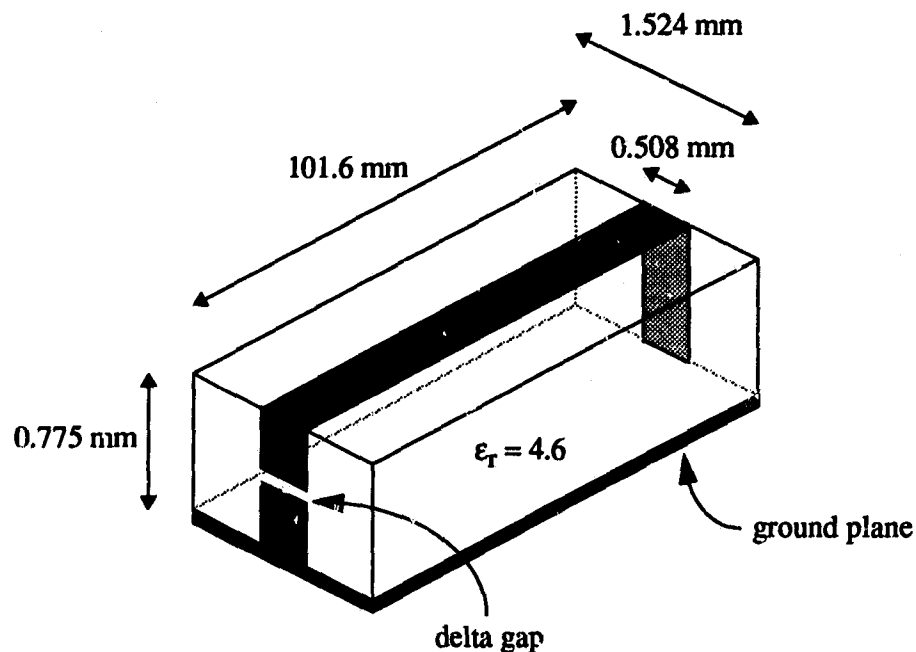


Figure 25. *Geometry of the analyzed short-circuited section of a microstrip transmission line.*

Both voltages are set to 0.5 V, because it is the total applied voltage, $V_1 + V_2$, that — by definition — has to be unity.

Figure 27 presents our calculated input impedance. Upon inspection, the values of X_{in} at low frequencies — besides the resonant frequency reduced by the factor of two — are what sets the short-circuited arrangement apart from the open-ended variety. As frequency approaches zero, Z_{in} converges to $0 - j\infty$, which is in agreement with the conclusions drawn by Schelkunoff [129], who derived analytical expressions for the input impedance of a wire loop as a function of the distance between the ends of the wire and the shapes and dimensions of the wire endings.

In order to verify whether the real and imaginary parts of the input impedance are calculated accurately, we applied the Kramers-Kronig application (Bode's integrals) of Section 7.1 in the following way: First, we converted the calculated input im-

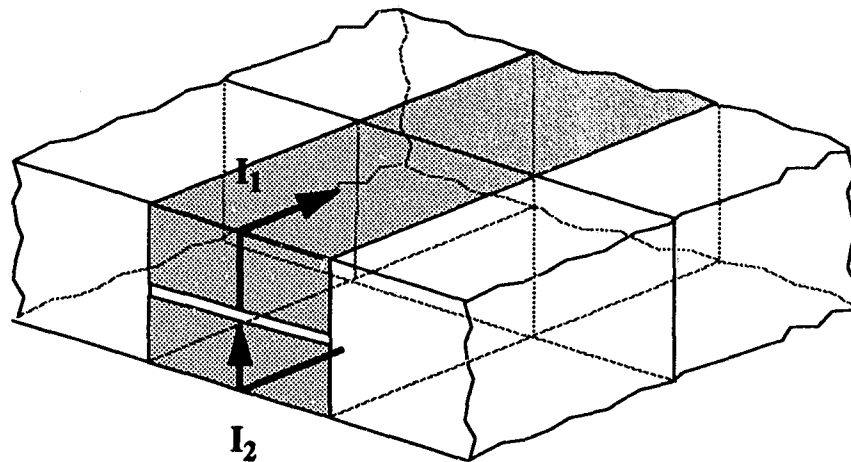


Figure 26. Feeding region and excitation currents of the structure depicted in Figure 25.

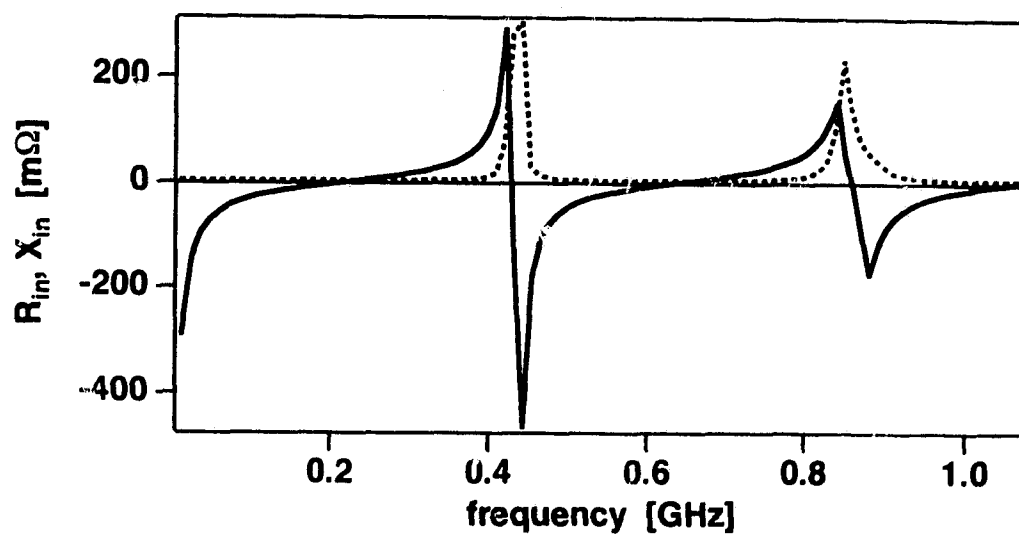


Figure 27. Frequency dependence of input impedance for the structure of Figure 25. Dotted line: calculated real part; solid line: calculated imaginary part.

pedance (as a function of frequency) to input admittance, Y_{in} , and subsequently — through Bode's integrals — used only the real part of Y_{in} to reconstruct the imaginary part. Figure 28 shows the imaginary part of Y_{in} that we started with and the *reconstructed* input susceptance, B_{in} . The evident good agreement validates our calculated curves of input impedance. The lower values of the reconstructed component around the first resonance mean nothing more than an indication that input impedance should have been evaluated in more points in that frequency range.

The short-circuited section of a microstrip transmission line is one of the examples published in the paper that this dissertation follows up on [62] (no measurement is available). The real part of input impedance is reported to reach $260 \text{ m}\Omega$ at the first resonance; the value compares with $301 \text{ m}\Omega$ of our calculation (Figure 27). The X_{in} calculation of [62] is presented as Figure 29. Considering that the graph has clearly been

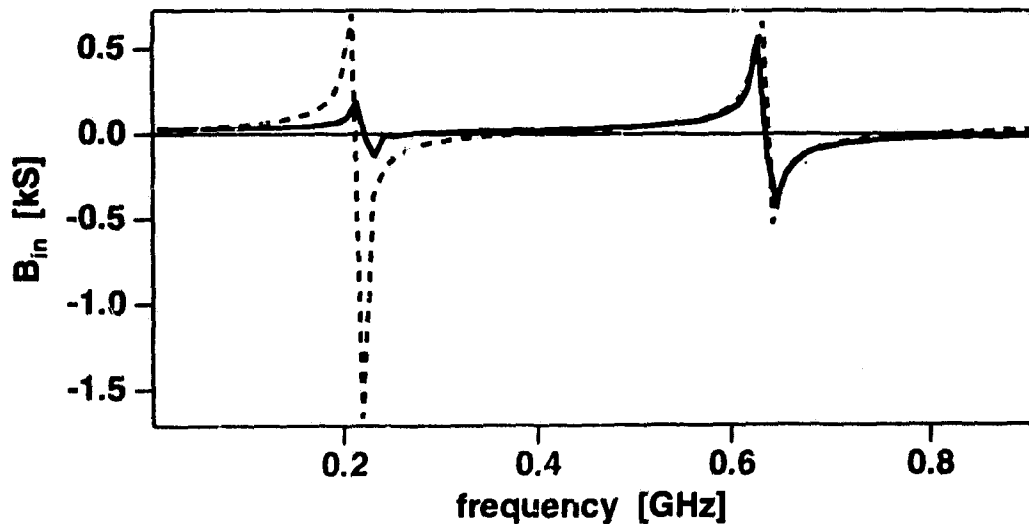


Figure 28. *Frequency dependence of input susceptance for the structure of Figure 25. Dashed line: obtained from input impedance; solid line: reconstructed through Bode's integrals.*

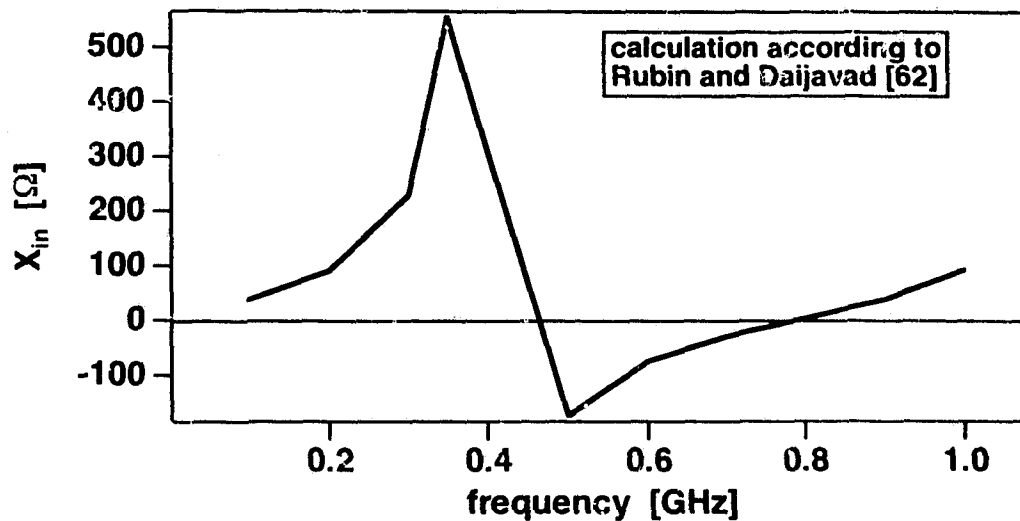


Figure 29. Frequency dependence of input susceptance for the structure of Figure 25 as published in [62].

constructed from no more than ten points, our calculated resonant frequency fairly well agrees with the one of [62]. However, we find two points about Figure 29 that should not go unnoticed: First, the calculation of [62] fails to predict the effects of the delta-gap capacitance that dominates at low frequencies — the value of X_{in} at 100 MHz is 37.5 Ω , comparing to our value of -28.5 m Ω at the same frequency. Second, the first resonance occurs at 464.1 MHz; yet even at the frequency as high as 1 GHz, the second resonance has not been reached. We can only reproduce the results of Figure 29 if we use the somewhat arbitrary integration algorithm of [62].

8 EFFECTS OF FINITE-EXTENT SUBSTRATE

We have investigated whether — and if positive, then how — substrates of finite extent affect performance of planar structures. Two topologies were studied. They are depicted in Figure 30, where the topology of Figure 30b was created by simply extending the topology of Figure 30a on two sides. Both structures are two-ports. Each consists of a square metallic

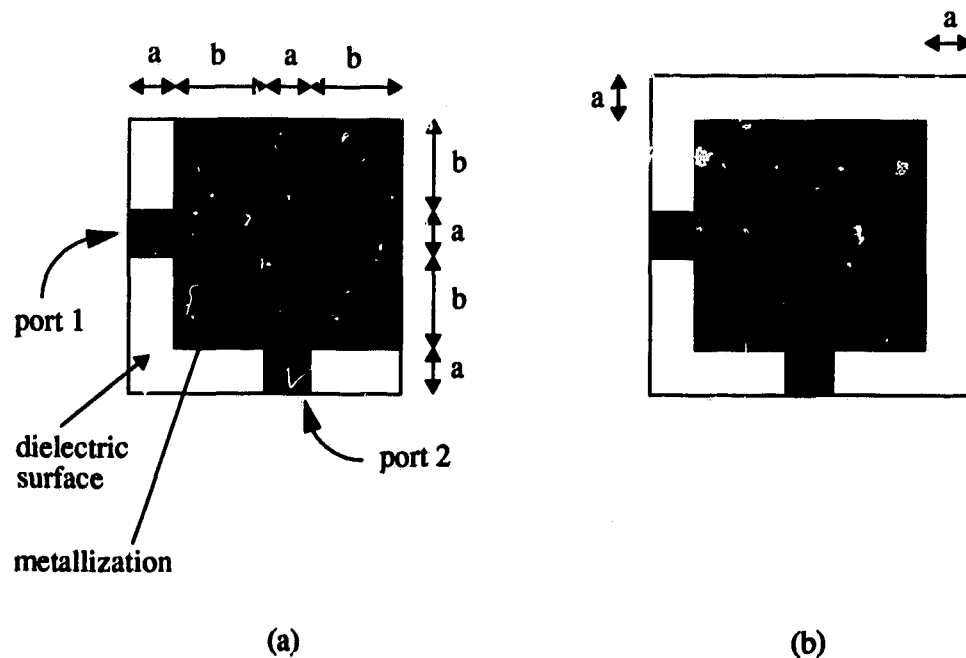
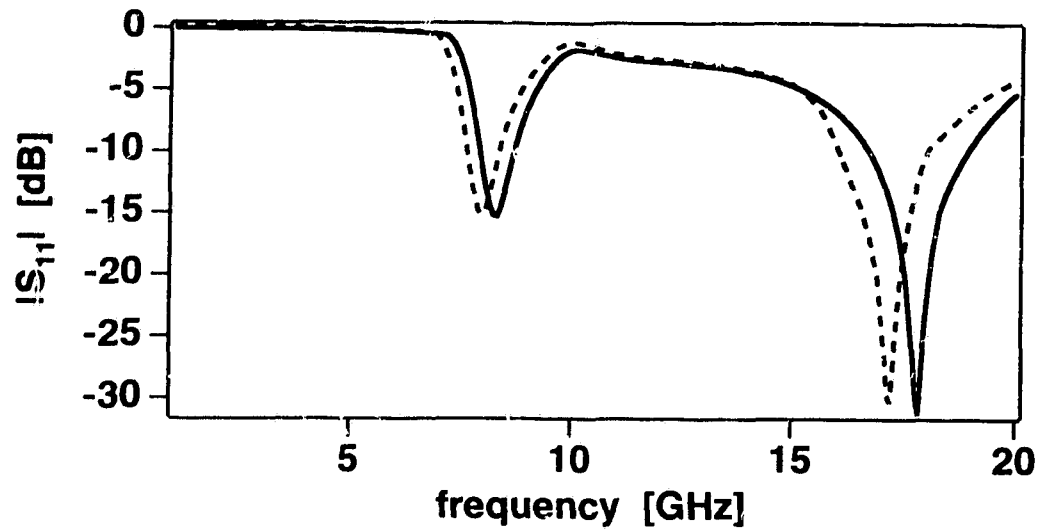


Figure 30. Topologies examined in study of effects of finite-extent substrates. Dimensions: $a=1.036$ mm, $b=2a$; dielectric thickness 1.423 mm, material properties are those of gallium arsenide at 25 degrees C. Port 2 matched.

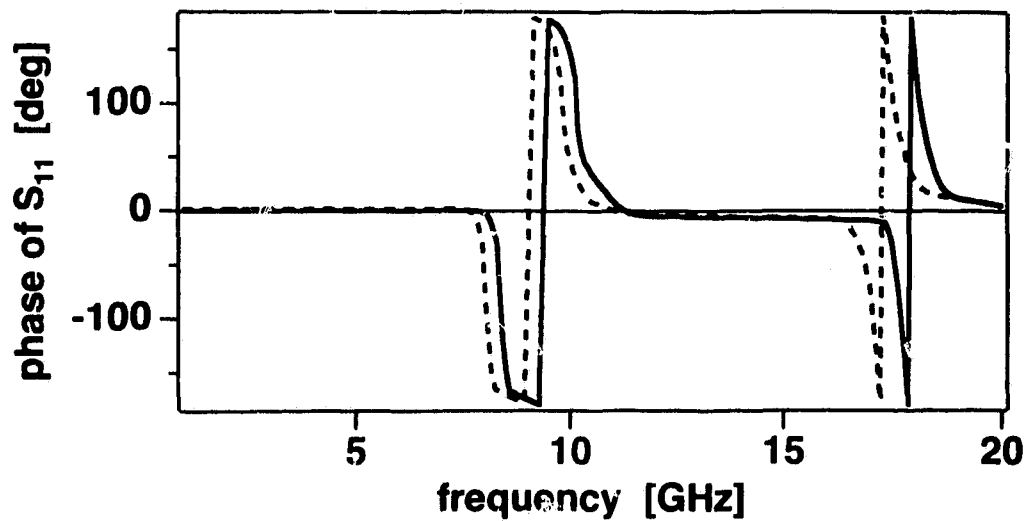
patch, fed by a 50-Ohm microstrip transmission line. At a 90-degree angle with respect to the feeding microstrip, a second port at the edge of the patch is formed — by attaching a section of a 50-Ohm microstrip. The material parameters are those of gallium arsenide at 25 degrees C.

Performance of the two two-ports, in terms of S_{11} and S_{21} parameters, is shown in Figures 31 and 32. Convergence analysis confirmed stability of the calculated results up to at least four significant figures.

The structure of Figure 30a resonates at lower frequencies than its extended alternative (Figure 30b), apparently due to higher fringing fields — note that the extent of the ground metallization is dictated by the size of the substrate. Since we have employed the volume equivalence theorem, the currents of the structure of Figure 30a already account for all scattered fields — including the fringing fields. Noteworthy is also the fact that in Figure 31 the resonance at the second harmonic is stronger than at the primary resonant frequency. To resolve this seemingly surprising behavior and directly relate the input reflection coefficient with the transmission response (Figures 32), we have calculated the total power radiated by the structure (Figure 33). From Figure 33, it is evident that the strongest radiation occurs at the two resonances of S_{11} . In between these two frequencies, radiation is significantly reduced and a substantial amount of power reaches the second port, thus causing a maximum in the transmission coefficient S_{21} . The frequency at which the highest outflow of power through port 2 occurs is close to the primary S_{11} resonant frequency, resulting in a slightly subdued radiation at the primary resonance of S_{11} in comparison with radiation at the second harmonic.

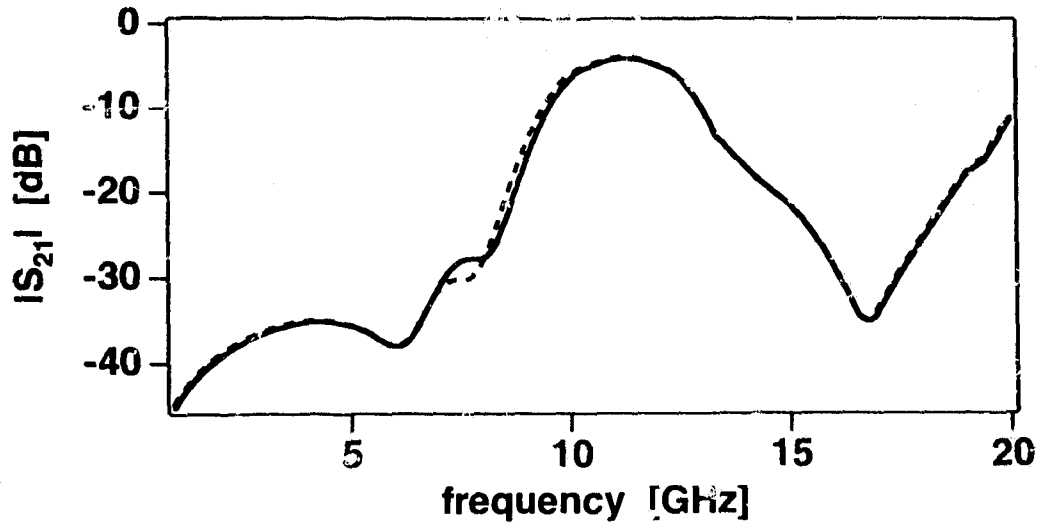


(a)

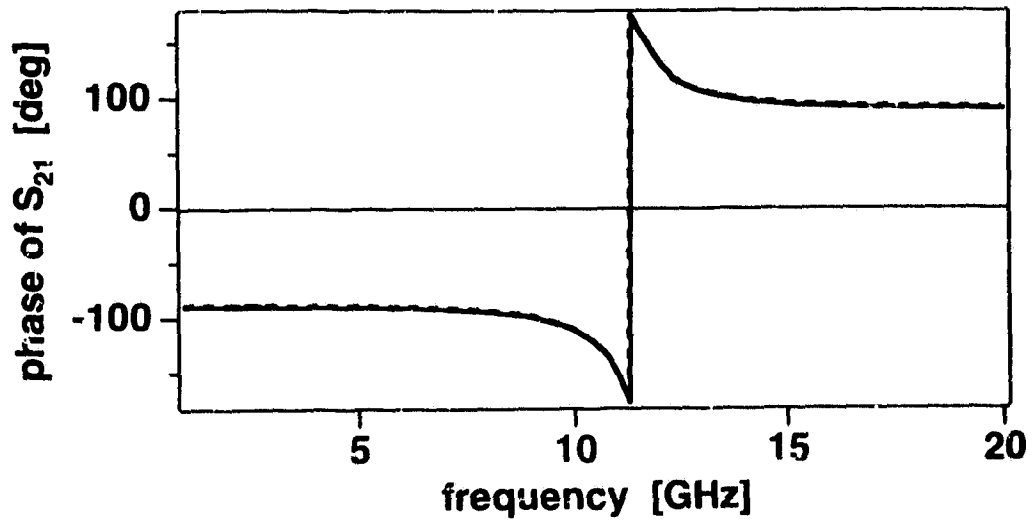


(b)

Figure 31. Frequency dependence of input reflection coefficient — amplitude (a) and phase (b) — for the two-ports of Figures 30a (dashed line) and 30b (solid line).



(a)



(b)

Figure 32. Frequency dependence of transmission coefficient — amplitude (a) and phase (b) — for the two-ports of Figures 30a (dashed line) and 30b (solid line).

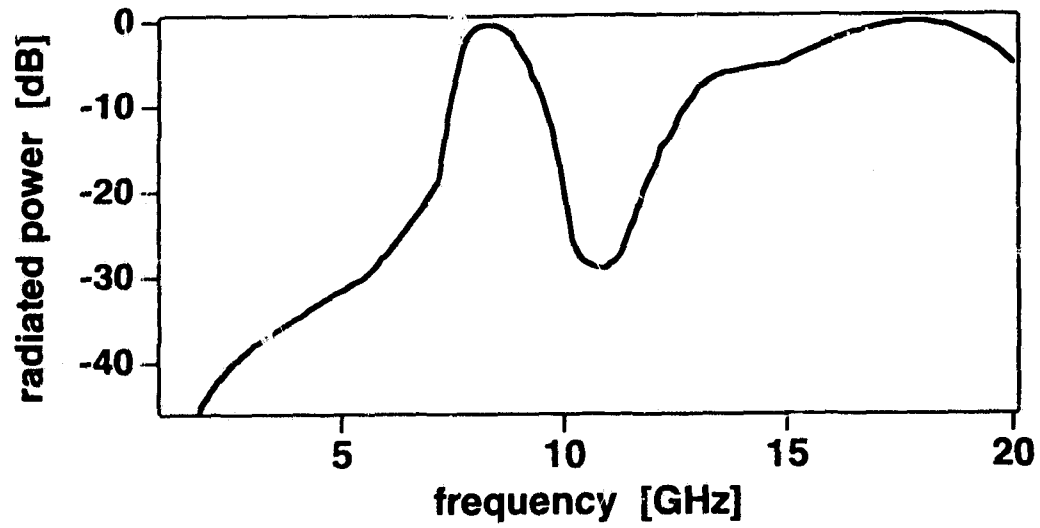


Figure 33. *Frequency dependence of the total power radiated by the two-port of Figure 30b.*

9 RADIATION CHARACTERISTICS OF PLANAR ANTENNAS

This section presents radiation patterns of several planar radiators. Performance of the numerical model that is the subject of this dissertation is shown on three types of feeding mechanisms: coaxial feeding, feeding through coupling to a coplanar transmission line, and feeding through aperture coupling to a microstrip-line. The geometry of the last feeding mechanism listed includes an array of five printed radiators, all of them active, in a multilayer environment, thus demonstrating performance of the model on geometries that are truly complex and, as a rule, difficult to analyze accurately.

All calculations to be presented respect finite conductivities of metals and non-zero conductivities of dielectrics. To prevent computer-memory and -time requirements from becoming exuberant, however, metallic surfaces were modeled as having zero thicknesses.

Because microstrip antennas can be viewed as aperture antennas [130], cross-polarization in this dissertation is understood in terms of Ludwig's third definition [131]. The definition is based on a standard measurement method for testing feeds or small aperture antennas [132], [133], but it is also widely used for large antennas. In the method, co-polarization and cross-polarization are defined to be what one actually measures when antenna radiation patterns are taken in the usual manner [132], [134].

9.1 Coaxial Feeding

The first example is a planar antenna fed by a coaxial probe; the arrangement is depicted in Figure 34. The radiator is fabricated on 3M CuClad 233 microwave substrate.

Figures 35 present calculated radiation patterns in E- and H-planes at the frequency of 6.8 GHz; measured co-polarized E- and H-plane patterns [135] are plotted for comparison. A minute asymmetry can be observed in both the calculated and measured E-plane patterns of the co-polarized component. Inspection of the calculated current distribution on the structure confirms that the asymmetry is a result of the patch's being slightly longer than one half of the guided wavelength at the given frequency. With the exception of angular values below -80 deg and above 80 deg, where pattern measurement

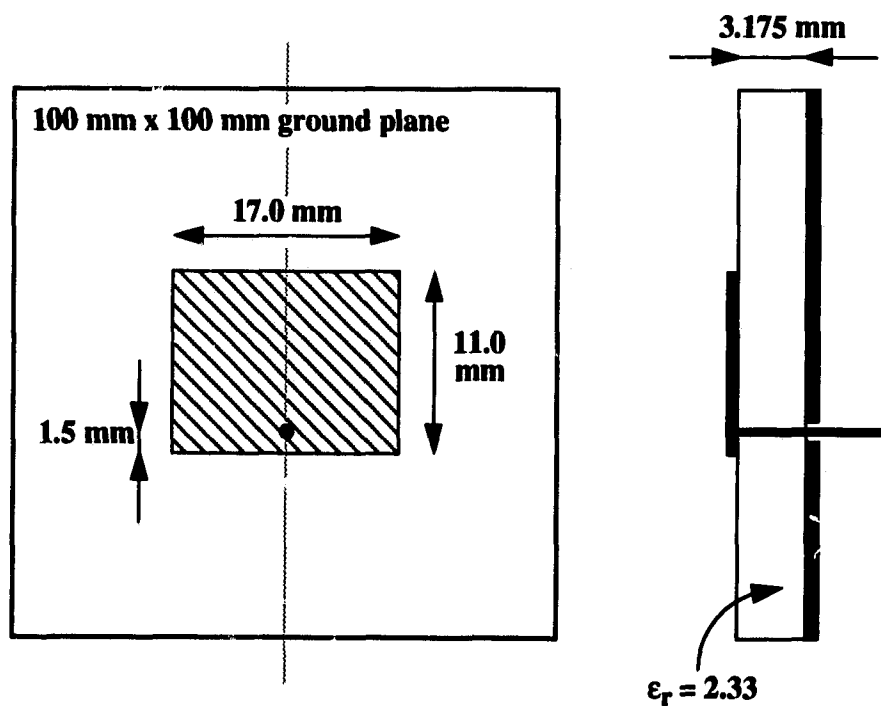
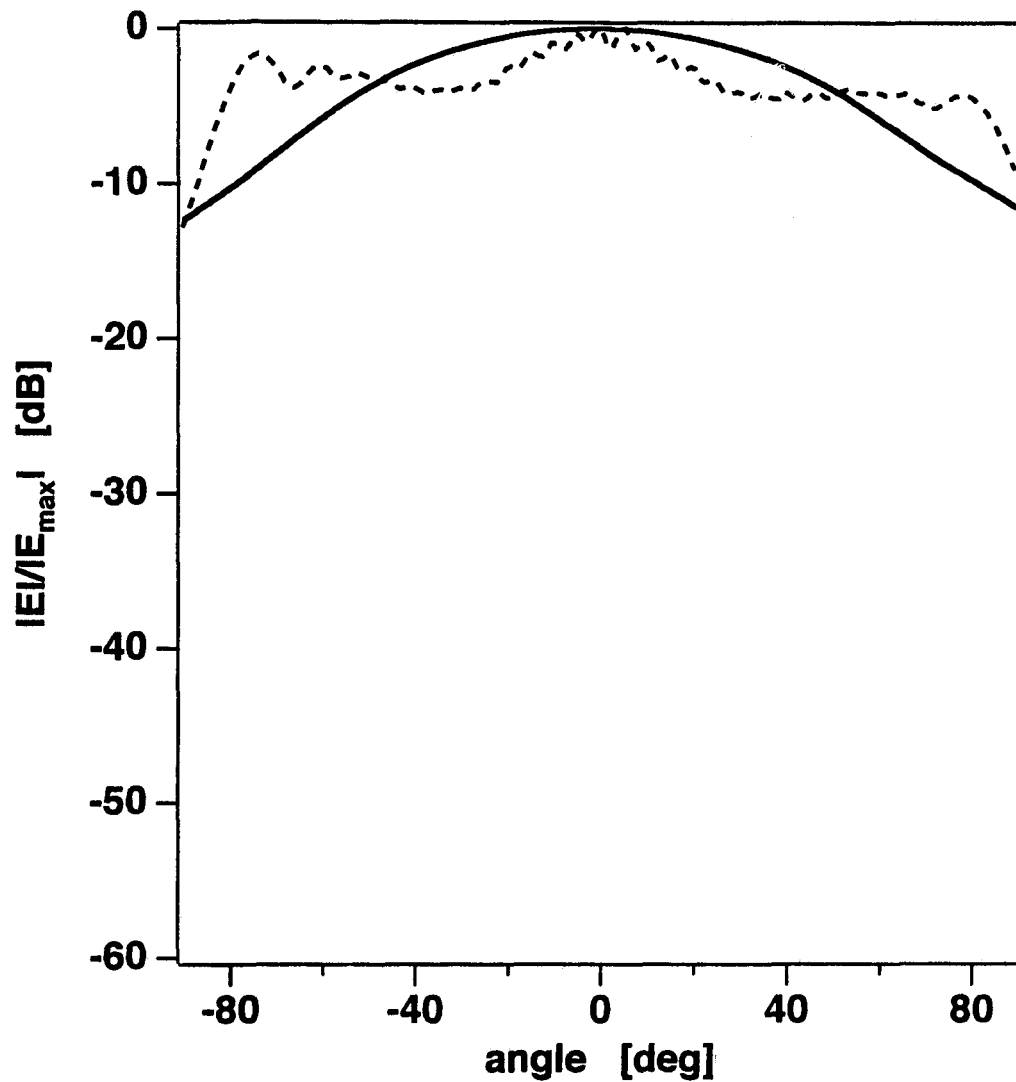
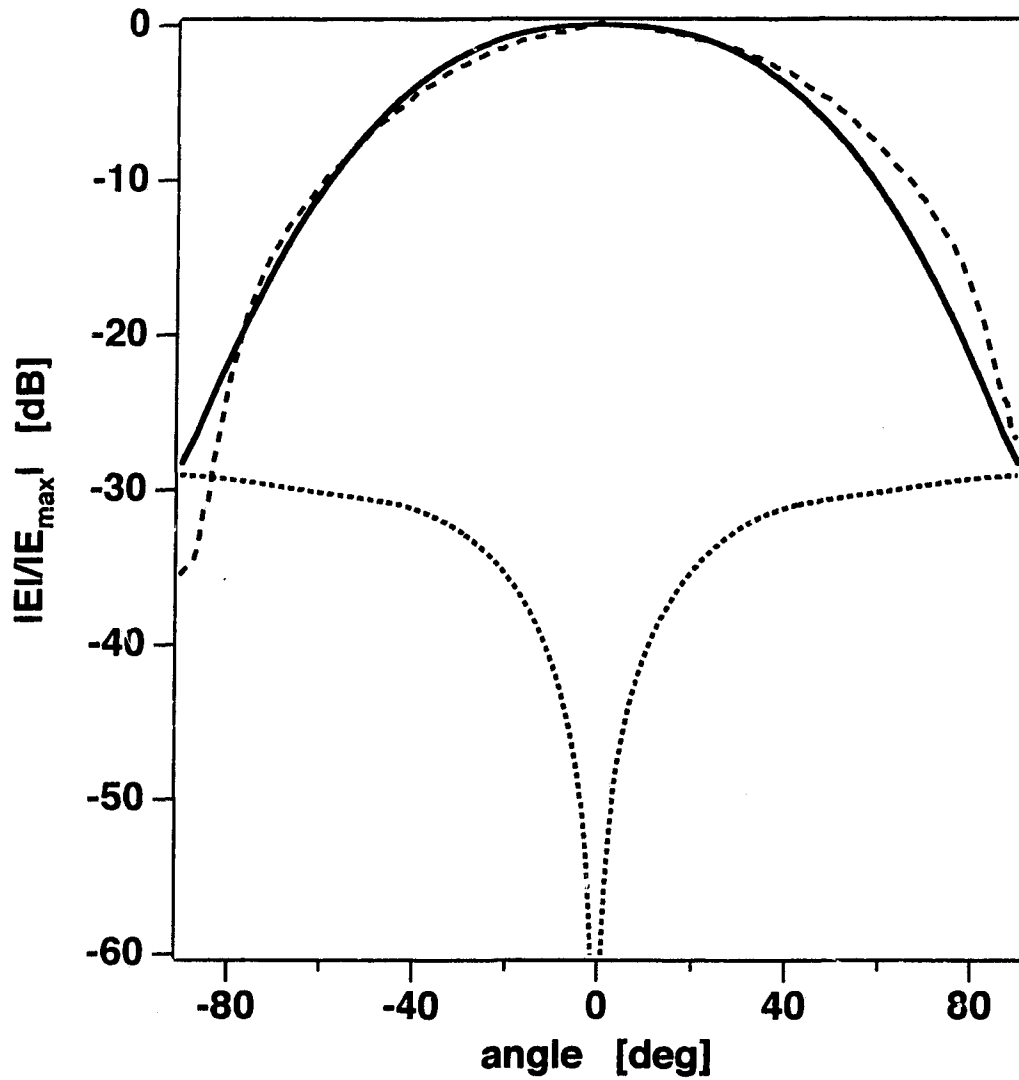


Figure 34. *Coaxially fed rectangular patch antenna.*



(a)

Figure 35. *E*-plane radiation patterns of the coaxially fed rectangular patch antenna of Figure 34 at 6.8 GHz. Solid line: calculated co-polarized; dashed line: measured co-polarized [135]; calculated cross-polarized below -60 dB.



(b)

Figure 35 (cont'd). *H-plane radiation patterns of the coaxially fed rectangular patch antenna of Figure 34 at 6.8 GHz. Solid line: calculated co-polarized; dashed line: measured co-polarized [135]; dotted line: calculated cross-polarized.*

is known to be tricky and burdened by inaccuracies, the calculated and measured patterns are in fairly good agreement, especially in the E-plane. It is not clear whether the deviations in the H-plane are caused by measurement inaccuracies, the inability of our numerical model to represent circular (rather than square) via holes or a combination of both.

Because the patch is fed symmetrically, the cross-polarized component of its E-plane radiation pattern should theoretically be zero. In this and the remaining examples, the calculated value is always below -60 dB. With only limited computer resources on hand, we have assessed that the insignificant difference does not warrant investigations as to whether it is due to computer-roundoff or discretization errors. In addition, the calculated cross-polarized pattern is essentially uniform, which only further supports the roundoff-error explanation.

For the same reason as in the E-plane, the H-plane cross-polarized component should theoretically be zero at patch's zenith, i.e., at the angular value 0 deg; in comparison, the calculated value, once again, is below -60 dB. As the test point moves away from zenith — i.e., the angular variable diverges from zero — the H-plane cross-polarized component, expectedly, increases symmetrically and reaches its maximum at ± 90 deg, which corresponds to testing the radiated field in the plane of the patch. The value of the radiated field at that point depends on the electrical length of the patch along the feeding edge, that is, it depends on whether the radiated fields from both ends of the edge add up in, or out of, phase.

9.2 Coupling to a Coplanar Transmission Line

This type of antenna-feeding mechanism was first successfully proposed by Menzel and Grabherr in [136]. It is depicted in Figure 36. The coupling from the coplanar line to the

patch is accomplished via a slot in the ground plane; the coplanar line is then connected to the slot either capacitively (as in Figure 36) or inductively (in that case, the inner conductor of the coplanar line would be connected directly across the slot). The arrangement combines the advantages of coplanar lines and microstrip patch antennas.

E- and H-plane radiation patterns are shown in Figures 37. The substrate of three times the extent of the patch was modeled. In order to be able to model even the finest features on the back side, non-equidistant segmentation was applied to the structure. Agreement between measurement [136] and computation is good. Some radiation — both co- and cross-polarized — is found on the back side of the patch (which corresponds to the

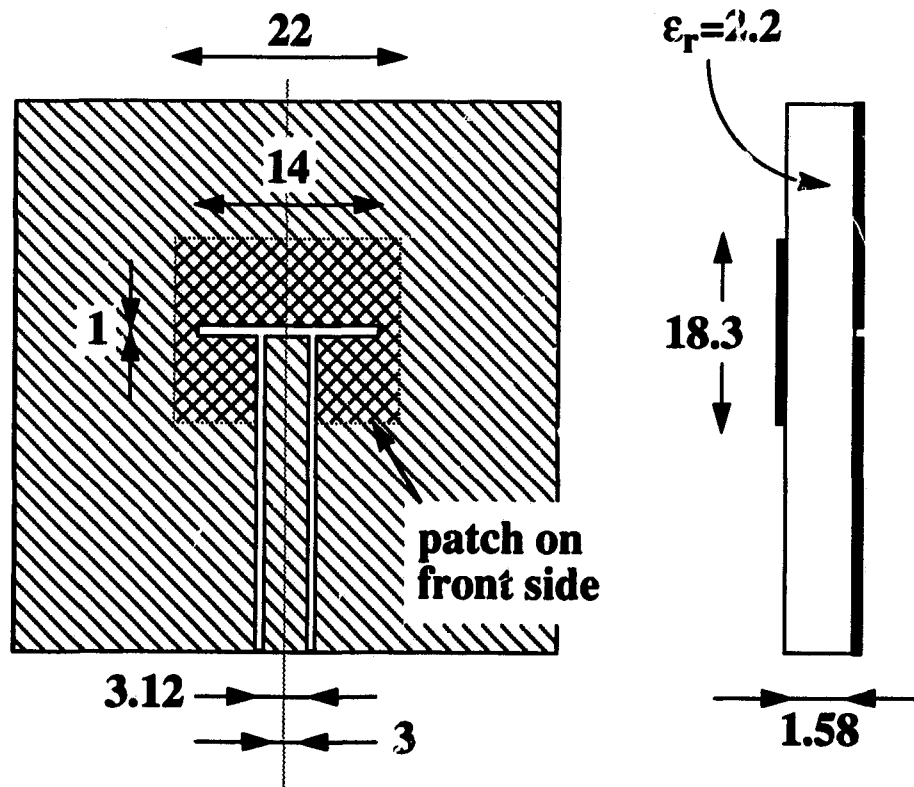
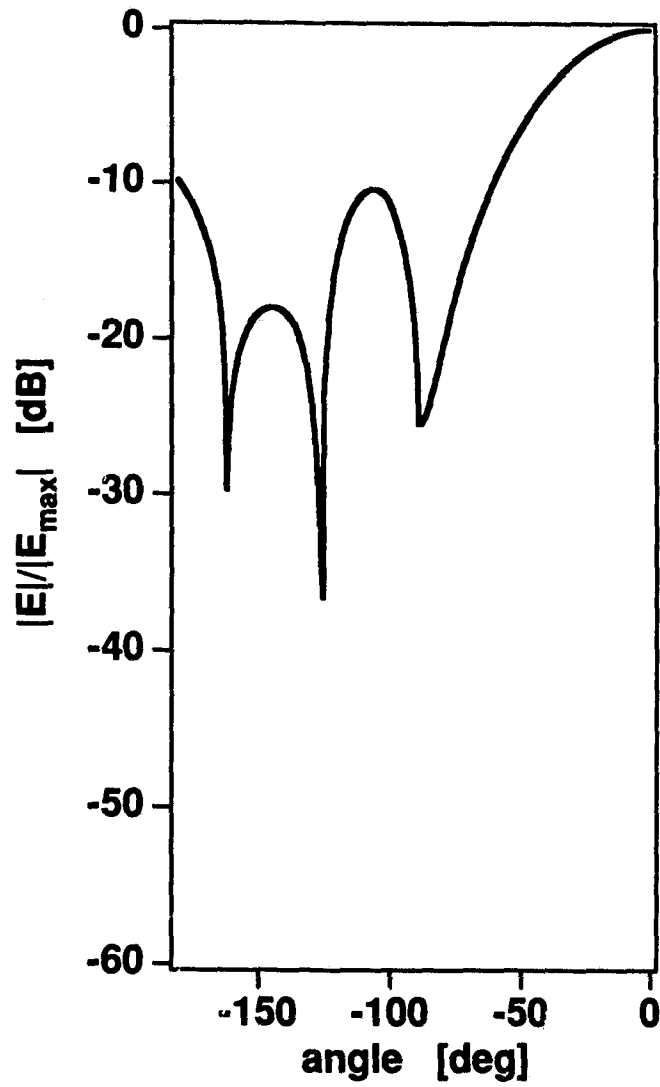
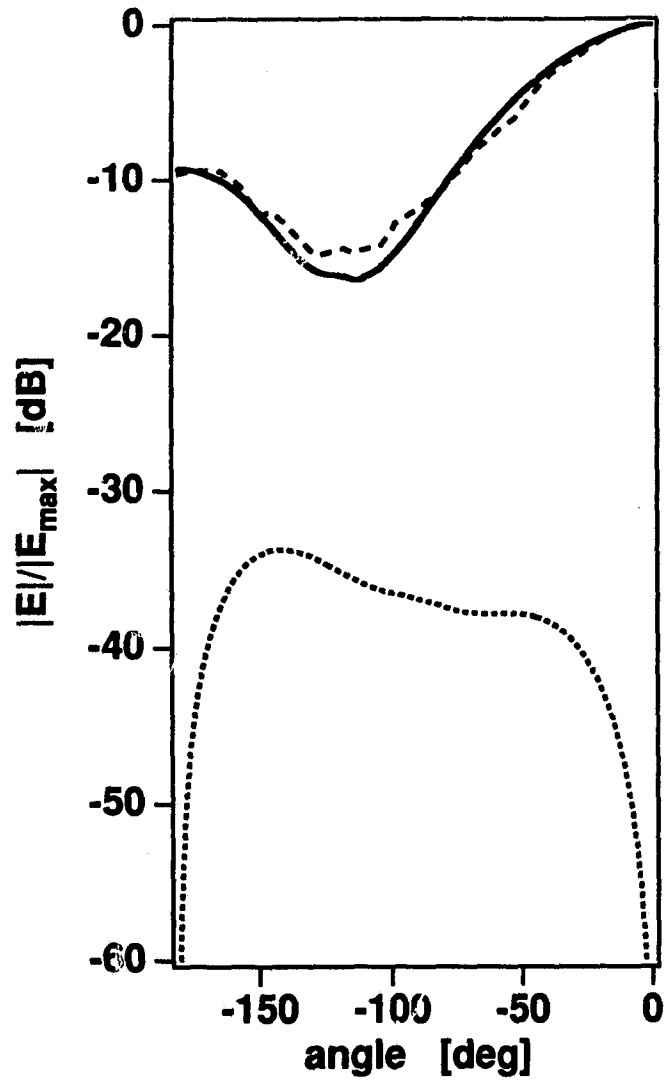


Figure 36. Back-side view of rectangular patch antenna fed by coupling from a coplanar transmission line. Dimensions in millimeters.



(a)

Figure 37. *E-plane radiation patterns of the microstrip patch antenna with coplanar feed line of Figure 36 at 4.3 GHz. Solid line: calculated co-polarized; calculated cross-polarized below -60 dB.*



(b)

Figure 37 (cont'd). *H-plane radiation patterns of the microstrip patch antenna with coplanar feed line of Figure 36 at 4.3 GHz. Solid line: calculated co-polarized; dashed line: measured co-polarized [136]; dotted line: calculated cross-polarized.*

angular variable in the range from -180 to -90 deg in Figures 37). It appears that the amount of energy radiated in the backward direction depends on the length of the coupling slot, that is, how close the coupling slot is to resonance. Changing the length of the slot, however, significantly affects the distribution of currents on the patch, which — in turn — directly modifies radiation properties in the forward direction.

9.3 Aperture Coupling to a Microstrip-Line

In 1985, Pozar in [5] proposed a multilayer patch-antenna feeding mechanism that combines a microstrip transmission line and a rectangular patch, coupling being provided through an opening in the ground plane of the microstrip. As a result, the configuration separates the feeding network from the radiators, thus removing generally undesirable interactions between the radiators on one hand and the feeding microstrips on the other hand. At the same time, it also allows greater flexibility in designing patch antenna arrays, because antenna designers no longer have to zig-zag between — or otherwise bypass and circumvent — individual radiators when drawing the feeding microstrips, all the while attempting to preserve desired phase differences between individual antenna feeding points. The price of the striking elegance, and general ease, of design is increased difficulty of fabrication (associated with the introduction of one extra layer of dielectric and one extra layer of metallization), which ultimately results in a higher cost. Despite the disadvantages, since its introduction, the feeding configuration became recognized as superior to the corporate (microstrip-based) feeding networks and is a preferred choice whenever justified.

Figure 38 depicts the geometry of a microstrip antenna composed of parallel dipole resonators of different lengths, fed by a rectangular slot cut in the ground plane of a microstrip line. The configuration of the resonators is detailed in Figure 39.

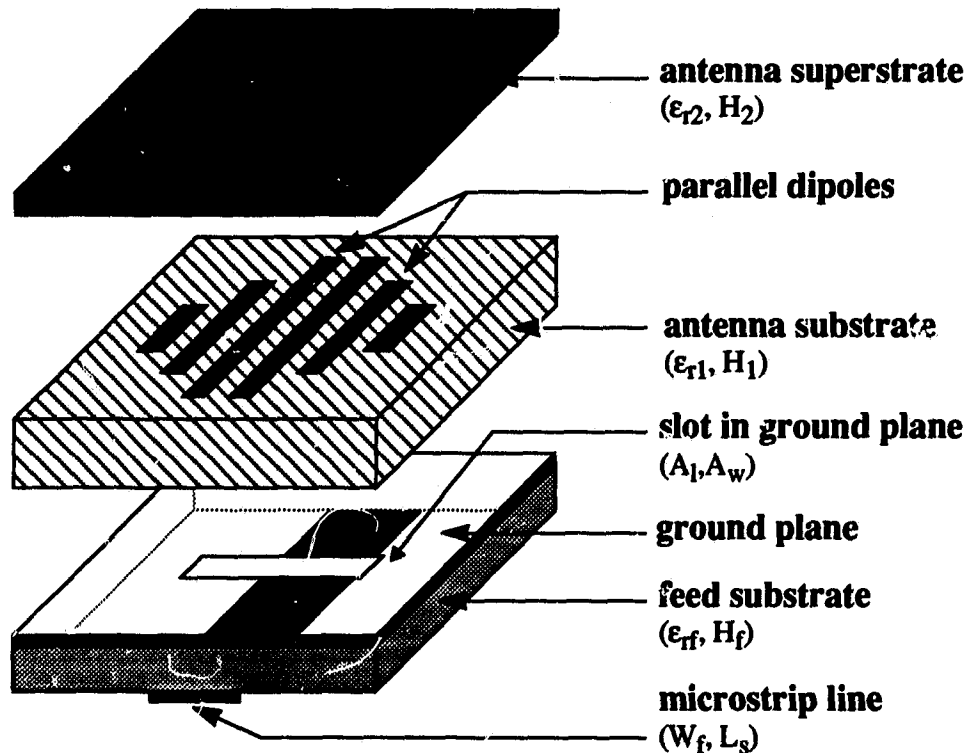


Figure 38. Expanded view of multilayer microstrip antenna comprised of parallel dipoles aperture-coupled to a microstrip line. Dimensions: $\epsilon_{r2} = 2.33$, $H_2 = 0.762$, $\tan \delta_2 = 0.0012$, $\epsilon_{r1} = 1.07$, $H_1 = 5.2$ mm, $\tan \delta_1 = 0.0004$, $A_1 = 13.0$ mm, $A_w = 0.8$ mm, $\epsilon_{rf} = 2.2$, $H_f = 0.762$ mm, $\tan \delta_f = 0.0009$, $W_f = 2.32$ mm, $L_s = 3.0$ mm.

To be able to perform any meaningful calculations at all on available computers, we have modeled the radiating system as a three-layer assemblage only, assuming all metallic surfaces of zero thickness. Refraction occurring at the boundary of dielectrics was properly accounted for, by means of Snell's Law. However, if the ray path (the electrical line of sight) for any two interacting currents was intercepting a metallic surface, mutual impedances for the two currents were set to zero — that is, we assumed that

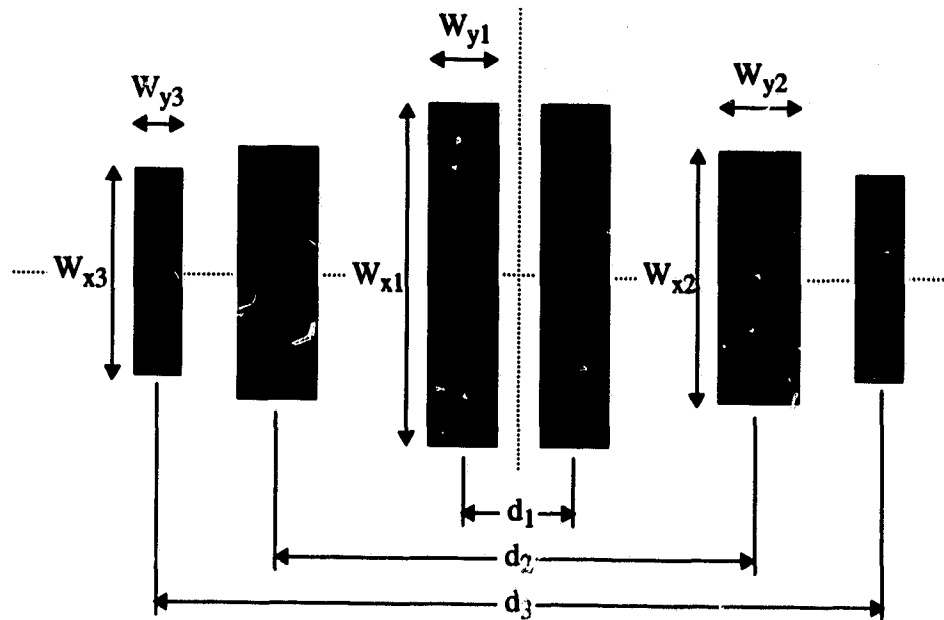
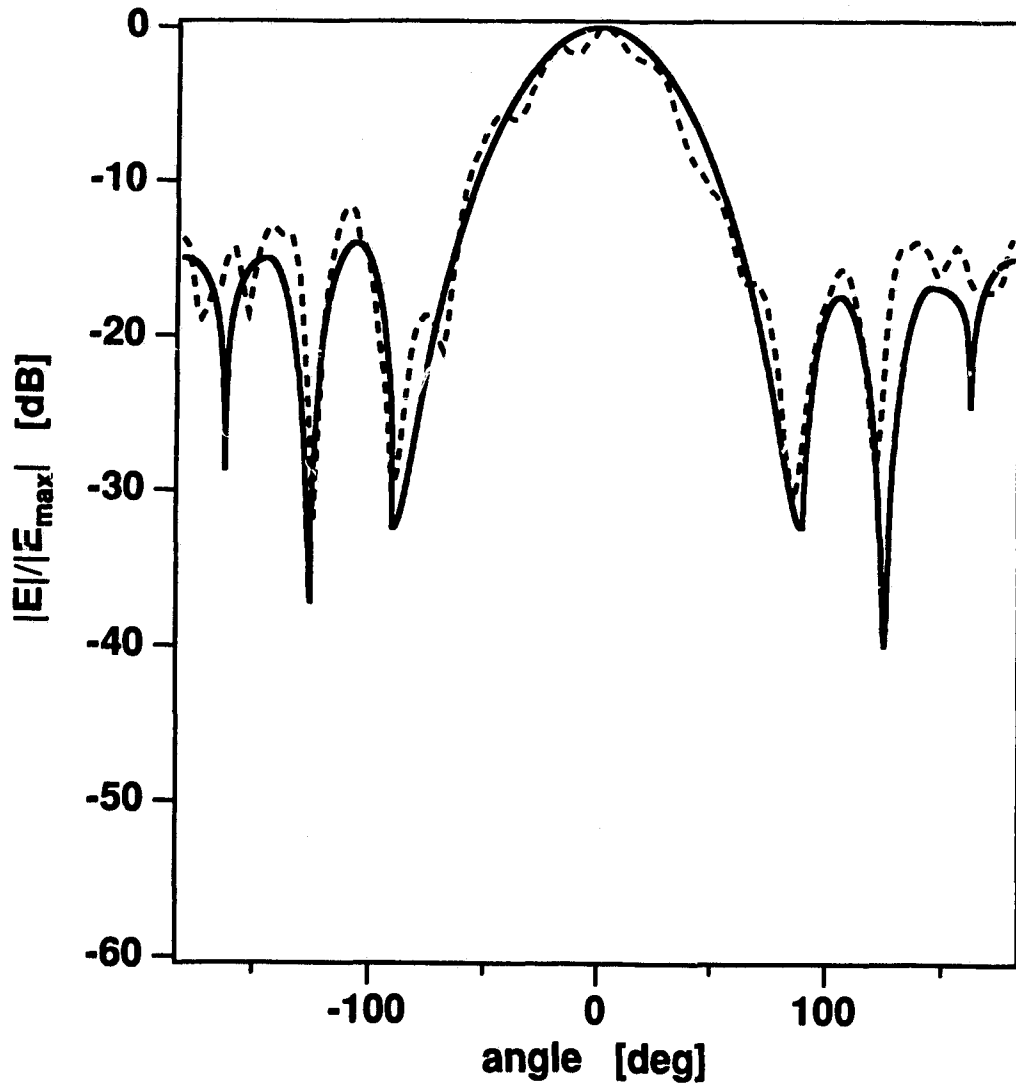


Figure 39. Detailed view of parallel resonators of Figure 38. Dimensions: $W_{x1} = 20.50$ mm, $W_{y1} = 0.25$ mm, $d_1 = 0.25$ mm, $W_{x2} = 17.80$ mm, $W_{y2} = 0.50$ mm, $d_2 = 2.00$ mm, $W_{x3} = 15.50$ mm, $W_{y3} = 0.50$ mm, $d_3 = 4.00$ mm.

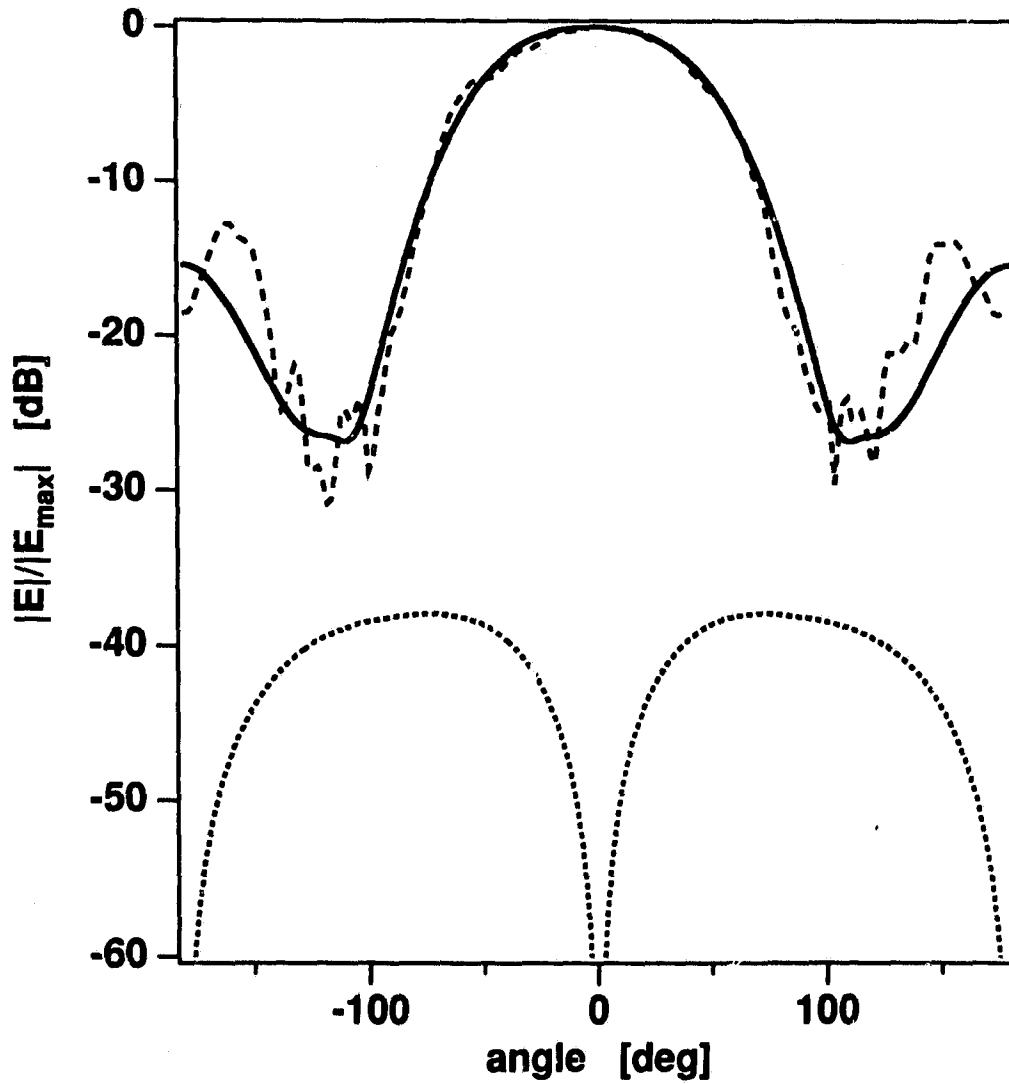
that the metallic surfaces provide perfect shielding; have infinitely high conductivity. The two compromises were the most reasonable arrangement that we were able to come up with under the limitations of finite virtual memory and computer power. In addition, like in the structure of Section 9.2, non-equidistant segmentation was employed.

E- and H-plane radiation patterns of the entire structure at 5.24 GHz are presented in Figures 40. The frequency is the one that corresponds to the resonance of the longest pair of dipoles (c.f. Figure 39). Experimental data [137] are shown to be in good agreement with computed results, especially in the forward direction (which corresponds to the angular variable in the range from -90 to $+90$ deg) with respect to the radiators. We



(a)

Figure 40. *E*-plane radiation patterns of the microstrip antenna of Figure 38 at 5.24 GHz. Solid line: calculated co-polarized; dashed line: measured co-polarized [137]; calculated cross-polarized below -60 dB.



(b)

Figure 40 (cont'd). *H-plane radiation patterns of the microstrip antenna of Figure 38 at 5.24 GHz. Solid line: calculated co-polarized; dashed line: measured co-polarized [137]; dotted line: calculated cross-polarized.*

attribute the backward-radiation deviations to the aforementioned compromises that we had to make in the modeling process.

A performance comparison with the antenna of Section 9.2 is offering itself. From Figures 37 and 40, the two antenna systems perform — in terms of E- and H-plane radiation patterns — similarly in the forward-looking direction. The only noticeable difference is that the antenna of this section has a slightly narrower beam in the E-plane, most likely resulting from focusing properties of the dielectric superstrate. In the backward direction, the coplanar-fed antenna of Section 9.2 radiates more than the microstrip-fed antenna presented in this section. From the radiation-pattern point of view, this appears to be the only shortcoming of the coplanar-fed antenna, which is a price that many an antenna designer would be glad to pay for the antenna's reduced complexity of construction and lower cost in comparison with the multilayer antenna described in this section.

10 CONCLUSIONS

This dissertation presented a full-wave analysis tool for planar radiators and transmission lines. The current distribution on all components is found by applying a method-of-moments procedure. The utilized method, which is based on the algorithm originally introduced in [62], is capable of accounting for real-material parameters — finite conductivity of metals and non-zero conductivity of dielectrics — as well as metallic surfaces of non-zero thickness and substrates of finite extent.

The introduced technique for the exact numerical evaluation of the two-dimensional generalized exponential integral (Section 3), which replaces the somewhat arbitrary integration procedure of [62], makes the method *systematic* and suitable for the analysis of even highly complex structures in an unambiguous way. Furthermore, it was demonstrated that the method has characteristics of a *field solver*. In this, we feel, primarily consists the new contribution of the dissertation.

It is crucial for any grid-based solution of Maxwell's curl equations to implicitly enforce the Gauss Law relations for the electric and magnetic fields, which require the absence of free electric and magnetic charges in the source-free space being modeled. As the example shown in Section 4 demonstrated, the utilized grid and algorithm do inherently possess the divergence-free nature prescribed by the Gauss Law.

Performance of the method was tested on comparisons with measured data, in terms of input impedance and input reflection coefficient, of a number of planar radiators and transmission lines (Sections 5—7). On all accounts, good agreement was found. We consider input-impedance/input-reflection-coefficient tests to be the most sensitive

detector of a possible modeling inadequacy and the best indicator of modeling accuracy, because they test performance of the *entire system locally* — at the antenna's feeding point — rather the globally, which is the case of radiation patterns.

Effects of finite-extent substrate were studied on a planar two-port (Section 8). It was shown that they should not be neglected.

Three types of microstrip-antenna feeding mechanisms were modeled, and radiation patterns of the corresponding antenna systems were presented (Section 9). Again, good agreement with measurement — including radiation in the backward direction — resulted.

Although the presented algorithm can conveniently handle the structural complexities associated with planar antennas and transmission lines, it would not be honest from us to pretend that the technique is the method of choice for all microwave systems with planar morphologies. In an inevitable comparison with the finite-difference time-domain method (FDTD) [138], [139], which assigns six unknowns (three E- and three H-field components) — plus material parameters — to each unit cell, our technique works in average with no fewer than nine unknowns (amplitudes of associated surface currents) — plus surface impedances — per unit cell of a large and/or complex structure. However, in a number of configurations, this disadvantage is more than compensated for by the fact that, unlike in FDTD, in our method one does not need to model the surrounding medium, because its effects have been removed through the volume equivalence theorem (Section 3.3).

Accurate method-of-moments modeling of complex planar systems, with all their fine features, typically requires a large mesh and a truly exorbitant volume of computer memory, not uncommonly going beyond all reasonable limits. To make a bad situation worse, the excessive memory requirements are directly linked with similarly excessive amounts of computational time. It is not possible to bypass the issues of required

memory; in general, one can only partially remove them, by reducing the order of the impedance matrix — sacrificing the accuracy of solution in the process. Nevertheless, the problem of processing time can be alleviated by employing massively-parallel processing (MPP). While the process of setting up the impedance matrix in a method-of-moments formulation is highly suitable for parallelization (individual mutual and self-impedances can almost always be calculated independently of one another), matrix-inversion algorithms — including the ones developed specifically for MPP — are known for their very low computational efficiency. With current costs of MPP machines' processor time being still very high, MPP clearly is not the best choice.

At present, distributed processing, which combines simplicity and advantages of single-processor machines with raw, strength-in-numbers computer-power of MPP, offers — what appears to be — the most feasible solution. It enables the characteristics of large problems of practical interest to be computed in acceptable amounts of time. In fact, the antenna systems of Sections 9.3 and 9.4 were analyzed on one such computer: a four-processor, hyperSPARC-based Sun machine, supported by a full complement of RAM. In comparison with MPP, distributed processing improves computational efficiency significantly (thus increases the science-per-dollar ratio), while maintaining the accuracy and versatility of the method.

A class of its own are issues associated with metallic surfaces in multilayer antennas. Accurate and efficient accounting for all physical phenomena that typically occur there (non-zero penetration depths, diffraction on the edges of apertures, etc.) opens up a Pandora's box of problems, and we can easily envision an entire academic career being devoted to — and built on — solving them. This is one of the suggestions that we are presenting for future research.

Another logical step would encompass the incorporation of unit cells other than blocks, resulting in a better representation of round contours (which in the existing

model can only be modeled as series of step functions), circular via holes and other components.

More refinement would consist in replacing the triangles in rooftop functions, which yield piece-wise linear distributions of current, with piece-wise sinusoidal functions, thus making the resulting current distributions approximate the physical reality better. Because of new modulating functions in the generalized exponential integrals of Section 3.6, this task would necessitate the derivation and development of new integration subroutines, which would have to perform with the efficiency and effectiveness of the ones presented in this dissertation, in order not to be of only academic importance. It may also be useful to follow the line of thought even further, by employing such basis functions that would result in yet more precise approximation of physics.

Finally, we conclude with the suggestion of extending the model to all structures, not only planar ones. This we would consider to be the ultimate goal.

BIBLIOGRAPHY

- [1] *Preparing for the Future/ESA's Technology Programme Quarterly*, Vol. 4, No. 1, March 1994, ESA Publications Division.
- [2] S.W. Greenwood, "The application of imaging sensors to aircraft landing in adverse weather," *Microwave Journal*, pp. 80—89, Sep. 1992.
- [3] H. Bierman, "Personal communications, and motor vehicle and highway automation spark new microwave applications," *Microwave Journal*, pp. 26—40, Aug. 1991.
- [4] H.I. Elowitz, "The Global Positioning System," *Microwave Journal*, pp. 24—33, Apr. 1992.
- [5] D.M. Pozar, "A microstrip antenna aperture-coupled to a microstrip line," *Electronics Letters*, vol. 21, pp. 49—50, Jan. 17, 1985.
- [6] K.R. Carver, J.W. Mink, "Microstrip antenna technology," in *Microstrip Antenna Design* (edited by K.C. Gupta and A. Benalla). Norwood, MA: Artech House, 1988, pp. 13—35.
- [7] X.Z. Gao, K. Chang, "Analysis of microstripline coupled to microstrip antenna," *Electronics Letters*, vol. 23, pp. 694—695, Jun. 18, 1987.
- [8] P.L. Sullivan, D.H. Schaubert, "Analysis of an aperture coupled microstrip antenna," *IEEE Trans. Antennas Propagation*, vol. AP-34, pp. 977—984, Aug. 1986.

- [9] N. Herscovici, D.M. Pozar, "Full-wave analysis of aperture-coupled microstrip lines," *IEEE Trans. Microwave Theory Tech.*, vol. MTT-39, pp. 1108—1114, Jul. 1991.
- [10] S.G. Pan, I. Wolff, "Computation of mutual coupling between slot-coupled microstrip patches in a finite array," *IEEE Trans. Antennas Propagation*, vol. AP-40, pp. 1047—1053, Sep. 1992.
- [11] G.A. Deschamps, "Microstrip microwave antennas," presented at the 3rd USAF Symposium on Antennas, 1953.
- [12] H. Gutton, G. Baissinot, "Flat aerial for ultra high frequencies," French Patent No. 703113, 1955.
- [13] L. Lewin, "Radiation from discontinuities in stripline," in *Proc. Inst. Elec. Eng.*, vol. 107, pt. C, pp. 163—170, Feb. 1960.
- [14] E.V. Byron, "A new flush-mounted antenna element for phased array application," in *Proc. Phased-Array Antenna Symp.*, 1970, pp. 187—192.
- [15] R.E. Munson, "Single slot cavity antennas assembly," U.S. Patent No. 3713162, Jan. 23, 1973.
- [16] J.Q. Howell, "Microstrip antennas," in *Dig. Int. Symp. Antennas Propagation Soc.*, Williamsburg, VA, pp. 177—180, Dec. 1972.
- [17] H.D. Weinschel, "Progress report on development of microstrip cylindrical arrays for sounding rockets," New Mexico State Univ., Las Cruces, NM, 1973.
- [18] G.G. Sanford, "Conformal microstrip phased array for aircraft tests with ATS-6," in *Proc. Nat. Electronics Conf.*, vol. 29, pp. 252—257, Oct. 1974.
- [19] G.W. Garvin, R.E. Munson, L.T. Ostwald, K.G. Schroeder, "Low profile electrically small missile base mounted microstrip antennas," in *Dig. Int. Symp. Antennas Propagation Soc.*, Urbana, IL, pp. 244—247, Jun. 1975.
- [20] J.Q. Howell, "Microstrip antennas," *IEEE Trans. Antennas Propagation*, vol. AP-23, no. 1, pp. 90—93, Jan. 1975.

- [21] H.D. Weinschel, "A cylindrical array of circularly polarized microstrip antennas," in *Dig. Int. Symp. Antennas Propagation Soc.*, Urbana, IL, pp. 177—180, Jun. 1975.
- [22] J.R. James, G.J. Wilson, "New design techniques for microstrip antenna arrays," in *Proc. 5th European Micro. Conf.*, Hamburg, pp. 102—106, Sep. 1975.
- [23] R.E. Munson, "Conformal microstrip antennas and microstrip phased arrays," *IEEE Trans. Antennas Propagation*, vol. AP-22, no. 1, pp. 74—78, Jan. 1974.
- [24] A.G. Derneryd, "Linearly polarized microstrip antennas," *IEEE Trans. Antennas Propagation*, vol. AP-24, pp. 846—851, Nov. 1976.
- [25] A.K. Bhattacharyya, R. Garg, "A generalized transmission line model for microstrip patches," *Proc. Inst. Elec. Eng.*, vol. 132, pt. H, no. 132, pp. 93—98, Apr. 1985.
- [26] G. Dubost, "Transmission line model analysis of lossy rectangular microstrip patch," *Electronics Letters*, vol. 18, no. 7, pp. 281—282, Apr. 1982.
- [27] G. Dubost, "Linear transmission line model analysis of arbitrary-shape patch antenna," *Electronics Letters*, vol. 22, no. 15, pp. 798—799, Jul. 1986.
- [28] G. Dubost, G. Beauquet, "Linear transmission line model analysis of a circular patch antenna," *Electronics Letters*, vol. 22, no. 22, pp. 1174—1176, Oct. 1986.
- [29] R.W. Dearnley, A.R.F. Barel, "A broad-band transmission line model for a rectangular microstrip antenna," *IEEE Trans. Antennas Propagation*, vol. AP-37, no. 1, pp. 6—15, Jan. 1989.
- [30] A.K. Bhattacharyya, "Long rectangular patch antenna with a single feed," *IEEE Trans. Antennas Propagation*, vol. AP-38, no. 7, pp. 987—993, Jul. 1990.
- [31] Y.T. Lo, D. Solomon, W.F. Richards, "Theory and experiment on microstrip antennas," in *Proc. 1978 Antenna Applications Symp.* (sponsored by Electromagnetics Lab., Univ. of Illinois, Urbana).

- [32] W.F. Richards, Y.T. Lo, D.D. Harrison, "An improved theory for microstrip antennas and applications," *IEEE Trans. Antennas Propagation*, vol. AP-29, no. 1, pp. 38—46, Jan. 1981.
- [33] K.C. Gupta, P.C. Sharma, "Segmentation and desegmentation techniques for the analysis of planar microstrip antennas," in *Proc. IEEE Int. Symp. Antennas Propagation*, 1981, pp. 19—22
- [34] P. C. Sharma, K.C. Gupta, "Analysis and optimized design of single feed circularly polarized microstrip antennas," *IEEE Trans. Antennas Propagation*, vol. AP-31, no. 11, pp. 949—955, Nov. 1983.
- [35] V. Palanisamy, R. Garg, "Analysis of arbitrarily shaped microstrip patch antennas using segmentation technique and cavity model," *IEEE Trans. Antennas Propagation*, vol. AP-34, no. 10, pp. 1208—1213, Oct. 1986.
- [36] K.C. Gupta, "Multiport network modeling approach for computer-aided design of microstrip patches and arrays," in *Proc. IEEE Int. Symp. Antennas Propagation*, 1987.
- [37] D.C. Chang, "Analytical theory of an unloaded rectangular microstrip patch," *IEEE Trans. Antennas Propagation*, vol. AP-29, pp. 54—62, 1981.
- [38] A.T. Fialkovskiy, B.A. Krivozubov, "Theory of edge effects in printed circuits and its applications" (in Russian), *Radiotekh. Elektron.*, vol. 23, pp. 502—508, 1978.
- [39] I. Wolff, N. Knoppik, "Rectangular and circular microstrip disk capacitors and resonators," *IEEE Trans. Microwave Theory Tech.*, vol. MTT-22, pp. 857—864, 1974.
- [40] B. Easter, R.J. Roberts, "Radiation from half-wavelength open circuit microstrip resonators," *Electronics Letters*, vol. 6, pp. 573—574, 1970.
- [41] J.R. James, A. Henderson, "High-frequency behavior of microstrip open-circuit terminations," *IEE Proc. Microwaves, Optics and Acoustics*, vol. 3, pp.205—218, 1979.

- [42] I.J. Bahl, P. Bhartia, *Microstrip Antennas*. Dedham, MA: Artech House, 1990, ch. 2.
- [43] B. Noble, *Methods Based on the Wiener-Hopf Technique*. London: Pergamon Press, 1958.
- [44] T. Itoh, R. Mittra, "Analysis of a microstrip disk resonator," *Arch. Elek. Ubertragung.*, vol. 27, pp. 456—458, Nov. 1973.
- [45] T. Itoh, "Analysis of microstrip resonators," *IEEE Trans. Microwave Theory Tech.*, vol. MTT-22, pp. 946—952, Nov. 1974.
- [46] T. Itoh, W. Menzel, "A full-wave analysis method for open microstrip structures," *IEEE Trans. Antennas Propagation*, vol. AP-29, no. 1, pp. 63—67, Jan. 1981.
- [47] J.N. Brittingham, E.K. Miller, J.T. Okada, "A bivariate interpolation approach of efficiently and accurately modeling of antennas near a half space," *Electronics Letters*, vol. 13, pp. 690—691, 1977.
- [48] Y. Rahmat-Samii, P. Parhami, R. Mittra, "Transient response of loaded horizontal antenna over an imperfect ground," *IEEE Trans. Antennas Propagation*, vol. AP-26, pp. 789—796, 1978.
- [49] P. Parhami, Y. Rahmat-Samii, R. Mittra, "An efficient approach for evaluating Sommerfeld integrals encountered in the problem of a current element radiating over a lossy ground," *IEEE Trans. Antennas Propagation*, vol. AP-28, pp. 100—104, 1980.
- [50] R.S. Elliott, *Antenna Theory and Design*. Englewood Cliffs, NJ: Prentice-Hall, 1981.
- [51] J.R. Mosig, F.E. Gardiol, "General integral equation formulation for microstrip antennas and scatterers," *Proc. IEE*, pt. H, vol. 132, pp. 424—432, Dec. 1985.
- [52] J.R. Mosig, F.E. Gardiol, "Analytical and numerical techniques in the Green's function treatment of microstrip antennas and scatterers," *Proc. IEE*, pt. H, vol. 130, pp. 175—182, Mar. 1983.

- [53] J.R. Mosig, "Arbitrarily shaped microstrip structures and their analysis with mixed potential integral equation" *IEEE Trans. Microwave Theory Tech.*, vol. MTT-36, no. 2, pp. 314—323, Feb. 1988.
- [54] J.P. Damiano, "Computation of input impedance in microstrip antennas, graphic representation and numerical integration of oscillating functions," *Proc. IEE*, pt. H, vol. 134, pp. 456—466, 1987.
- [55] D.M. Pozar, "Input impedance and mutual coupling of rectangular microstrip antennas," *IEEE Trans. Antennas Propagation*, vol. AP-30, no. 11, pp. 1191—1196, Nov. 1982.
- [56] E.H. Newman, J.H. Richmond, B.W. Kwan, "Mutual impedance computation between microstrip antennas," *IEEE Trans. Microwave Theory Tech.*, vol. MTT-31, no. 11, pp. 941—945, Nov. 1983.
- [57] D.M. Deshpande, M.C. Bailey, "Input impedance of microstrip antennas," *IEEE Trans. Antennas Propagation*, vol. AP-30, no. 7, pp. 645—650, Jul. 1982.
- [58] D.H. Schaubert, D.M. Pozar, A. Adrian, "Effect of microstrip antenna substrate thickness and permittivity: Comparison of theories with experiment," *IEEE Trans. Antennas Propagation*, vol. AP-37, no. 6, pp. 677—682, Jun. 1989.
- [59] D.M. Pozar, S.M. Voda, "A rigorous analysis of a microstripline fed patch antenna," *IEEE Trans. Antennas Propagation*, vol. AP-35, no. 12, pp. 1343—1350, Dec. 1987.
- [60] J. Herault, R. Moint, A. Reineix, B. Jecko, "A new approach to microstrip antennas using a mixed analysis: transient-frequency," *IEEE Trans. Antennas Propagation*, vol. AP-38, no. 8, pp. 1166—1175, Aug. 1990.
- [61] D.R. Jackson, N.G. Alexopoulos, "Simple approximate formulas for input resistance, bandwidth and efficiency of a resonant rectangular patch," *IEEE Trans. Antennas Propagation*, vol. AP-39, no. 3, pp. 407—410, Mar. 1991.

- [62] B.J. Rubin, S. Daijavad, "Radiation and scattering from structures involving finite-size dielectric regions," *IEEE Trans. Antennas Propagation*, vol. AP-38, no. 11, pp. 1863—1873, Nov. 1990.
- [63] R.A. York, R.C. Compton, B.J. Rubin, "Experimental verification of the 2-D rooftop approach for modeling microstrip patch antennas," *IEEE Trans. Antennas Propagation*, vol. AP-39, no. 5, pp. 690—694, May 1991.
- [64] D.M. Pozar, "A reciprocity method of analysis for printed slot and slot-coupled microstrip antennas," *IEEE Trans. Antennas Propagation*, vol. AP-34, pp. 1439—1446, Dec. 1986.
- [65] N.I. Herscovici, D.M. Pozar, "Full-wave solution for an aperture-coupled patch fed by perpendicular coplanar strips," *IEEE Trans. Antennas Propagation*, vol. AP-42, pp. 544—547, Apr. 1994.
- [66] N.I. Herscovici, D.M. Pozar, "Analysis and design of multilayer printed antennas: a modular approach," *IEEE Trans. Antennas Propagation*, vol. AP-41, pp. 1371—1378, Oct. 1993.
- [67] X.H. Yang, L. Shafai, "Characteristics of aperture coupled microstrip antennas with various radiating patches and coupling apertures," *IEEE Trans. Antennas Propagation*, vol. AP-43, pp. 72—78, Jan. 1995.
- [68] N.I. Herscovici, N.K. Das, J. Klugman, "A microstrip array fed by a new type of multilayer feeding network," *Microwave Journal*, pp. 124—134, Jul. 1995.
- [69] S.C. Wu, N.G. Alexopoulos, O. Fordham, "Feeding structure contribution to radiation by patch antennas with rectangular boundaries," *IEEE Trans. Antennas Propagation*, vol. AP-40, pp. 1245—1249, Oct. 1992.
- [70] M.J. Vaughan, K. Y. Hur, R.C. Compton, "Improvement of microstrip patch antenna radiation pattern," *IEEE Trans. Antennas Propagation*, vol. AP-42, pp. 882—885, Jun. 1994.

- [71] A.B. Smolders, "Finite stacked microstrip arrays with thick substrates," Eindhoven University of Technology, EUT Report 93-E-273, 1993.
- [72] L. Barlatey, J.R. Mosig, T. Sphicopoulos, "Analysis of stacked microstrip patches with a mixed potential integral equation," *IEEE Trans. Antennas Propagation*, vol. AP-38, pp. 608—615, 1990.
- [73] T.M. Au, K.M. Luk, "Effect of parasitic element on the characteristics of microstrip antenna," *IEEE Trans. Antennas Propagation*, vol. AP-39, pp. 1247—1251, Aug. 1991.
- [74] D.R. Jackson, N.G. Alexopoulos, "Gain enhancement methods for printed circuit antennas," *IEEE Trans. Antennas Propagation*, vol. AP-33, pp. 976—987, Sep. 1985.
- [75] H.Y. Yang, N.G. Alexopoulos, "Gain enhancement methods for printed circuit antennas through multiple superstrates," *IEEE Trans. Antennas Propagation*, vol. AP-35, pp. 860—863, Jul. 1987.
- [76] D.R. Jackson, A.A. Oliner, "A leaky-wave analysis of the high-gain printed antenna configuration," *IEEE Trans. Antennas Propagation*, vol. AP-36, pp. 905—910, Jul. 1988.
- [77] X.H. Shen, G.A.E. Vandenbosch, A.R. Van de Capelle, "Study of gain enhancement method for microstrip antennas using moment method," *IEEE Trans. Antennas Propagation*, vol. AP-43, pp. 227—231, Mar. 1995.
- [78] C. Wu, K.L. Wu, Z.Q. Bi, J. Litva, "Accurate characterization of planar printed antennas using finite-difference time-domain method," *IEEE Trans. Antennas Propagation*, vol. AP-40, pp. 526—534, May 1992.
- [79] A. Dreher, R. Pregla, "Full-wave analysis of radiating planar resonators with the method of lines," *IEEE Trans. Microwave Theory Tech.*, vol. MTT-41, pp. 1363—1368, Aug. 1993.

- [80] R.E. Collin, *Antennas and Radiowave Propagation*. New York, NY: McGraw-Hill, 1985, ch. 3.
- [81] V. Galindo, C.P. Wu, "Integral equations and variational expressions for arbitrary scanning of regular infinite arrays," *IEEE Trans. Antennas Propagation*, vol. AP-14, pp. 392—394, May 1966.
- [82] V. Galindo, C.P. Wu, "A variational expression for the dominant mode coupling coefficients between the elements in an infinite array," *IEEE Trans. Antennas Propagation*, vol. AP-14, pp. 637—638, Nov. 1966.
- [83] V.W.H. Chang, R.W.P. King, "On two arbitrarily located identical parallel antennas," *IEEE Trans. Antennas Propagation*, vol. AP-16, no. 3, pp. 309—317, May 1968.
- [84] V.D. Agrawal, Y.T. Lo, "Mutual coupling in phased arrays of randomly spaced antennas," *IEEE Trans. Antennas Propagation*, vol. AP-20, no. 3, pp. 288—295, May 1972.
- [85] N. Amitay, V. Galindo, C.P. Wu, *Theory and Analysis of Phased Array Antennas*. New York, NY: Wiley-Interscience, 1972.
- [86] R.F. Harrington, J.R. Mautz, "A generalized network formulation for aperture problems," *IEEE Trans. Antennas Propagation*, vol. AP-24, pp. 870—873, Nov. 1976.
- [87] R.F. Harrington, J.R. Mautz, "Electromagnetic transmission through a rectangular aperture in a perfectly conducting plane," Scientific Report No. 10, Contract F19628-73-C-0047 with Air Force Cambridge Research Laboratories, Hanscom AFB, MA, Feb. 1976.
- [88] R.P. Jedlicka, M.T. Poe, K.R. Carver, "Measured mutual coupling between microstrip antennas," *IEEE Trans. Antennas Propagation*, vol. AP-29, pp. 147—149, 1981.

- [89] D.M. Pozar, "Finite phased arrays of rectangular microstrip patches," *IEEE Trans. Antennas Propagation*, vol. AP-34, no. 5, pp. 658—665, May 1986.
- [90] P.B. Katehi, "A generalized method for the evaluation of mutual coupling in microstrip arrays," *IEEE Trans. Antennas Propagation*, vol. AP-35, no. 2, pp. 125—133, Feb. 1987.
- [91] A.K. Bhattacharyya, L. Shafai, "Surface wave coupling between circular patch antennas," *Electronics Letters*, vol. 22, no. 22, pp. 1198—1200, Oct. 1986.
- [92] N.K. Das, D.M. Pozar, "Multiport scattering analysis of general multilayered printed antennas fed by multiple feed ports: Part I — theory," *IEEE Trans. Antennas Propagation*, vol. AP-40, no. 5, pp. 469—481, May 1992.
- [93] N.K. Das, D.M. Pozar, "Multiport scattering analysis of general multilayered printed antennas fed by multiple feed ports: Part II — applications," *IEEE Trans. Antennas Propagation*, vol. AP-40, no. 5, pp. 482—491, May 1992.
- [94] A.K. Skrivervik, J.R. Mosig, "Finite phased array of microstrip patch antennas: the infinite array approach," *IEEE Trans. Antennas Propagation*, vol. AP-40, pp. 579—582, May 1992.
- [95] A.K. Skrivervik, J.R. Mosig, "Analysis of finite phase arrays of microstrip patches," *IEEE Trans. Antennas Propagation*, vol. AP-41, pp. 1105—1114, Aug. 1993.
- [96] A.A. Ishimaru, R.G. Coe, G.E. Miller, W.P. Geren, "Finite periodic structure approach to large scanning array problems," *IEEE Trans. Antennas Propagation*, vol. AP-33, pp. 1213—1220, 1985.
- [97] P.R. Haddad, D.M. Pozar, "Anomalous mutual coupling between microstrip antennas," *IEEE Trans. Antennas Propagation*, vol. AP-42, pp. 1545—1549, Nov. 1994.
- [98] S.G. Mikhlin, *Variational Methods in Mathematical Physics*. New York, NY: Pergamon Press, 1964.

- [99] B.G. Galerkin, "Rods and plates. Series occurring in various questions concerning the elastic equilibrium of rods and plates" (in Russian), *Engineers' Bulletin*, no. 19, 1915, pp. 897—908.
- [100] I.G. Bubnov, "Report on the works of Prof. Timoshenko which were awarded the Zhuranskiy prize" (in Russian), in *Proc. Symposium of the Institute of Communication Engineers*, no. 81, All-Union Special Planning Office, 1913.
- [101] R.F. Harrington, *Field Computation by Moment Methods*. New York, NY: Macmillan, 1968.
- [102] M.F. Catedra, E. Gago, L. Nuno, "A numerical scheme to obtain the RCS of three-dimensional bodies of resonant size using the conjugate gradient method and the fast Fourier transform," *IEEE Trans. Antennas Propagation*, vol. AP-37, pp. 528—537, May 1989.
- [103] T.K. Sarkar, E. Arvas, S. Ponnappalli, "Electromagnetic scattering from dielectric bodies," *IEEE Trans. Antennas Propagation*, vol. AP-37, pp. 673—676, May 1989.
- [104] A.W. Glisson, "An integral equation for electromagnetic scattering from homogeneous dielectric bodies," *IEEE Trans. Antennas Propagation*, vol. AP-32, pp. 173—175, Feb. 1984.
- [105] R.F. Harrington, J.R. Mautz, "An impedance sheet approximation for thin dielectric shells," *IEEE Trans. Antennas Propagation*, vol. AP-23, pp. 531—534, Jul. 1975.
- [106] C.A. Balanis, *Advanced Engineering Electromagnetics*. New York, NY: John Wiley & Sons, 1989, ch. 7.
- [107] E.C. Jordan, K.G. Balmain, *Electromagnetic Waves and Radiating Systems*. Englewood Cliffs, NJ: Prentice-Hall, 1968, ch. 5.
- [108] S. Ramo, J.R. Whinnery, T. Van Duzer, *Fields and Waves in Communication Electronics*. New York, NY: John Wiley & Sons, 1965, ch. 5.

- [109] S. Amari, J. Bornemann, "Spectral-domain modelling of superconducting microstrip structures," presented at Progress in Electromagnetics Research Symposium, Seattle, Washington, 1995.
- [110] J.H. Richmod, "A wire-grid model for scattering by conducting bodies," *IEEE Trans. Antennas Propagation*, vol. AP-14, pp. 782—786, Nov. 1966.
- [111] M. Gimersky, J. Bornemann, "Utilization of symmetry properties for the pattern analysis of mutually coupled patch radiators," *Radioengineering*, vol. 1, pp. 11—16, May 1992.
- [112] M. Gimersky, J. Bornemann, "A simplified technique for the analysis of single and coupled microstrip radiators," *Proc. Wireless 92*, Calgary, Alberta, Jul. 1992.
- [113] W.H. Press, S.A. Teukolsky, W.T. Vetterling, B.P. Flannery, *Numerical Recipes in FORTRAN/The Art of Scientific Computing*. Cambridge, MA: Cambridge University Press, 1992.
- [114] J.R. Mautz, R.F. Harrington, "An *E*-field solution for a conducting surface small comparable to the wavelength," *IEEE Trans. Antennas Propagation*, vol. AP-32, pp. 330—339, Apr. 1984.
- [115] R.W.P. King, *The Theory of Linear Antennas*. Cambridge, MA: Harvard University Press, 1956.
- [116] D.H. Werner, P.L. Werner, J.H. Huffman, A.J. Ferraro, and J.K. Breakall, "An exact solution of the generalized exponential integral and its application to moment method formulations," *IEEE Trans. Antennas Propagation*, vol. AP-41, pp. 1716—1719, Dec. 1993.
- [117] M. Gimersky, S. Amari, J. Bornemann, "Tuning-free analysis of planar radiators based on an exact numerical evaluation of the two-dimensional generalized exponential integral," in *Proc. 1995 IEEE AP-S Symposium*, pp. 1316—1319, Newport Beach, California, June 1995.

- [118] S. Amari, M. Gimersky, J. Bornemann, "Imaginary part of antenna's admittance from its real part using Bode's integrals," *IEEE Trans. Antennas Propagation*, vol. AP-43, pp. 220—223, Feb. 1995.
- [119] H.W. Wyld, *Mathematical Methods for Physics*. New York, NY: Addison-Wesley, 1976, ch. 12.
- [120] N. Balabanian, T.A. Bickart, *Electrical Network Theory*. New York, NY: Wiley, 1969, ch. 6.
- [121] C. Kittel, *Introduction to Solid State Physics*. New York, NY: Wiley, 1986, ch. 11.
- [122] S. Amari, "Single-particle excitations of the electron gas," Ph.D. dissertation, Washington University, St. Louis, MO, 1994.
- [123] W.L. Stutzman, G.A. Thiele, *Antenna Theory and Design*. New York, NY: Wiley, 1981.
- [124] Z. Cai, J. Bornemann, "Rigorous analysis of radiation properties of lossy patch resonators on complex anisotropic media and lossy ground metallization," *IEEE Trans. Antennas Propagation*, vol. AP-42, pp. 1443—1446, Oct. 1994.
- [125] S. Amari, "Evaluation of Cauchy principal-value integrals using modified Simpson rule," *Appl. Math. Lett.*, vol. 7, no. 3, pp. 19—23, 1994.
- [126] J.M. Ziman, *The Principles of the Theory of Solids*. New York, NY: Cambridge, 1972, ch. 8.
- [127] W. Cheney, D. Kincaid, *Numerical Mathematics and Computing*. Monterrey, CA: Brooks/Cole, 1985.
- [128] P.J. Davis, P. Rabinowitz, *Methods of Numerical Integration*. Orlando, FL: Academic Press, 1984.
- [129] A.S. Schelkunoff, *Electromagnetic Waves*. Princeton, NJ: D. Van Nostrand, 1964, ch. 12.
- [130] R.C. Johnson, H. Jasik (Eds.), *Antenna Engineering Handbook*. New York, NY: McGraw-Hill, 1984, ch. 7.

- [131] A.C. Ludwig, "The definition of cross polarization," *IEEE Trans. Antennas Propagation*, vol. AP-21, pp. 116—119, Jan. 1973.
- [132] S. Silver, *Microwave Antenna Theory and Design*. New York, NY: McGraw-Hill, 1949, pp. 557—564.
- [133] "Test procedures for antennas," IEEE Publ. No. 149, Jan. 1965.
- [134] J.D. Kraus, *Antennas*. New York, NY: McGraw-Hill, 1950, ch.15.
- [135] E. Chang, S.A. Long, W.F. Richards, "An experimental investigation of electrically thick rectangular microstrip antennas," *IEEE Trans. Antennas Propagation*, vol. AP-34, pp. 767—772, Jun. 1986.
- [136] W. Menzel, W. Grabherr, "A microstrip patch antenna with coplanar feed line," *IEEE Microwave and Guided Wave Letters*, vol. 1, pp. 340—342, Nov. 1991.
- [137] F. Croq, D.M. Pozar, "Multifrequency operation of microstrip antennas using aperture coupled parallel resonators," *IEEE Trans. Antennas Propagation*, vol. AP-40, pp. 1367—1374, Nov. 1992.
- [138] K.S. Yee, "Numerical solution of initial boundary value problems involving Maxwell's equations in isotropic media," *IEEE Trans. Antennas Propagation*, vol. AP-14, pp. 302—307, May 1966.
- [139] A. Taflove, *Computational Electrodynamics / The Finite-Difference Time-Domain Method*. Boston, MA: Artech House, 1995.

APPENDIX

The Method of Moments

Let us consider equations of the inhomogeneous type

$$L(f) = g, \quad (\text{A-1})$$

where L is an operator, g is the source or excitation (known function), and f is the field or response (unknown function to be determined). A problem of *analysis* involves a determination of f when L and g are given. A problem of *synthesis* involves a determination of L when f and g are specified. In this appendix only the analysis will be considered.

Let f be expanded in a series of functions f_1, f_2, f_3, \dots in the domain of L , as

$$f = \sum_n \alpha_n f_n, \quad (\text{A-2})$$

where the α_n are constants. The f_n are customarily called *expansion functions* or *basis functions*. For exact solutions, (A-2) is usually an infinite summation, and the f_n form a complete set of basis functions. For approximate solutions, (A-2) is usually a finite summation. Substituting (A-2) in (A-1) and using the linearity of L , we have

$$\sum_n \alpha_n L(f_n) = g. \quad (\text{A-3})$$

It is assumed that a suitable inner product $\langle f, g \rangle$, for example,

$$\langle f, g \rangle = \int_0^1 f(x) g(x) dx, \quad (\text{A-4})$$

has been determined for the problem. Now define a set of *weighting functions*, or *testing functions*, w_1, w_2, w_3, \dots in the range of L and take the inner product of (A-3) with each w_m .

The result is

$$\sum_n \alpha_n \langle w_m, Lf_n \rangle = \langle w_m, g \rangle, \quad (\text{A-5})$$

$m = 1, 2, 3, \dots$ This set of equations can be written in matrix form as

$$[l_{mn}] [\alpha_n] = [g_m], \quad (\text{A-6})$$

where

$$[l_{mn}] = \begin{bmatrix} \langle w_1, Lf_1 \rangle & \langle w_1, Lf_2 \rangle & \dots \\ \langle w_2, Lf_1 \rangle & \langle w_2, Lf_2 \rangle & \dots \\ \dots & \dots & \dots \end{bmatrix}, \quad (\text{A-7})$$

$$[\alpha_n] = \begin{bmatrix} \alpha_1 \\ \alpha_2 \\ \dots \end{bmatrix}, \quad (\text{A-8})$$

$$[g_m] = \begin{bmatrix} \langle w_1, g \rangle \\ \langle w_2, g \rangle \\ \dots \end{bmatrix}, \quad (\text{A-9})$$

If the matrix $[l]$ is nonsingular, its inverse $[l^{-1}]$ exists. The α_n are then given by

$$[\alpha_n] = [l^{-1}] [g_m], \quad (\text{A-10})$$

and the solution for f is given by (A-2). For concise expression of this result, define the matrix of functions

$$[\tilde{f}_n] = [f_1 f_2 \dots], \quad (\text{A-11})$$

and write

$$f = [\tilde{f}_n] [\alpha_n] = [\tilde{f}_n] [l_{mn}^{-1}] [g_m]. \quad (\text{A-12})$$

This solution may be exact or approximate, depending on the choice of the f_n and w_n . The particular choice $w_n = f_n$ is known as *Galerkin's method*.

If the matrix $[l]$ is of infinite order, it can be inverted only in special cases, for example, if it is diagonal. The classical eigenfunction method leads to a diagonal matrix and can be thought of as a special case of the method of moments. If the sets f_n and w_n are finite, the matrix is of finite order and can be inverted by known methods.

VITA

Surname: Gimersky

Given Names: Martin

Place of Birth: Presov, Czechoslovakia

Date of Birth: May 23, 1965

Educational Institutions Attended:

University of Victoria 1991 to 1996

Czech Technical University of Prague 1983 to 1990

Degrees Awarded:

Engineer (Honors) Czech Technical University 1988

Honors and Awards:

Czech Tech Fellowship 1984-88

Czech Tech Presidential Graduation Award 1988

Publications:

M. Gimersky, S. Amari, J. Bornemann, "Tuning-free analysis of planar radiators based on an exact numerical evaluation of the two-dimensional generalized exponential integral," in Proc. 1995 IEEE AP-S Symposium, pp. 1316—1319, Newport Beach, California, June 1995.

S. Amari, M. Gimersky, J. Bornemann, "Imaginary part of antenna's admittance from its real part using Bode's integrals," *IEEE Transactions on Antennas and Propagation*, vol. 43, pp. 220—223, February 1995.

P. Horowitz, M. Gimersky, "Design of an L-band dual feedhorn for the purposes of microwave search for extraterrestrial intelligence," *Radioengineering*, vol.3, no. 2, pp. 1—4, July 1994.

M. Gimersky, J. Bornemann, "Investigation of mutual coupling effects on the radiation pattern of rectangular patch antennas," in Proc. 1992 IEEE AP-S Symposium, pp. 1194—1197, Chicago, Illinois, July 1992.

M. Gimersky, J. Bornemann, "A simplified technique for the analysis of single and coupled microstrip radiators," in Wireless 92 Proceedings, Calgary, Alberta, July 1992.

M. Gimersky, J. Bornemann, "Utilization of symmetry properties for the pattern analysis of mutually coupled patch radiators," *Radioengineering*, vol.1, pp. 11—16, May 1992.

P.F. Driessen, M. Gimersky, T. Rhodes, "Polarization effects for indoor propagation," in Wireless 92 Proceedings, Calgary, Alberta, July 1992.

P.F. Driessen, M. Gimersky, T. Rhodes, "Ray model of indoor propagation," in Wireless Personal Communications Symposium Digests, Blacksburg, Virginia, June 1992 (extended version also published in a book).

M. Gimersky, "Calculation of the Cassegrain antenna radiation patterns using the aperture method" (in Slovak), *Slaboproudý obzor*, pp. 291—295, July 1990.

M. Gimersky, "FORTRAN code for calculation of reflector antenna radiation patterns using the aperture method" (in Slovak), *Sdelovaci technika*, pp. 149—152, April 1990.

PARTIAL COPYRIGHT LICENSE

I hereby grant the right to lend my dissertation to users of the University of Victoria Library, and to make single copies only for such users or in response to a request from the library of any other university, or similar institution, on its behalf or for one of its users. I further agree that permission for extensive copying of this dissertation for scholarly purposes may be granted by me or a member of the University designated by me. It is understood that copying or publication of this dissertation for financial gain shall not be allowed without my written permission.

Title of Dissertation:

Full-Wave Analysis of Imperfect Planar Radiators on Lossy Substrates of Finite Extent

Author:

_____ ✓
Martin Gimersky

March 13, 1996